Electrostatic Micro-Hydraulic Hair Sensors and Actuators

by

Mohammad M. Sadeghi

A dissertation submitted in partial fulfillment
of the requirements for the degree of
Doctor of Philosophy
(Electrical Engineering)
in the University of Michigan
2014

Doctoral Committee:

Professor Khalil Najafi, Chair
Associate Professor Luis P. Bernal
William D. Nothwang, Army Research Laboratory
Assistant Professor Rebecca L. Peterson
Professor Kamal Sarabandi
Emeritus Professor Kensall D. Wise

For my family.

Acknowledgments

I would like to sincerely thank my advisor, Professor Khalil Najafi, for his support and the opportunity he provided for me to conduct independent research. His patience and encouragements inspired me during the course of my graduate studies. His dedication to conduct excellent and exceptionally innovative work has always motivated me. I have learned many lessons from him, both personally and professionally. I would also like to thank my dissertation committee members, Professor Luis Bernal, Dr. William Nothwang, Professor Rebecca L. Peterson, Professor Kamal Sarabandi and Professor Ken Wise for accepting to be on my dissertation committee. Many thanks to Prof. Peterson for her unconditional help and support during the course of my studies. Her advice and feedback have always been helpful. I want to acknowledge Mr. Robert Gorndenker for excellently maintaining our test facility and his always helpful technical advice, Dr. Behrouz Shiari for his modeling and simulation support, Mr. Michael Deininger for his technical advice on design of SLA parts and Mr. Brendan Casey for his valuable help on packaging and wire-bonding. I want to express my gratitude to all the staff at Lurie Nanofabrication Facility, who provide an excellent micro-fabrication research facility. Without their efforts, this and many other research works could not be pursued at UM. I also want to acknowledge all of my mentees who helped me with this project over a short period of time: Michael T. Chaney, Bing Zhang, and Karen Dowling. The supportive work and efforts of all the staff in EECS department, especially Ms. Trasa Burkhardt, Ms. Deb Swartz, and Ms. Beth Stalnaker, are appreciated.

I like to acknowledge students and research fellows in Najafi group for being such great colleagues. Working with these talented people has been a great motivation for me; Hanseup Kim, Jay Mitchel, Sang-Hyun Lee, Sang Won Yoon, Tzeno Chalchev, Jae Yoong Cho, Andrew Gross, Erkan Aktakka, Jeffery Gregory, Sanghyun Lee, Seow Yuen Yee, James McCullagh, Daniel Egert, Kevin Owen, Stacey Tang, Jialiang Yan, Yi Yuan and Christopher Boyd. I also enjoyed always having Iranian colleagues in our group: Reza Azadegan, Iman Shahosseini, Ali Besharatian, Ali Darvishian and Amin Sandoughsaz, and special thanks to Dariush Daneshvar, Amir Borna and Niloufar Ghafouri for their invaluable friendship. I learned perseverance, professionalism, critical thinking and dedication from my kind friend Dariush. Many thanks to Amir for his always encouraging complements, enjoyable fishing trips and his exemplary respect for my ideas and otherness. And Niloufar for her joyful teatime talks and amusing political discussions. I must also thank all my other friends at SSEL who made my time here pleasant and were always willing to help: Razi Haque, Gayatri Perlin, Angelique Johnson and Ning Gulari, and this list is not inclusive. I want to express my appreciation to Ali A., for his help with COMSOL simulations, Dariush, Sina, and Mahya for kindly accepting to proofread my dissertation.

I would also like to thank all my friends in Ann Arbor who made my life far away from home enjoyable. Reza Gh. has been a sincere friend and has always been there for me since the very first days I started my PhD. Mostafa, a considerate friend with endless brilliant ideas, will be my tentative business partner. Ali A. with his utmost sympathy, patiently helped me with complicated physical theories and I kept asking him unanswerable questions about fluid dynamics. I had extremely pleasant and refreshing hangouts with Mina, Sina, Mahya, Abbas and Alireza. Reza A. with his sarcasm practically taught me how to agree to disagree while

maintaining our friendship. I always enjoyed intellectual arguments with Farhad, whenever I was overwhelmed with soulless technical matters. Maryam, Mohammad N., Nasrin, Bahareh, Lauleh, Mohammad E. and Fatemeh, they have virtually become my relatives in Ann Arbor and I much enjoy their company. I hereby acknowledge all other friends: Sara, Meysam, Reza F., Mahmoud, Iman, Amirhossein, Rahman, Parisa, Mehrzad, Vahid, Hedieh, Hossein, Behzad, Mehdi, Marjan and Mojtaba with whom I spent my time, for their precious companionship and support throughout the course of my graduate studies.

I have been blessed with unconditional and endless love of my parents and siblings. They have always been supportive of me. My father, Nasim, has been a great role model for me both in personal and professional life. He always encourages me not only to achieve the best, but also to achieve it in the best way. My mother, Badri, a symbol of love never stopped caring and always sees my successes as hers. My parents have constantly believed in me and given me the confidence. My siblings, Fatemeh, Faezeh, Ali and Hassan, have shown their true love and affection throughout my life. Having this lovely family on my side has been the greatest support of all.

Finally, my love, Narges, I owe her a great debt of gratitude for her wonderful companionship. She patiently tolerated countless nights I left her alone to work on my research in the lab. Narges took on more concern and stress for me for my work, especially in preparation for my final defense, than I could alone. I am fortunate to have her in my life. Without her understanding, help and support I would not be able to complete this dissertation.

Preface

In this research project, a novel bio-mimetic electrostatic micro-hydraulic (EMH) structure that significantly improves the performance of many MEMS sensors and actuators is introduced. The EMH is a new paradigm in MEMS devices that can replace piezeo-electric or electromagnetic sensing/actuation mechanisms. The EMH sensing/actuation platform can be used in combination with application specific appendages to realize devices such as air flow sensors, tactile sensors, inertial sensors, valve arrays, micro-scale hexa-pedal robots and many other MEMS sensors and actuators. This structure consists of two chambers on front and back sides of a silicon wafer, connected through a channel and filled with an incompressible liquid. With a proper choice of the area ratio between the chambers, amplification of either force or displacement is achievable. This amplification, which is characteristic of the micro-hydraulic system, plays an essential role in improving sensor and actuator performance. A pair of electrodes on the back side are used for electrostatic actuation (which can provide internal pressure) or capacitive sensing. Various modeling and simulations have been used to optimize the EMH system for high-speed sensing and actuation. The optimized system has been fabricated and tested with improved bandwidth of about 60-70Hz, based on the EMH die size.

To demonstrate a high performance class of sensor, hair-like structures are considered to form appendages for functionalizing EMH systems. Biological hair is characterized by arrays of high aspect ratio, three-dimensional structures, with mechanical amplification of movement. Using hair in conjunction with the EMH structure, a new type of low power, accurate and robust

flow sensor has been fabricated. In this sensor, the hair is dragged by air flow and pushes the EMH structure's front side bossed-membrane, moving the liquid to the back side, thus deflecting its membrane, which is sensed electrostatically. The hair and boss structure are optimally designed to maximize the sensor response to a given flow speed. Stereo-lithography has been utilized to precisely fabricate the 3D hair-boss structure. Additionally, an array of four sensors is used to realize 2D directional sensing. Compared to conventional capacitive air flow sensors, the EMH system expands the measurement range while maintaining the same sensitivity. The capacitive transduction sensor is lower power compared to commonly used hot-wire anemometers or other thermal sensors. In addition, since capacitive gaps of the front and back side chambers are enclosed, the system is more robust to environmental pollutants, such as debris, oil and water droplets, etc. The hair-like micro-hydraulic air flow sensor detects flow speeds ranging from 0 to over 15 $m.s^{-1}$ (our measurement tools limit) with a resolution of 1.7 $mm.s^{-1}$, an extrapolated minimum detectable speed of lower than 2 $mm.s^{-1}$ and angular resolution of 13°. This corresponds to about 78.9 dB of range to minimum detection ratio, which is the highest range over resolution ratio to best of our knowledge. Additionally, this sensor has the lowest minimum detection for external DC air flow velocities.

Using the EMH system, a highly sensitive tactile sensor has also been designed and fabricated with the same spatial resolution as human skin. Instead of hair-boss appendage atop the EMH system, plunges are used to apply touch pressures on EMH. The plunges are optimized to allow for maximum range without damaging the EMH front side membrane. Similar to hair flow sensors, the tactile sensor application specific appendage is formed with stereo-lithography fabrication technique. The sensor is capable of delivering high average sensitivity of 87 fF/mN (maximum observed: 260 fF/mN), a minimum detectable capacitance change of 80 aF at

quiescence and a spatial resolution of 1 mm. It is sensitive enough to detect the fall of a 38.5 nL water droplet. The sensor full-scale force range with a 2-μm thick parylene membrane is 15 mN. With an array using 15 μm thick parylene, the full-scale range can be expanded to 180 mN.

Basic EMH actuation mechanism has been also demonstrated in this dissertation. In the actuation mode, a voltage is applied on the back side capacitor of an EMH system, and the metal plate on the flexible membrane is actuated electrostatically. The membrane deflection pushes the liquid to the front side. Depending on the surface area ratio of the front to the back side, amplification of either force or deflection is made possible. A curved-electrode capacitive actuator with a diameter of 4.47 mm driven at 200 V produces 94.3 μm deflection on the front side at 12.3 kPa of pressure which corresponds to 38.6 mN force generated by the capacitive actuator on the back side. Actuation occurs from DC to 10-15 Hz, depending on device geometry. Realization of locomotion patterns is also achievable using micro-hydraulics. Founded on hydraulic amplification of deflection concept, an innovative type of actuator can be designed and fabricated, which moves a hair out of the substrate plane, resembling a 3D micro-size strider leg. The actuator uses electrostatic actuation to deflect a parylene membrane and an off center positioned hair. This hair can be used as a leg when flipped over. An array of legs can be arranged in a way to imitate a bio-mimetic tripod gaits and essentially implement a micro-size hexa-pedal robot locomotion pattern. The prototype actuator shows 40μm deflection at the tip of the hair with a maximum bandwidth of 10Hz and each cell can carry up to 300 mg of weight which is 5× of its body weight.

Table of Content

List of Tables

List of Figures

Abstract

A novel, optimally-designed micro-hydraulic structure is introduced to significantly improve performance of many MEMS devices for sensing and actuation. The micro-hydraulic system in conjunction with application-specific appendages can realize high performance sensors and actuators. For instance, biomimetic hair-like structures can provide external air flow sensing with high accuracy and high resolution that can replace bulky, high power and fairly low-resolution hotwire anemometers or other conventional sensors in most applications. Moreover, 3D hairs with small footprints enable dense array fabrication to provide redundancy, fault tolerance and directional sensitivity. Previous works using hairs with piezo-resistive or capacitive transduction have very fragile structures that limit the use of the air flow sensors in outside environments. Additionally, the high accuracy of these sensors is achieved at the expense of full-scale range. Using a micro-hydraulic structure a new type of low-power, accurate and robust flow sensor has been fabricated and tested in which a hair-like appendage is used to translate flow into hydraulic pressure. This pressure is sensed with an integrated capacitor within the micro-hydraulic system by which the sensitivity is amplified. The air flow sensor detects flow speeds ranging from about $2 mm \cdot s^{-1}$ to over $15\ m \cdot s^{-1}$ with a resolution of $1.7\ mm \cdot s^{-1}$. This corresponds to about 78.9 dB of range to minimum detection ratio, which is the highest range over resolution ratio to the best of our knowledge. An array of sensors allows 2D directional sensing with minimum 13° angular resolution. This enables utilization of the hair sensors for state estimation and wind gust rejection when integrated with micro-air-vehicles.

The micro-hydraulic structure can also be used as a platform to realize many cross-disciplinary high performance devices. This platform has been used to make tactile sensors that are needed in humanoid robotics, providing performance similar to human skin. Additionally, these structures have been tested in actuation mode to form micro-valves for micro-fluidic circuits and have the ability to provide hexa-pedal locomotion for micro-scale robotic applications. With use of proper appendages, devices such as shear stress sensors, 3D accelerometers, 2D gyroscopes, active flow controllers or tri-gait locomotion actuators can be realized.

1 Chapter 1: Introduction

In this research work, the Electrostatic Micro-Hydraulic (EMH) system as a novel sensing/actuation unit is studied. This transducing platform can be used in combination with application specific appendages, such as bio-mimetic hair structures, to realize high performance MEMS sensors and actuators.

Actuators with capability to provide high force or large deflection are critical for devices such as valves and pumps used in microfluidic systems, for surface bump manipulation in tactile displays, and for micro-airfoil control. Table 1.1 compares features of various conventional actuation methods.

Table 1.1 Comparison of several actuation methods.

	Electrostatic	**Hydraulic**	**Piezoelectric**	**Pneumatic**	**Electromagnetic**
Force	Low	High	High	High	High
Deflection	Small	Large	Small	Large	Large
Fab. & Materials	Easy	Difficult	Difficult	Difficult	Difficult
Power	Low	High	Low	High	High
Control	Easy	Easy	Medium	Easy	Hard
Speed	Fast	Medium	Fast	Slow	Fast

Electrostatic actuation, the most commonly used actuation technique, cannot provide the high force (~10-100 mN) and high deflection (tens of microns) required for many applications. Other conventional high force mechanisms either suffer from control complexity (e.g. electromagnetic) or process integration issues (e.g., piezoelectric). Previously studied micro-hydraulic systems depend on an external source of actuation [1], suffer from poor liquid encapsulation technique, are not suitable for parallel micro-fabrication processes [2] or exhibit poor performance, such as

cross talk between adjacent cells in an array or low speed [3]. This raises a need for a new class of actuators that offers controllable and high force actuation, which can be delivered across a large displacement range. In this research, the approach is to overcome this challenge by assisting electrostatic actuation with hydraulic amplification that can result in either large deflection or high force. This architecture is called Electrostatic Micro-Hydraulic (EMH) actuator. The EMH structure consists of two chambers, one on the front and one on the back sides of a silicon wafer, connected through a channel and filled with an incompressible liquid, with higher permittivity than air. The chambers are capped with flexible membranes and a pair of electrodes forms a capacitive actuator on the back side, as an integrated drive force. With a proper choice of the area ratio between the chambers, amplification of either force or displacement is achievable. Figure 1.1-A schematically shows the concept of EMH actuation.

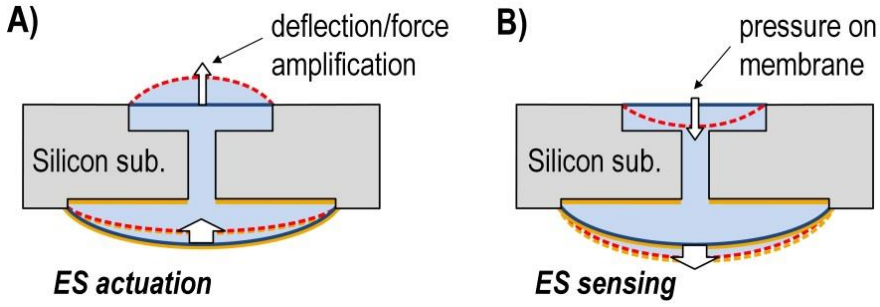

Figure 1.1 Electrostatic Micro-Hydraulic (EMH) structure for sensing and actuation.

The EMH structure can be used for sensing as well, in that the capacitor on the back side senses the deflection caused by pressurized front side chamber (Figure 1.1-B). Application specific appendages convert the measurand (e.g. flow velocity) to pressure exerted on the front side. Compared to air-gap capacitive sensors, sensitivity is improved by EMH structure, since the high permittivity liquid increases the base capacitance. Moreover, EMH allows for large range and high sensitivity simultaneously, because the measurand input and capacitive sensing sites are spatially separated. Additionally, EMH improves robustness of the sensing element,

since the capacitance gap is enclosed, enabling its deployment in harsher environments as opposed to well-controlled lab spaces.

To functionalize EMH structures for various sensing and actuation applications, hair-like appendages can be utilized. Hair-like structures are characterized by arrays of high aspect ratio, three-dimensional microstructures, with mechanical amplification of movement and local neural (i.e., electronic) integration. These structures are widely used in nature for environmental sensing, thermal isolation, mechanical filtration, inertial sensing and navigation systems [4, 5, 6, 7]. Utilizing bio-mimetic hair-like structures, a variety of devices can be realized, such as flow, tactile and inertial sensors or small strider leg and many other forms of actuators. In this research, hairs are designed to be integrated with EMH to realize high-performance hair-like air flow sensors (HAFS).

One application for HAFS introduced in this work is to operate on mobile micro-autonomous platforms such as those developed under the Army Research Laboratory's Micro Autonomous Systems & Technology (MAST) program. The MAST mobile platforms consist of micro-air-vehicles (MAVs) [8], micro-rovers or micro-crawlers [9], which are meso-scale, lightweight robots, with limited payload and power budget of tens of grams and few micro-watts, respectively. Sensory systems for dynamic robot control, mapping and navigation, and situational awareness of these vehicles are needed. Due to their very limited payload capacity, off-the-shelf components are challenging to integrate [8, 9]. For some applications such as directional air flow or wind-gust detection there are no commercial parts available even if size and weight constraints are relaxed. This motivates us to investigate a new class of sensors that can offer high speed, small size, high resolution, low power and wide dynamic range. Utilizing

the same platform, an array of force sensors with ability to provide spatial resolution similar to that of human fingertip has been investigated.

1.1 Background

1.1.1 Micro-Hydraulic Systems

Hydraulic structures (Figure 1.2) are being extensively used in many systems where amplification of force or deflection is needed. The principle of operation is based on uniform distribution of pressure over an incompressible liquid, filling two connected chambers [10]. Amplification of either force or deflection is made possible by taking advantage of unequal surface areas of two movable pistons/membranes capping the chambers. For instance, if a force is applied to the large-side membrane, knowing the fluid is incompressible, the same pressure is applied on the small-side membrane. Therefore, by conservation of work, the ratio of membrane deflection should be inversely proportional to their surface area ratio or the applied force, i.e. $F_S \times d_L = F_L \times d_S$ (shown in Figure 1.2).

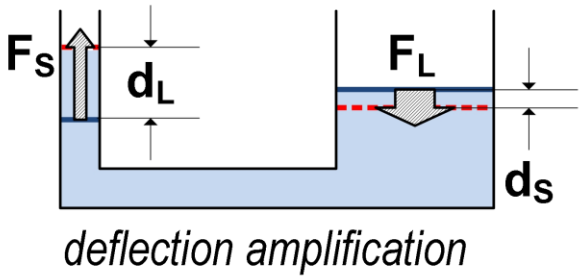

Figure 1.2 Basic hydraulic structure, deflection amplification. A large force is applied on the larger side, the deflection is amplified on the smaller side.

Application of hydraulic (or similarly pneumatic) systems in microstructures can drastically enhance performance of a class of MEMS devices. There have been some efforts in exploiting hydraulic systems in micro-scale levels [1], however, almost all presented devices amplify deflection or force generated by an external source through a micro-hydraulic system. In some

cases, although inflation of flexible chambers or membranes is utilized to generate large displacements, these instances depart from amplification of deflection concept in hydraulic systems [11, 12, 13].

In recent developments, two cases are introduced that investigate amplification of deflection through micro-hydraulic systems. The first one uses such systems for Braille code display realization [14, 15] and the second one to form piston arrays to operate as an all electrically controllable valve matrix for micro-fluidic circuit operation [3].

Braille code display by *Miki et al.* system is shown in Figure 1.3. An array of micro-hydraulic cells is mounted on a corresponding off-chip piezo-electric piston bed. The piezo-electric actuators are pre-fabricated components and the role of micro-hydraulic system is to compensate for small deflection of the piezo-electric piston. Although this technique offers a large deflection amplification of about 10× at 70 Hz, its fundamental dependence on external actuation source limits its applications. Additionally, the power consumption is high (tens of mW) and its integration capability with other MEMS systems is very limited.

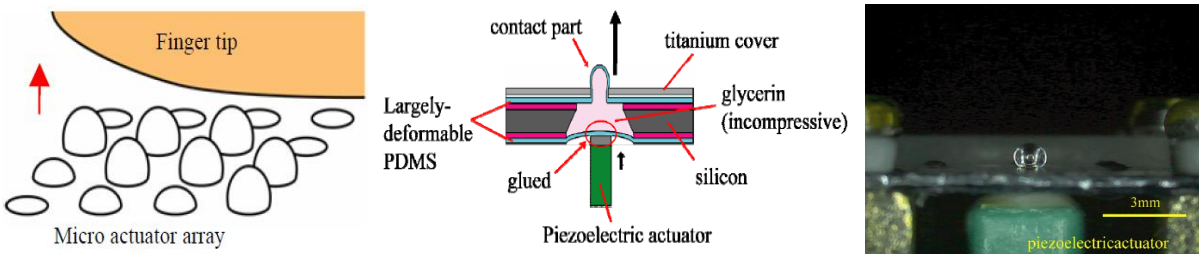

Figure 1.3 Left: schematic image of a tactile display. Middle: schematic image and (Right) photo of a Braille code display cell [14].

All-electrically driven micro-hydraulic piston array [3, 2], shown in Figure 1.4, introduced by H. S. Kim (Univ. of Michigan Alumnus, 2006) is the first device where integration of electrostatic actuation with micro-hydraulic structure is exhibited. A piezo-electric actuator film attached to one side provides the driving force in this work. Electrostatic latching (Figure 1.4)

amplified by high permittivity of the hydraulic carrier fluid (DI water in this case) is used to control array operation, i.e. to select which membrane should be deflected when the driver membrane is actuated. The array is operated up to a frequency of 2 Hz without failing, while allowing control over individual cells by utilizing electrostatic latching at 100 V-DC. The active device part measures as 8.4×8.4×0.65 mm^3. Some aspects of this work, such as manual liquid encapsulation, crosstalk between cells, low operational speed, and dependency on external piezo-electric driver are subject to improvement.

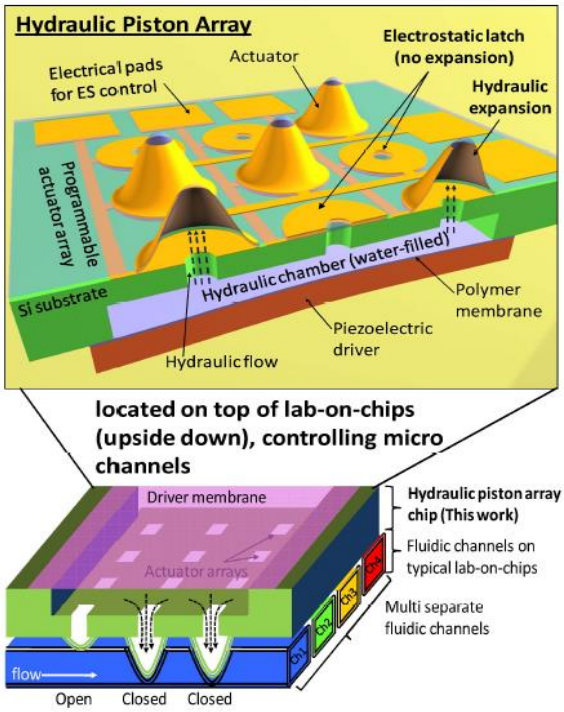

Figure 1.4 Illustration of (Top) micro-hydraulic actuator arrays, (Bottom) the application: simple generic microfluidic manipulation platform. Note electrostatic latching is shown in the top image [3].

Table 1.2 compares the features of both Braille code display and micro-hydraulic piston array and the fabricated EMH presented in this work. Table 1.2 clearly shows substantial improvement of the micro-hydraulic system in this research, namely its bandwidth, crosstalk, fabrication reliability, reproducibility and power consumption. It should be noted that a very important aspect of the EMH is its capability to be operated in the sensing mode, which makes it

a unique platform for realization of MEMS sensors and actuators in comparison with piezo-electric, magnetic or conventional electrostatic transduction mechanisms.

Table 1.2 Comparison of characteristic features of three classes of micro-hydraulic structures.

	braille code display	**μ-hydraulic piston**	**EMH (this work)**
Transduction mechanism (actuation)	Piezo-electric	Piezo-electric & Electrostatic	Electrostatic
Integrated drive force	No	No	Yes
Band width	70 Hz	2 Hz	70 Hz
Sensing mode of operation	No	No	Yes
Crosstalk	Low	High	Very Low
Batch fabrication	No	No	Yes
High dielectric material	N/A	Yes	No, but can be used
Power consumption	High	High	Low
Scalability	No	No	Yes
Hydraulic fluid	Glycerin	DI Water	Silicone oil
Structural material	PDMS	Parylene	Parylene

1.1.2 Hair-like Air Flow Sensors

Flow sensors in the literature are usually utilized for mass-flow measurement and are often used in tubular structures. There are a few types of sensors that can measure wind speed or detect gust, such as hotwire anemometers. This type of sensor suffers from large size and high power consumption and generally poor resolution. Another class of air flow sensors that is recently being investigated is hair-like sensors that can be used for wind speed measurement or wind gust detection. Hair-like air flow sensors are studied by a few research groups [16, 17, 18, 19]. In this sensor architecture, the hair is dragged by flow of the fluid it is immersed in and the drag force is sensed by piezo-resistive [20, 21] or electrostatic elements [22, 23].

Many instances of "hair sensors" are made out of a planar structure that is formed on a wafer surface and moved out of plane [24, 25]. Figure 1.5 shows an example of such a sensor, where a cantilever beam is curled out of the plane due to thin film residual stress. Although in literature they are referred to as hair sensors, they depart from the concept of utilizing the third dimension

to save chip area, allowing dense array formation and providing redundancy. In this research, similar to hair formation described in [21] and [23], the hair structure is formed on top of the wafer, without using the chip area. Stereo-lithography technique has been used to form complex 3-dimentional structures, extended above the wafer plane, for optimal performance of the resultant hair-like air flow sensors. This technique does not consume any excess chip area, as the hair structure is a post-fabrication addition to the EMH structure.

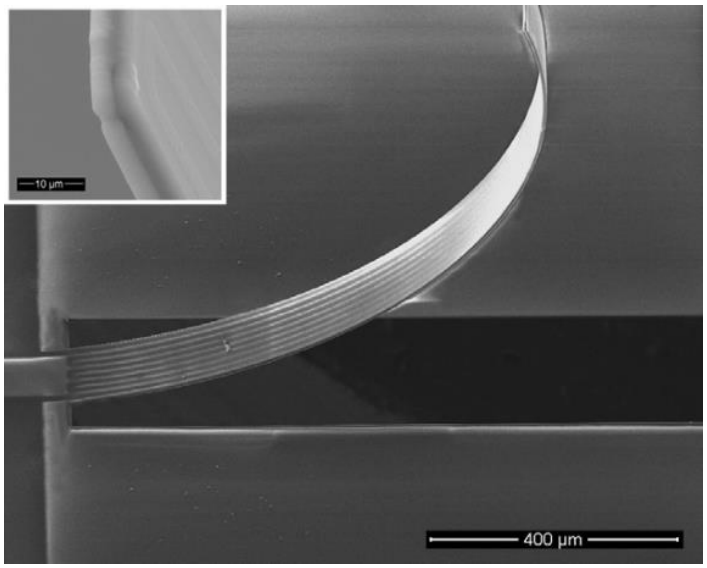

Figure 1.5 Stress driven "hair" flow sensor formed by parylene coated AlN-Si cantilever beam [25].

Piezo-resistive hair-based sensors (Figure 1.6) have been extensively investigated by *C. Liu et al.* [21]. In this type of air flow sensor, the hair sits on a plane held by two narrow cantilever beams whose dimensions are optimized to result in maximum sensitivity and range [21]. As the hair is dragged by fluid flow, it is deflected and the change in stress, which is proportional to the flow speed, is measured by piezo-resistive parts embedded on the cantilever. A Wheatstone bridge is made on the MEMS die with the same piezo-resistive material for the sensor readout.

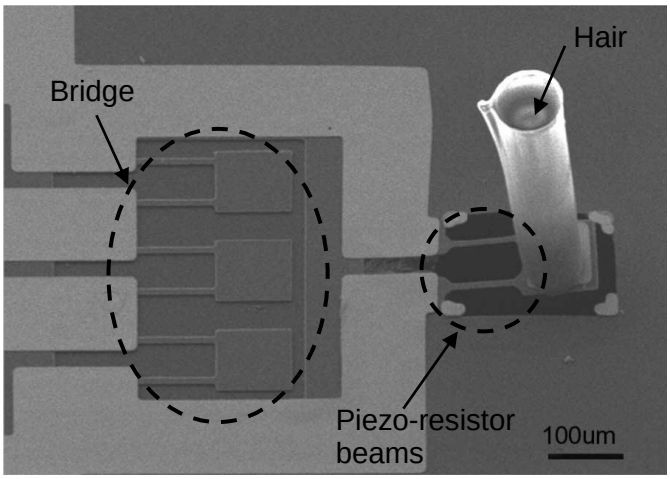

Figure 1.6 Piezoresistive based hair flow sensor [21].

The latest results indicate that *C. Liu et al.* have achieved DC flow sensitivity of 50 mV/(m/s) with full-scale range of slightly less than 20 m/s for air flow. These test results were obtained under 1.25-V excitation voltage and 1000 times signal gain. The sensor also shows directional sensitivity and their measurement results indicate angular resolution of 2-3°. Figure 1.7 shows sensor response to air flow and its cross axial sensitivity. Generally, piezo-resistive based sensors suffer from low sensitivity. Moreover, the fragile narrow cantilever beam makes the sensor prone to damage when it is used outside of the well-controlled lab space which limits the application of the sensor in harsh environments. The sensor is designed for underwater applications to mimic lateral line of fish [26].

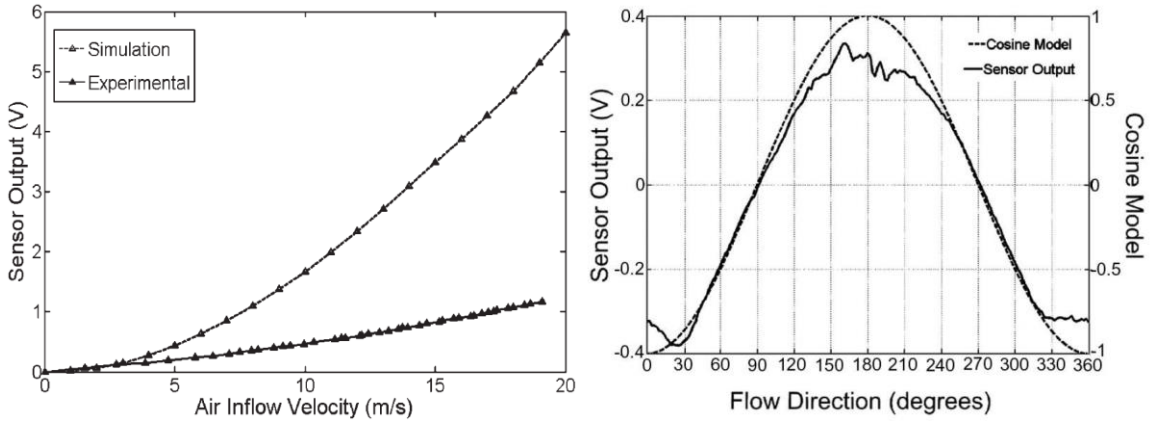

Figure 1.7 Left: sensor response to air flow at 1.25V excitation. Right: sensor directional sensitivity [21].

Capacitive based hair sensors (Figure 1.8, left) are broadly investigated by *G. J. M. Krijnen et al.* [22]. In this class of sensors, the hair is located on a membrane, containing two very narrow gap capacitance plates, and measured change in capacitances as a result of flow-induced drag force is related to flow speed. Using two out-of-phase AC voltage sources as the carrier signals, differential capacitance changes modulate the amplitude of the carrier signal (AM signal). A circuit that consists of a multiplier and a low pass filter demodulates the AM signal to recover the sensor response to flow velocity. This flow sensor operates with a high bandwidth (about 3 kHz) and offers a very high resolution (sub cm/s) at the expense of very limited full-scale range (< 0.5 m/s). *G. J. M. Krijnen et al.* has not explicitly reported their sensor's full-scale range, however, the maximum range in their plots is 20 cm/s. Figure 1.8-right shows the response of arrayed hair sensors (referred to as "previous hair sensor"), and single hair sensor along with their minimum detection level. The "single hair sensor" architecture is two perpendicularly aligned sensors on a substrate, which exhibits lower noise level.

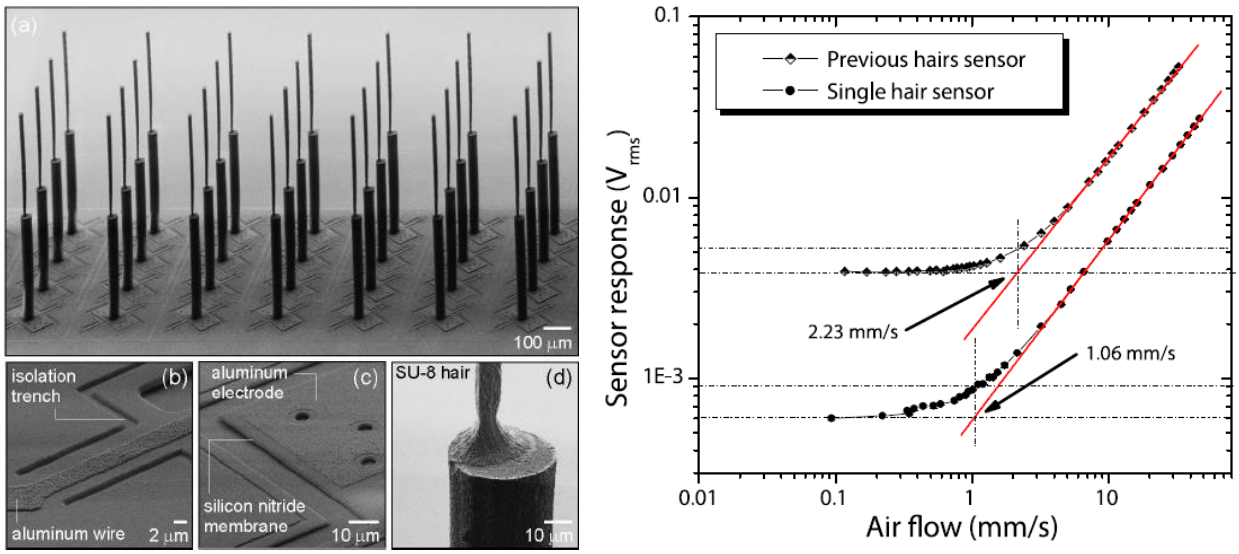

Figure 1.8 Left: Fabricated array of capacitive hair flow sensor [22]. Right: arrayed (previous) and single hair sensor response to an AC flow at 250 Hz [27].

From the experimental results, it is clear that the capacitive flow sensors usually trade off measurement range with resolution, i.e. a highly sensitive sensor has poor full scale range and vice versa. For applications in which external air flow measurement is needed, such as wind detection and gust rejection, sensors with both large range and high sensitivity are required. In addition, *G. J. M. Krijnen et al.'s* hair sensor, and almost all conventional capacitive based flow sensors, utilizes exposed electronics that limits their use in outside of the lab environment. For instance in moist or particle-abundant areas, capacitive gap might be filled with water or clogged with dirt, which can significantly affect the sensor performance if not cause sensor failure. Therefore, there is a need for a sensor with high resolution, large dynamic range, low power, fast time response and robust architecture. This thesis describes how combining hair-like structures with an EMH system can result in a new sensor to satisfy all the desired requirements.

Table 1.3 compares various features of sensors presented by *C. Liu et al.*, *G. J. M. Krijnen et al.* and this work. Note that the range to minimum detection ratio has significantly improved by EMH hair sensors. This sensor has a more robust structure and can be deployed in harsh environments. Moreover, due to novel stereo-lithography fabrication technique, longer hairs are possible to realize, which can drastically improve the minimum detection of the sensors.

Table 1.3 Comparison of characteristic features of three types of hair-like air flow sensors.

	C. Liu. et al.	**G. J. M. Krijnen et al.**	**This work**
Sensitivity	50 mV/(m/s)	-	46 fF/(m/s)
Resolution	-	-	2 mm/s
Min. detection	5 cm/s	~ 1 mm/s	1.7 mm/s (projected)
Range	19 m/s	20 cm/s	> 15 m/s
Range/min. detection	51.6 dB	46 dB	> 79 dB
Power	High	Low	Low
Transduction	Piezo-resistive	Capacitive	Capacitive-hydraulic
Bandwidth	N/A	3 kHz	70 Hz
Hair material - fabrication technique	SU8 - conventional lithography	SU8 - conventional lithography	Accura® ClearVue - 3D stereo- lithography
Hair height limit	0.7 mm	0.95 mm	< 10 mm
Robustness	Low	Very low	High

1.2 Research Objectives

Micro-hydraulic structures and devices are a new concept in MEMS community. Tremendous amount of time and effort are dedicated to make a reliable and useful micro-hydraulic technology that can serve as a platform for realization of many devices, such as air flow, tactile and inertial force and sensors.

The objective of this research work is to develop EMH systems, along with application specific appendages to functionalize the EMH for high performance sensing and actuation (Figure 1.9). To perform this task, the following topics are investigated:

- **Materials**: study of material for hair, fluid for reliable liquid encapsulation.
- **Micro-hydraulics**: formation of hydraulic structure, geometry optimization.
- **3D Process:** development of 3D process for appendage addition.
- **Functionalization**: integration of sensing/ actuation appendages for device operation.
- **Circuit integration**: distributed local transduction or control with CMOS elements integrated with micro-hydraulic systems.
- **Array**: high redundancy system, fault tolerance increase, 2D or 3D information extraction.

For this thesis, all the listed items, except for integration of the micro-hydraulic based devices with CMOS interface circuitry, are investigated. The fabrication process, however, allows for integration of the EMH with distributed CMOS circuitry. Due to fabrication consistency, the CMOS integration may be performed with minimal design modifications.

Liquid encapsulation technique plays a very critical role in realization of the micro-hydraulic system. Two packaging methods are studied and described in Chapter 2. In Chapter 2, the effort to fabricate the micro-hydraulic structure based on liquid encapsulation technique has been also

explained. Characterization of the micro-hydraulic system in actuation mode is also presented in this chapter. Chapter 3 describes the analysis performed on the first generation micro-hydraulic system. Second-generation micro-hydraulics, an optimally designed EMH using sloped-wall architecture, along with fabrication method and test results are presented in this chapter as well. Chapter 4 demonstrates fabrication, characterization and analysis of the first and second generations of hair-like air flow sensors (HAFS) based on a micro-hydraulic system. In Chapter 5, fabrication and characterization of force sensor arrays, another device based on EMH platform is reported. Finally, in Chapter 6, the thesis is concluded and future work is proposed. In Appendix, a novel hair-like hotwire anemometer is introduced and the results are presented.

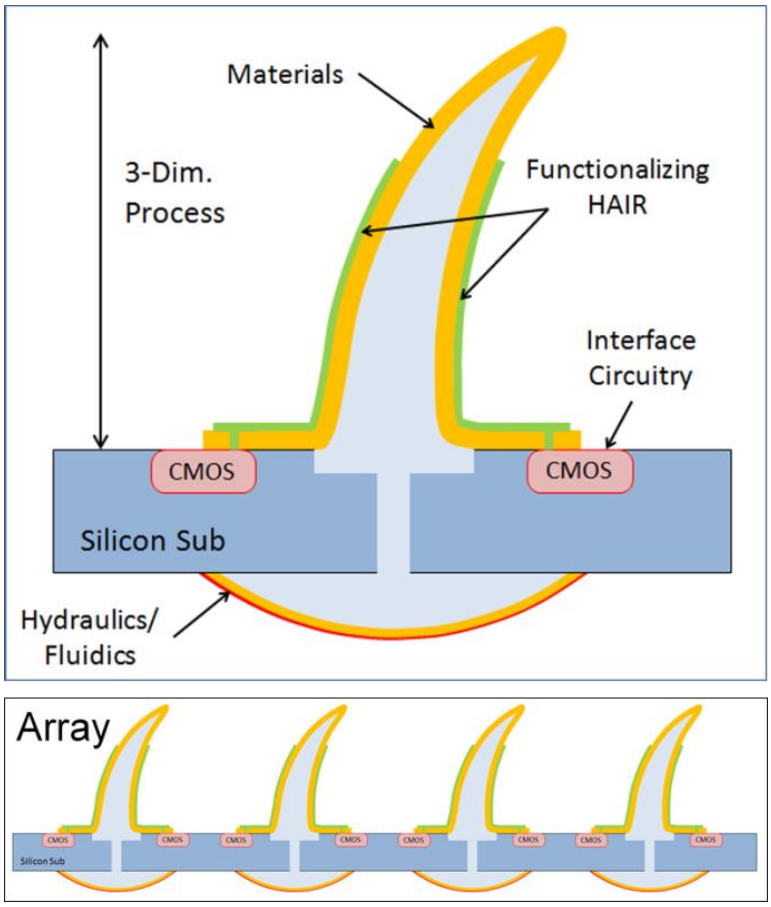

Figure 1.9 Micro-hydraulic device vision.

1.3 Summary of Contributions

In summary, the objective of this research work was to develop micro-hydraulic systems for high performance sensing and actuation, as well as a theoretical model for performance analysis. The major contributions of this thesis were:

- Development of a micro-hydraulic structure with integrated electrostatic element for sensing and actuation.
- Introduction of a robust, high-sensitivity, large dynamic range and high-speed hair-like air flow sensor based on micro-hydraulic system with wafer level fabrication process.
- Development of a multidimensional model for analysis and design of micro-hydraulic based devices.

2 Chapter 2: Basic Electrostatic Micro-Hydraulic (EMH) Structures

In this chapter the requirement for an encapsulation technique for formation of EMH structures are explored in the beginning. Liquid encapsulation methods in literature are briefly discussed and after those, two methods that are studied in this research are introduced. These novel methods are laser-assisted parylene bonding and direct deposition of parylene on liquid. Based on the latter, micro-hydraulic structures are fabricated. Finally, basic actuation mechanism of EMH is shown and characterized.

2.1 Wafer Level Liquid Encapsulation Methods

In order to fabricate micro-hydraulic structures, a reliable liquid encapsulation is needed. The encapsulation technique is preferred to be either wafer level or batch process. For optimal performance of the EMH structures, longevity of the sealing is important as well. At least one side of the sealing structure is required to be made of a flexible material, e.g. a polymer, and sealing structure cannot be conductive (since it will cause short circuit in final EMH).

There are few liquid encapsulation methods introduced in the literature. *S. Matsumoto et al.* have suggested high-pressure polymer-to-polymer bonding and self-sealing stiction valves [28]. Figure 2.1-left shows process steps for high-pressure polymer-to-polymer bonding. In this method, silicon molds, defining the chambers containing liquid, are made by DRIE on a blank silicon wafer. The mold and a blank Pyrex wafer are coated with a 4μm thick parylene-C layer. After the parylene coating, chambers are filled with liquid (DI water in this case) and the Pyrex wafer caps the chambers formed on the silicon mold. At 200~220°C and under 2.3 MPa

pressure, parylene layers form a bond and seal the liquid in between. Since the bonding is performed under high pressure, DI water does not evaporate. Figure 2.1-right shows samples of encapsulated liquid. This technique cannot be utilized for EMH fabrication due to its low efficiency (below 50%) and very short lifetime (a few hours) [28].

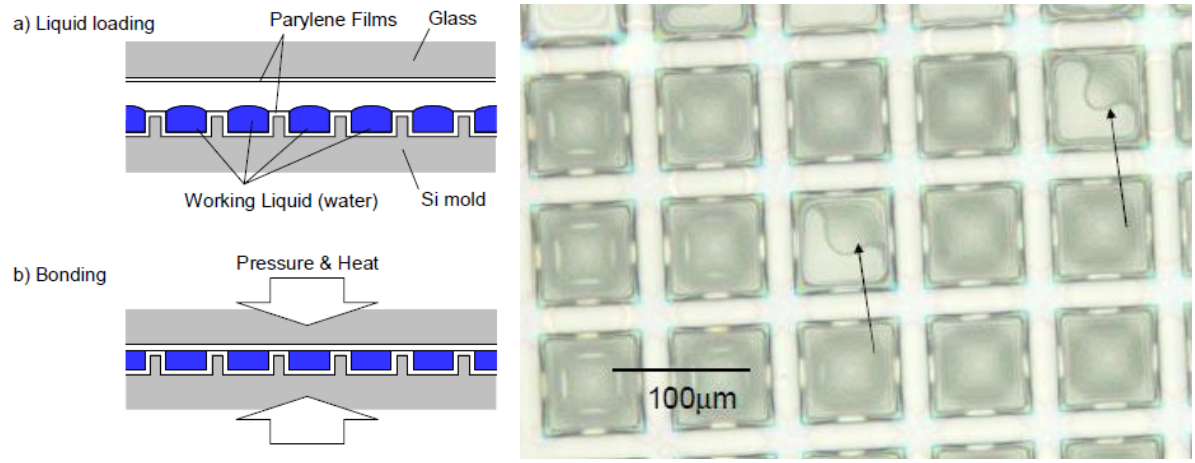

Figure 2.1 Left: basic process flow. Right: optical images of parylene cavities containing DI water. Arrows show liquid-vapor interface [28].

Self-sealing stiction valves are first introduced by *S. Matsumoto et al.* [28] and improved by *C. A. Gutierrez et al* [29]. The principle of operation is shown in Figure 2.2-left [29]. As shown in this Figure, once the chambers are filled, the liquid starts to evaporate through the peripheral access ports. However, the evaporation moves the liquid front toward the valves. Once the front reaches the movable section of the valve membrane, capillary force pushes the membrane downward, which closes the valve and entraps liquid inside the chamber. The authors have tested this structure with DI water, which can be held inside the parylene chambers for approximately 8 hours. Figure 2.2-right shows a comparison between evaporation rate of chambers with and without stiction valve. The lifetime of the sealing in this method is too short for EMH application.

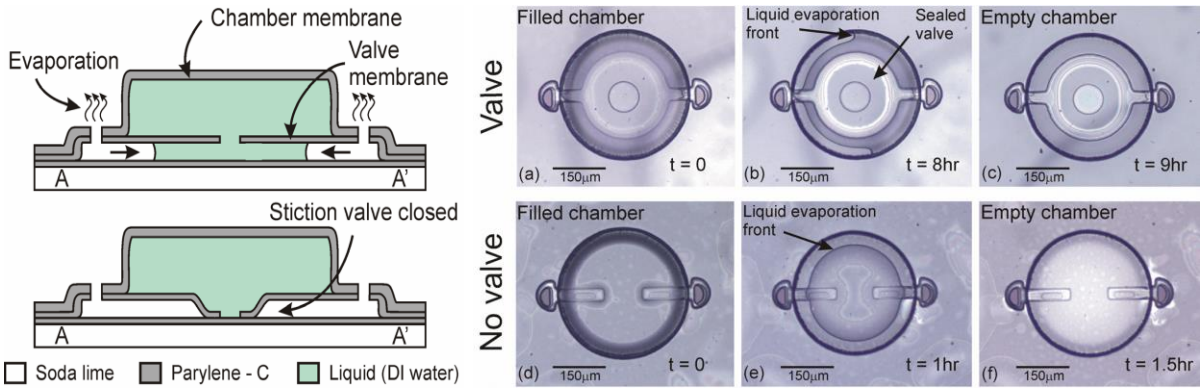

Figure 2.2 Left: stiction valve principle of operation. Right: comparison between evaporation rate of DI water of chambers with stiction valve and without stiction valve [29].

M. A. Lapisa et al. have used room temperature gold ring embossing for sealing of liquid reservoirs [30]. Figure 2.3-left shows process steps of this encapsulation concept. In this technique, 50μm wide and 30 μm tall gold walls are electroplated on a silicon substrate. Gold squeeze-rings are also electroplated on the lid silicon wafer, with height of about 3μm and various widths, ranging 3μm to 7μm. Once the liquid (ethylene-glycol) is dispensed inside the walls, the lid with squeeze-ring pattern on it covers the chamber. Using a bond aligner, the alignment is performed and 540 MPa pressure is applied to plastically deform the walls and seal the liquid inside the chamber. A low viscosity epoxy is applied to the chamber peripheral for mechanical support. The authors report 85% of the sealed chambers can maintain liquid after 24 hours in 10μtorr vacuum. Figure 2.3-right shows a sample of sealed liquid. Although this method has better efficiency and lifetime, a movable part cannot be easily integrated with the structure. Additionally, due to the nature of the sealing technique, bubble free encapsulation is hard to achieve, which it is critical for EMH application. A bubble free encapsulation is critical, because if an air bubble is entrapped in the system, the fluid inside the EMH is no longer incompressible. Also, its volume changes in response to temperature variations.

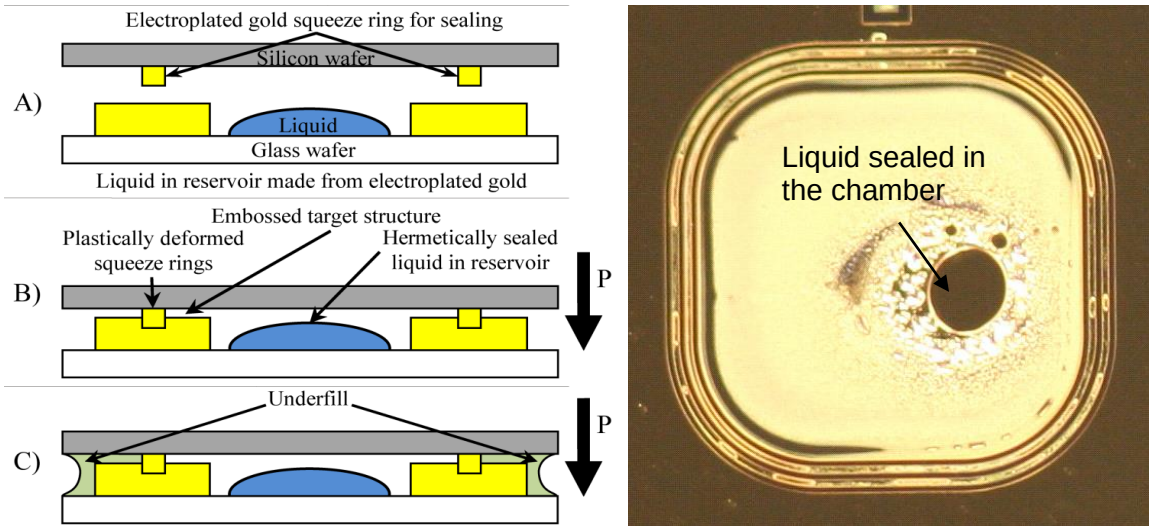

Figure 2.3 Left: room temperature gold ring embossing liquid encapsulation fabrication process. Right: sealed chamber after 24 hours of vacuum exposure. It is clear that the liquid has condensed on the glass inside the chamber [30].

There are instances of using UV curable adhesive for liquid encapsulation [31, 14, 15]. For example, *T. Ninomiya et al.* [31] used *UV Curing Silicone Resin 3164* to bond a PDMS sheet to a wafer with multiple cavities, in glycerin solution. Since the bonding process is formed inside the solution, the sealing is potentially bubble-free. However, it is reported that UV curable resins are water permeable [30], and they need manual manipulation of the samples, therefore, it is not a batch process.

The methods briefly reviewed above are not suitable for EMH fabrication. In this research work, laser assisted parylene bonding and direct deposition of parylene on liquid are studied for EMH formation.

2.1.1 Laser-assisted Parylene Bonding

This technique is based on local heating of the parylene layers with the absorption of laser pulse by intermediate layers of metals. The locally heated stack of metals provides enough energy to melt parylene layers in the vicinity of the laser pulse if they are under a certain amount of pressure. Under this condition, both polymer layers strongly bond to the metal to form a

parylene-metal-parylene bonded stack. Unlike other techniques [32], this mediated bonding method can be done in room temperature. The encapsulation methods either need a high temperature process or specific material properties [33] which both limit their application. This new method, however, provides low temperature bonding and choice of a wide variety of liquid types that gives a reasonable maneuverability in designing the hydraulic system of interest.

This bonding technique can be realized using the steps schematically shown in Figure 2.4. Two 1.5μm thick parylene layers are used in which the top layer (a free-standing layer in some configurations) is bonded to a second parylene layer coated on a silicon wafer with an intermediate layer of Cr/Au (500/2500A) on the bond-sites over the parylene. The upper parylene layer is pressed down (by 6.25MPa of pressure) with a glass stamp through which laser beam is directed. The exposure of the laser beam heats the metals and locally melts the parylene and makes strong bonds to the metal layers. By changing the laser power intensity, the amount of energy delivered to the bond site, and hence control over the temperature is achieved.

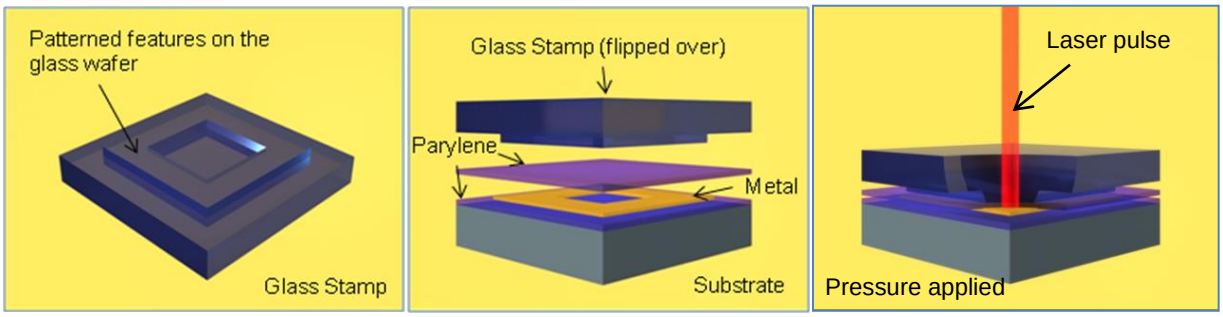

Figure 2.4 Laser assisted parylene bonding process applicable for liquid encapsulation. Left: glass wafer (stamp) with extrusions at bond locations. Middle: silicon substrate coated with parylene, absorbent metal layers and free standing parylene on top. Right: exerting pressure over bond area with the glass stamp. Local heating of the bond area with the laser pulse.

Various tests have shown that for this 532nm green laser, intensities ranging from 3.2 J/mm^2 to 4.0 J/mm^2 yield appropriate heat for bonding. The position of the absorbent metal layers was subjected to test as well, either underneath both parylene layers, or between them. In both cases,

formation of bond could be observed. However, the one with the metal in the middle of polymer layers is more likely to provide better bond strength, since the heat transfer through parylene layers is symmetrical. The parylene-metal-parylene configuration is used for further tests.

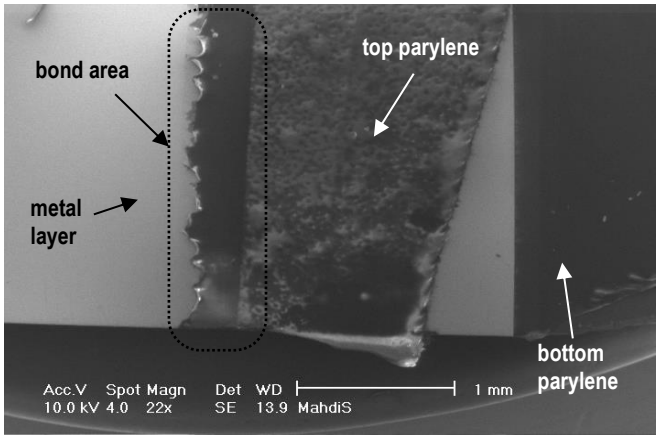

Figure 2.5 SEM image of a bonded parylene layer over another parylene with metal in between. The upper parylene layer is torn but not detached at the bond location, which is an indication of bond strength

Figure 2.5 shows a SEM image of the sample after laser assisted bonding. The bond is so strong that after detaching the upper parylene, the polymer sheet is torn at the bond interface while the bonded part is still intact. Encapsulation of air and water has also been tested with this technique by scanning a closed path with the laser pulse (Figure 2.6). For water encapsulation, a small droplet of DI water is dispensed over the substrate, atop parylene layer before pressing the upper parylene layer and then the laser beam is swept over the perimeter of the droplet. This forms an enclosed parylene chamber containing DI water. It is noteworthy that the parylene-to-parylene strong bond can still be maintained in presence of water. Therefore, bubble-free encapsulation is possible if parylene layers are bond while immersed in water (or other liquids).

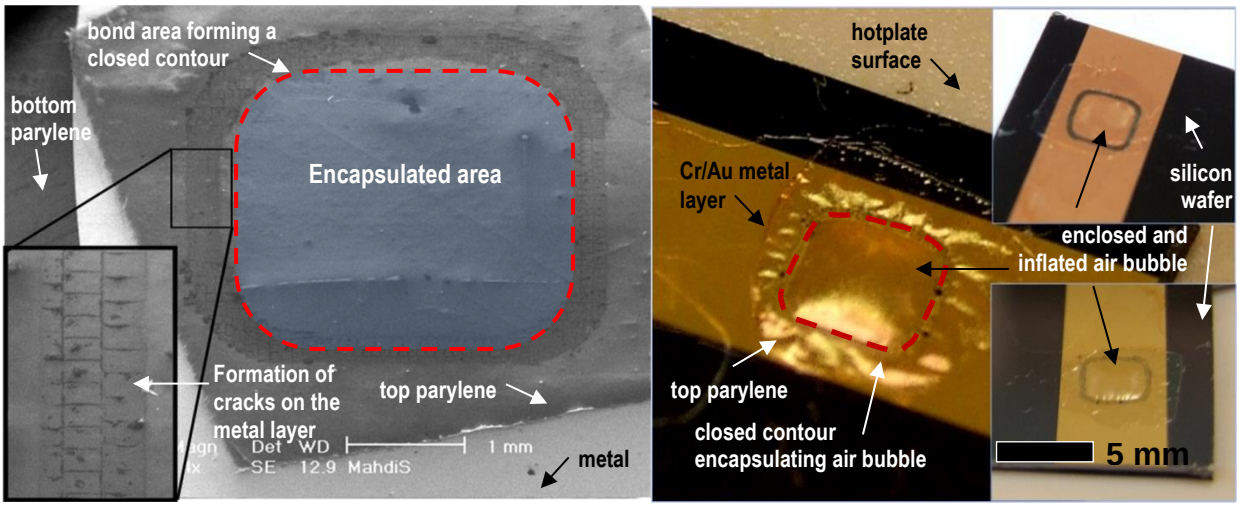

Figure 2.6 Left: Encapsulation of air using laser assisted parylene-parylene bonding. The formation of the cracks in the chamber sidewall can lead to leakage from the chamber. Right: Encapsulation of air. This picture shows the bulged parylene membrane due to expansion of the encapsulated air in this small chamber over a hotplate at 80°C.

The experimental results show that a water-filled chamber can maintain the water for a few hours. It is probable that by prevention of crack formation on the metal stacks in between the parylene layers, a better seal can be maintained. This improvement in the quality of the seal allows for a longer lifetime. These cracks (Figure 2.6-left) can be avoided by adjusting the metal layer thickness with respect to laser pulse energy. Figure 2.6-right shows a bulged parylene membrane due to expansion of the encapsulated air in this small chamber over a hotplate at 80˚C, which shows entrapment of an air bubble in between two parylene layers.

Direct Deposition of Parylene on Liquid

While the laser-assisted liquid encapsulation technique is promising, structures based on direct deposition of parylene on low vapor pressure silicone oils are also developed due to the ease of fabrication and repeatability of this method.

The chosen liquid material is 1,3,5-trimethyl-1,1,3,5,5-pentaphenyltrisiloxane, a type of silicone oil which has a vapor pressure at room temperature of under 1 mTorr, so that it can

survive the low vacuum inside the parylene deposition system (PDS) [33, 34]. After the oil is dispensed onto the wafer in the designated locations, the wafer is loaded in the PDS, and parylene is deposited. The polymer conformally coats the oil, encapsulating it [34, 33]. Note that no leakage or evaporation of the liquid is expected since the silicone oil does not evaporate at atmospheric pressure and room temperature.

Figure 2.7 shows pattering of the silicone oil by the means of a patterned layer of Cytop™ and a thin film of gold underneath. Cytop™ is an amorphous fluorocarbon polymer that is transparent and has low gas permeability. It is a hydrophobic spin-on layer that can be etched and patterned with an oxygen plasma ash step. It is clear from Figure 2.7 that silicone oil is contained in the Cytop™ free areas, i.e. rectangular boxes.

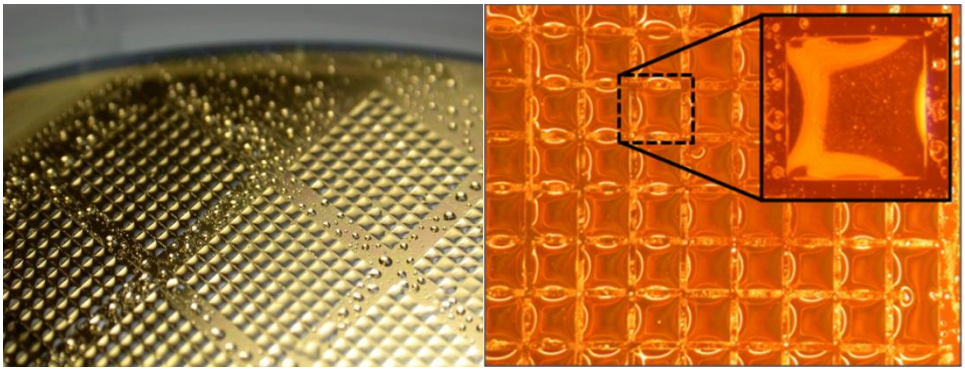

Figure 2.7 Patterning of the silicone oil with Cytop (hydrophobic) layer over thin film of gold. Residues over Cytop area can be avoided if the dispensing step is done with an inkjet printer. The sizes of the boxes are approximately 700μm with 150μm spacing. Parylene with 1μm thickness is coated over the liquid. The right image shows the top view.

This encapsulation method is used for fabrication of EMH structures presented in this research work, since it is a wafer level technique, a flexible membrane can be used as the movable parts needed for EMH and allows for utilization of various materials as long as they have low vapor pressure. Additionally, this method is a bubble free encapsulation because the parylene coats the liquid inside vacuum. The encapsulated liquid chambers have a very long

lifetime due to high stability of both parylene and the silicone oil in room temperature and atmosphere.

The direct deposition of parylene on liquid method is challenging in some aspects. This technique depends on use of low vapor pressure liquids, which have high viscosity by nature. The high viscosity causes large damping; therefore, lowers the device bandwidth. This issue is thoroughly investigated in Chapter 3. Additionally, it was observed that an air pocket entraps inside some devices with sharp corners and acute angles. This air pocket (or air multiple pockets) is so small that remains inside the device even under PDS chamber vacuum pressure of about 15mtorr. However, once the devices are processed inside lower pressure vacuum chambers (µtorr range), the entrapped air pocket largely expands. This expansion causes the parylene to deform plastically or in some instances rupture. To extract any entrapped air pocket after liquid dispensing, the devices are kept in the lowest vacuum pressure (µtorr range) for about 30 minutes. This helps the air pocket(s) escape from the deivce, and effectively de-air the silicone oil.

2.2 1st Generation Electrostatic Micro-Hydraulic Structure

Micro-hydraulic systems presented by *H. Kim et al.* [2, 3, 35] benefit from high dielectric constant of water, which amplifies electrostatic force. Although the experimental results demonstrate fully functional devices, this dissertation will address some issues associated with *H. Kim et al.* work. The main shortcomings of these devices are manual encapsulation of the fluid, limited lifetime (due to water evaporation through parylene membrane) and an inevitable cross talk between adjacent cells in micro-piston arrays [34]. Non-ideal sealing of fluid deteriorates the lifetime as well. As described in section 0, a very low vapor-pressure liquid that does not evaporate at room temperature/pressure and supposedly has infinite lifetime is to be

used for realization of EMH system. Moreover, the introduced wafer level bubble free liquid encapsulation technique enables dedication of individual driver for each cell in an array of actuator. With individual drivers, a common back side chamber, such as the one used in reference [3], is eliminated which effectively reduces cross talk.

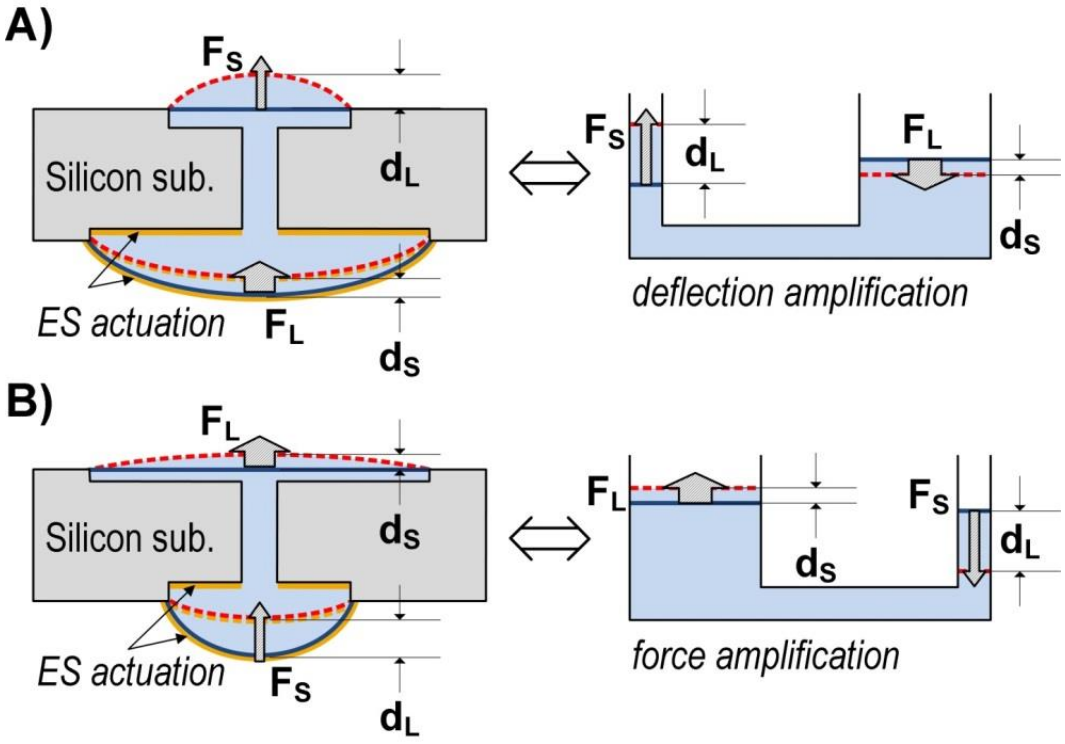

Figure 2.8 Schematics of (left) micro-hydraulic actuation and (right) generic hydraulic system for electrostatic actuation resulting in (A) amplification of deflection and (B) amplification of force, where L indicates the larger force or larger deflection and S indicates the smaller value.

Figure 2.8 schematically shows the concept of the EMH technology which assists electrostatic actuation with micro-hydraulic amplification to obtain large-force, large-deflection, and low-power actuation, along with hydraulic system analogy. Each actuator cell is made of two chambers on opposite sides of a silicon wafer capped by two parylene membranes. An etched-through-wafer channel connects top and bottom chambers. A pair of thin film metal electrodes on the silicon surface and parylene membrane allow electrostatic actuation (or sensing) on the back and/or front side of the wafer. Once one flexible parylene membrane is

electrostatically pulled down, the liquid is pushed through the channel into the opposite chamber, causing its membrane to be deflected out of plane. Similarly, with a proper choice of front to back side surface area ratio, amplification of either deflection (Figure 2.8 A) or force (Figure 2.8 B) is possible.

2.2.1 Fabrication

The fabrication process, shown in Figure 2.9, provides the option of having individually actuated chambers for each cell. It begins with formation of 3-4 μm dry etched silicon recess. This recess is utilized for curvature correction, which is described in Section 2.2.2.1. A stack of Cr/Au electrodes are then deposited by e-beam evaporator and patterned in a wet-etching step. Next, Cytop^{TM}, a hydrophobic layer, is spun, cured and patterned with oxygen plasma on both sides. Chambers and movable membranes are defined by the Cytop^{TM}-free areas, which will be covered with oil and then parylene in the succeeding steps. After deposition and patterning of Cytop^{TM}, a through-wafer DRIE step forms the channel connecting the front and back side chambers. The silicone oil is then dispensed and is contained in Cytop^{TM} free areas. The surface tension (silicone oil: 34.3 mN/m) at the back side and the weight of the liquid are in balance, thus after filling both chambers and channel, the dispensed liquid is held in place. The volume of the hydraulic chambers can be adjusted by dispensing controlled amount of liquid. Additionally, after liquid dispensing, the droplets heights can be made uniform by removing excess liquid of some cells using a stamp with a pre-adjusted gap over the chambers area. The wafer is then loaded in the parylene tool deposition chamber and in a single parylene deposition run the dielectric liquid is encapsulated on both sides.

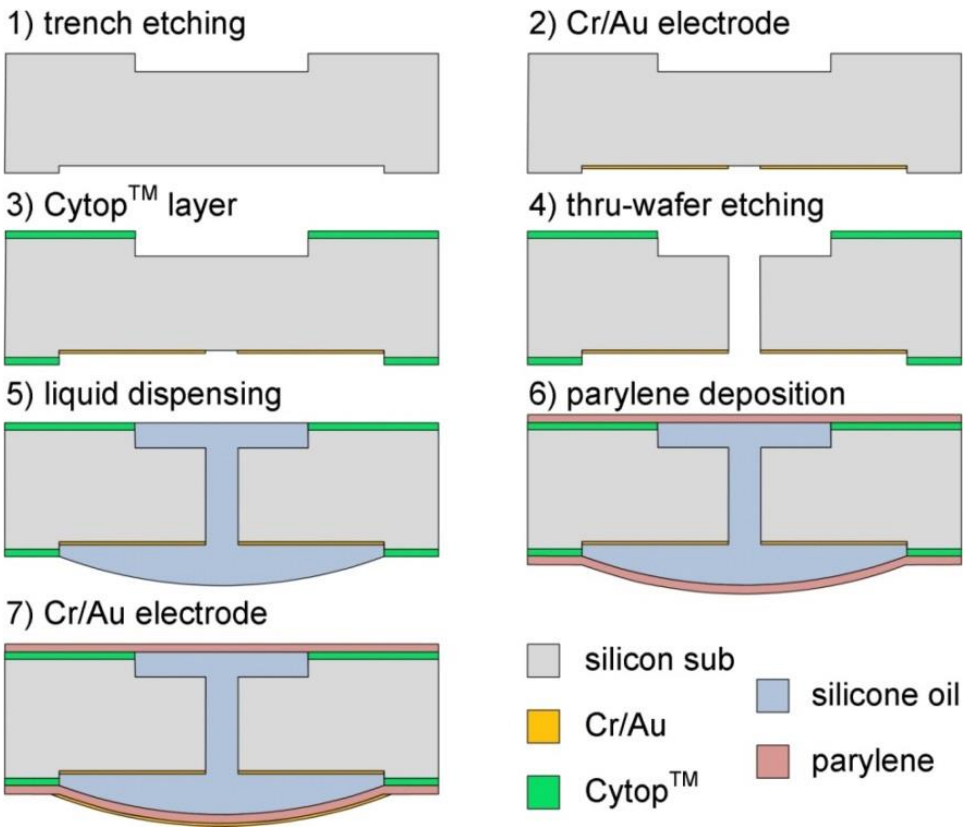

Figure 2.9 EMH fabrication process. Recesses on the front and back sides are utilized for curvature correction. Metal electrode on the parlyene layer forms the second electrode of the back side capacitor.

Figure 2.10-A and Figure 2.10-B show the top and bottom view of one of the actuators arrays after parylene deposition over the dispensed liquid. This technique results in a bubble free encapsulation since conformal deposition of the parylene layer is done in vacuum. In the last step, second capacitive electrodes (Cr/Au stack) are deposited using an appropriate shadow mask in an e-beam evaporator. In Figure 2.10-C, the photographs of a completed 100-mm wafer with arrays of actuators show that this wafer-level fabrication technique has high-yield, since almost all devices in the silicon wafer survived.

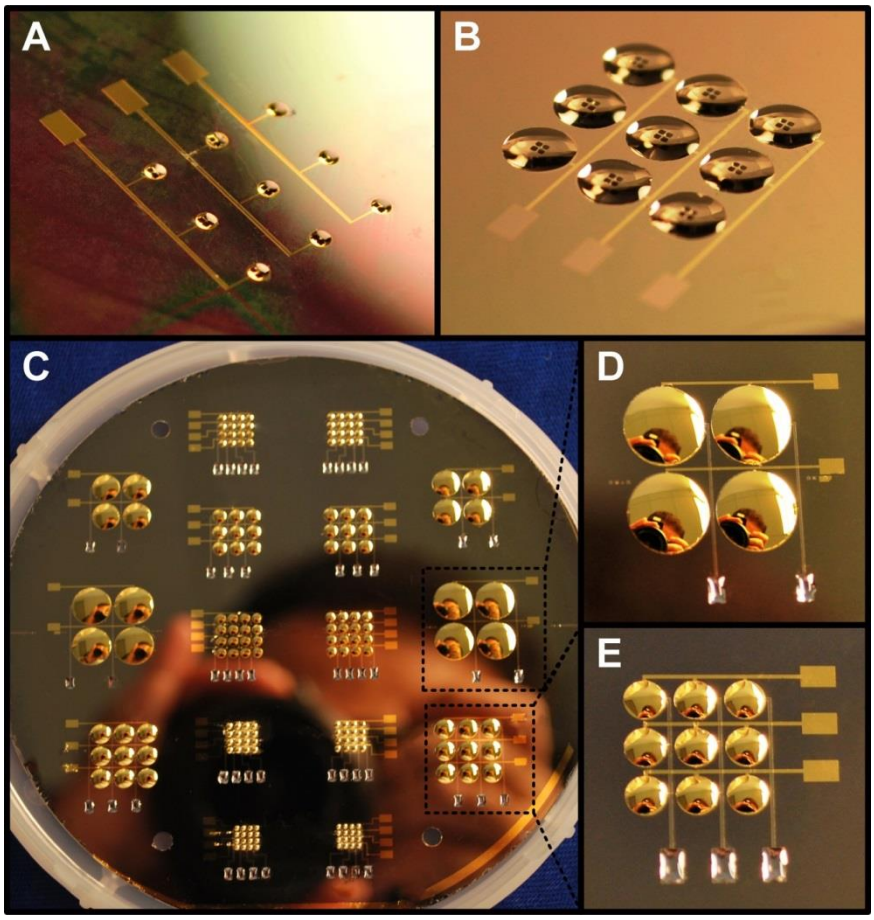

Figure 2.10 Image of front (A) and back sides (B) of the wafer after parylene deposition before the second metal layer is deposited. C: Full wafer view of back side, showing that the fabrication technique can be processed at the wafer level with high yield. D and E show close view of the two different arrays.

2.2.2 Characterization

In this chapter, the EMH structure is used for actuation only. Therefore, it is referred to as Electrostatic Micro-hydraulic Actuators or EMA. First, the device geometry and a process modification that results in curvature correction are investigated. To illustrate the basic operation of EMA, multiple tests are performed. In the first experiment, a DC voltage is applied on the back side and the deflection is measured. A Multi-Physics model in COMSOL™ has been made to compare the experimental data with our theoretical FEM based estimation. Then, the generated force by the EMA structure is measured as the actuation voltage is varied. Due to the limitation of our measurement tools, deflection on the front side could not be directly

measured. Instead, by measurement of the volume displacement under the back side membrane, net volume transfer to the front side is obtained. Based on this volume transfer, deflection on the front side is calculated. Volume change under the membrane can be measured with a 3D laser interferometer or surface profilometer. The devices have also been tested with a Laser Doppler Vibrometer (LDV) to characterize its frequency response and bandwidth.

2.2.2.1 Device Geometry and Curvature Correction

Among all the parameters, the curvature radius of the silicone droplet (i.e. the curvature of one of the capacitance electrodes) is very important since it strongly influences the electrostatic force [34]. In fact, the higher the curvature, the lower the capacitance gap. Therefore, for a curved electrode with low curvature radius, a higher voltage is needed to generate the same force compared to an identically sized electrode with a higher curvature radius. In order to achieve higher curvature radius and thus get higher force at lower applied voltage, a shallow recess on the backside in the locations of the chambers is made (i.e., the first step of the fabrication process). This recess has the same pattern as the Cytop™ creating a step at its edge, and helps to keep the liquid in place. Combined with the hydrophobicity of Cytop™, less liquid oil is needed to cover the chamber areas, which means the oil bubble's height is smaller and the curvature radius is increased. The recess formation is done prior to Cr/Au deposition.

Table 2.1 Dimensions of the fabricated devices along with the measured height of the membranes and calculated curvature radii. (D_f and D_b are the diameters of the front and back side chambers, respectively. $R_{C,b}$ and h_b are the curvature radius and height of the back side membrane)

	D_f [µm]	D_b [µm]	h_b [µm]	$R_{C,b}$ [mm]
Dev 1-1	2000	4472	264	9.59
Dev 1-2	1000	2236	163	3.91
Dev 2-1	2000	4472	62.4	37.7
Dev 2-2	1000	2236	19.0	32.8
Dev 2-3	500	1118	7.04	21.0

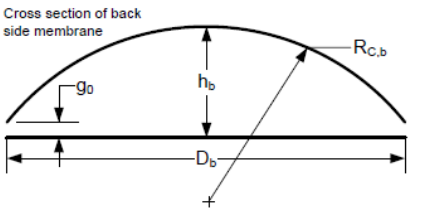

Table 2.1 lists measured dimensions of several fabricated devices. By modifying the process, the curvature radius of the back chamber membrane was increased by almost 9× from the first batch of devices (3.91 mm in Device 1-2) to the second batch (32.8 mm in Device 2-2), for the same membrane radius. This results in a significant improvement in performance of the actuator cells.

2.2.2.2 Deflection vs. Voltage

In this experiment, the back side electrode is actuated and the deflection on the back side is measured with both a profilameter (Dektak) and a laser confocal microscope (LEXT OLS4000). Figure 2.11 shows the back side membrane profile as the actuation voltage is varied from 0 to 200V and Figure 2.12 shows optical images of one of the actuator cells in the array. As it is shown in Figure 2.11, the membrane's deflection is not unidirectional, downward movement around the perimeter and upward movement in the middle is observed. This bidirectional membrane deflection is due to asymmetric sizing of the capacitive electrodes. Since the movable electrode is laid over a curved membrane, it is larger compared to the opposite flat electrode. Once the voltage is applied, the movable membrane is attracted to the flat membrane. In case of pull-in, the movable membrane tends to collapse on the fixed one, but since it has larger surface and cannot shrink in size, it will buckle in the most compliant section to allow other sections to collapse. When there is a marginal deflection, the parts close to the perimeter move downward as they experience larger force due to smaller gap compared to the parts in the middle where the membrane will move upward to avoid shrinkage.

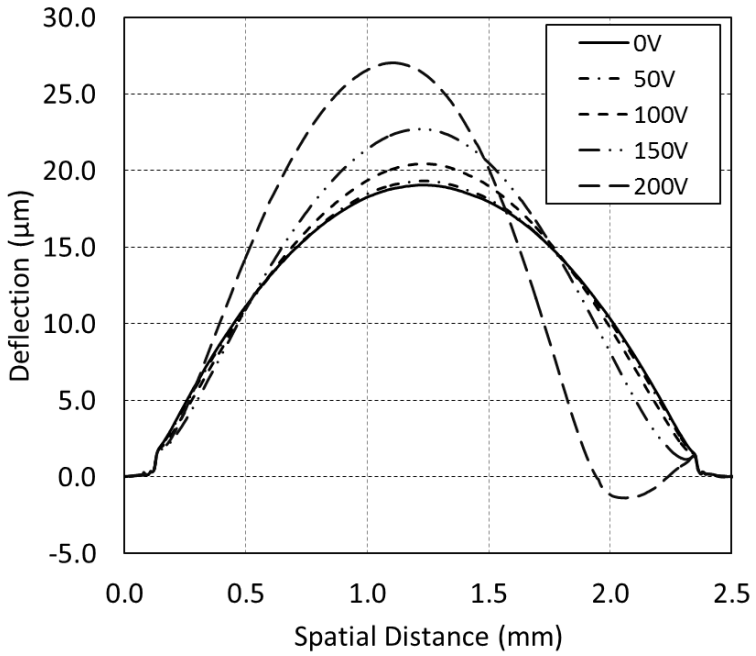

Figure 2.11 Surface profile of one of the cells under various DC bias. The plots show a gradual change in the membrane shape as the voltage increases from 0V to 200V. At 200V, the membrane is partially collapsed and partially bulged up.

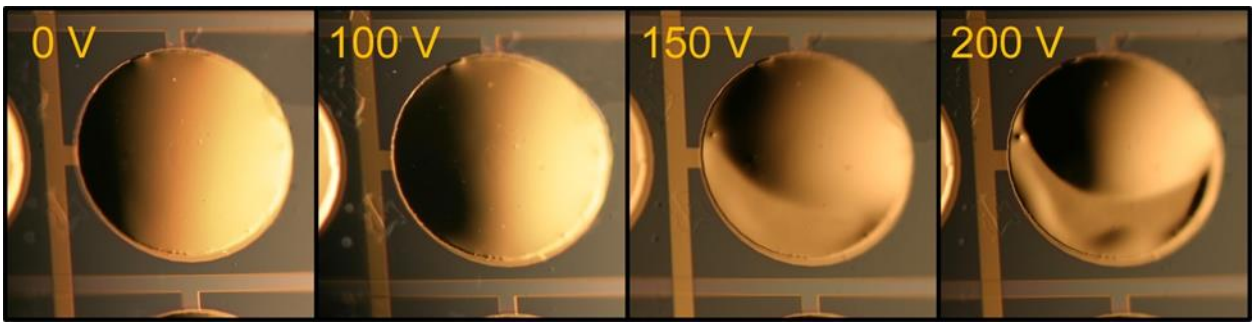

Figure 2.12 Images of one EMA with 2.24mm diameter. The plots show a gradual change in the membrane shape as the voltage increases from 0V to 200V.

The bidirectional movement of the membrane makes it hard to define a hydraulic amplification factor in this case. However, by measurement of the displaced liquid volume underneath the back side membrane and knowing the liquid is incompressible, deflection on the front side can be calculated.

As shown in Figure 2.11, at 200V, back side membrane partially collapses on the electrode underneath. This asymmetry is supposedly due to non-ideal fabrication of the structure that

results in non-uniform capacitive gap around the perimeter. These locations with smaller capacitive gaps have smaller pull-in voltage and will collapse at lower voltages. As a result, the membrane partially collapses; however, the incompressible liquid under the collapsed parts is pushed over to the other side of the membrane that results in the profile shown in Figure 2.11 at 200V.

Figure 2.13 shows the 3D profile of an EMA actuator with back side diameter of 4.47 mm. It should be mentioned that for devices with diameter over 2.5 mm, four separately scanned profiles are stitched together to form the overall profile of the device, as shown in Figure 2.13. This can be one source of error in volume transfer analysis, in the following Section 2.2.2.3.

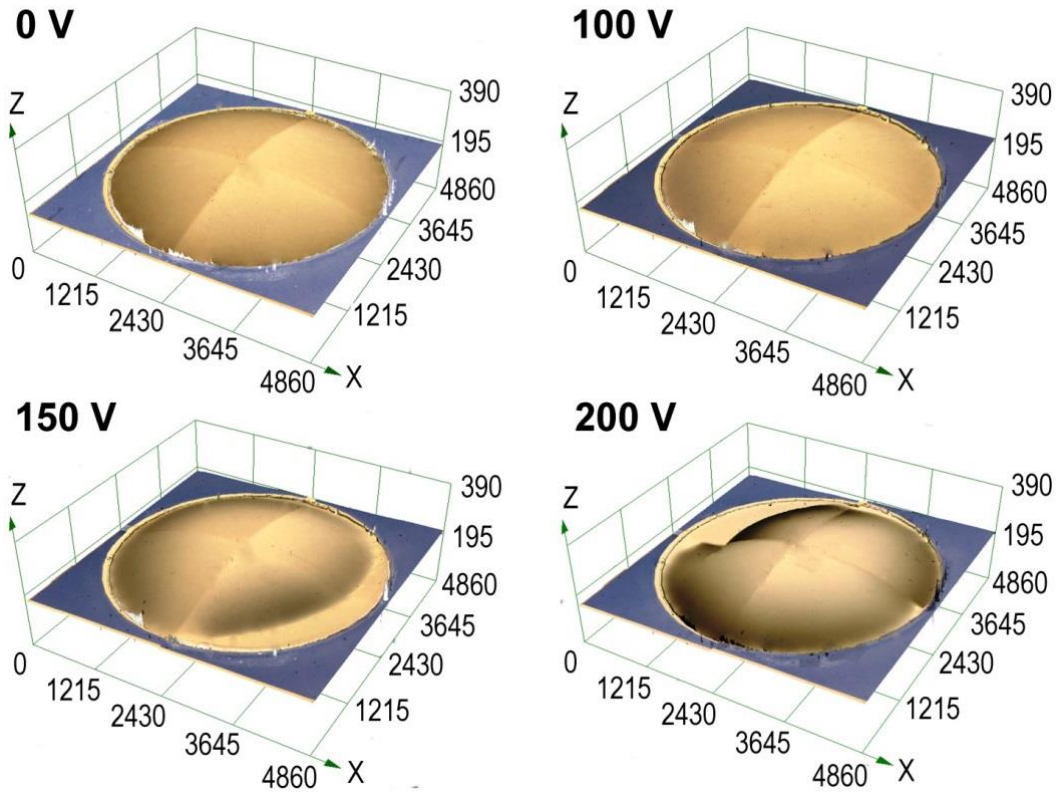

Figure 2.13 3D surface scanning of the micro-hydraulic actuator with a diameter of 4.47 mm at 0V and 200V. Stitching traces can be clearly seen on the membrane.

A 2D Multi-Physics model in COMSOL™ has been developed in which *Electrostatic*, *Structural-mechanic* and *Moving-mesh* components are all coupled to numerically analyze the deflected membrane. The Moving-mesh component is essential in this analysis since the deflection of the membrane is comparable to the gap size. Unfortunately, COMSOL™ does not allow axial symmetry for moving-mesh analysis. Table 2.2 lists the parameters used in the COMSOL™ simulation.

Table 2.2 Device dimension and physical quantities used in the COMSOL™ simulation.

2D simulation	Parameter	Value
Device dimensions	Diameter	2.236 mm
	$R_{Curvature}$	15 mm
	Gap	10 μm (edge)
Parylene characteristics	Thickness	2 μm
	Young's modulus	3.2 GPa
	Poisson ration	0.4
	Dielectric	3.15 ε_0
Liquid (incompressible)	Dielectric	2.9 ε_0

Due to some anomaly in the simulation solver, and the fact that FEM tools are suitable for "buckling type" simulations, it cannot converge for voltages above 21.38V. This value is close to pull-in voltage of the 2D model. The results however, nicely explain the non-uniform deflection of the membrane. It is clear that the potential gradient around the perimeter of the curved electrode, where the maximum force and the maximum deflection is expected, changes abruptly. In Figure 2.14, the original geometry of the curved electrode capacitance along with exaggerated deflection of the membrane at voltages 0-25V are plotted. These plots show that as the voltage increases the membrane bulges up in the middle while collapsing toward the bottom electrode around the edges. Using these deflection results, the simulation tool also calculates total volume displacement under the membrane which proves the proper operation of the system.

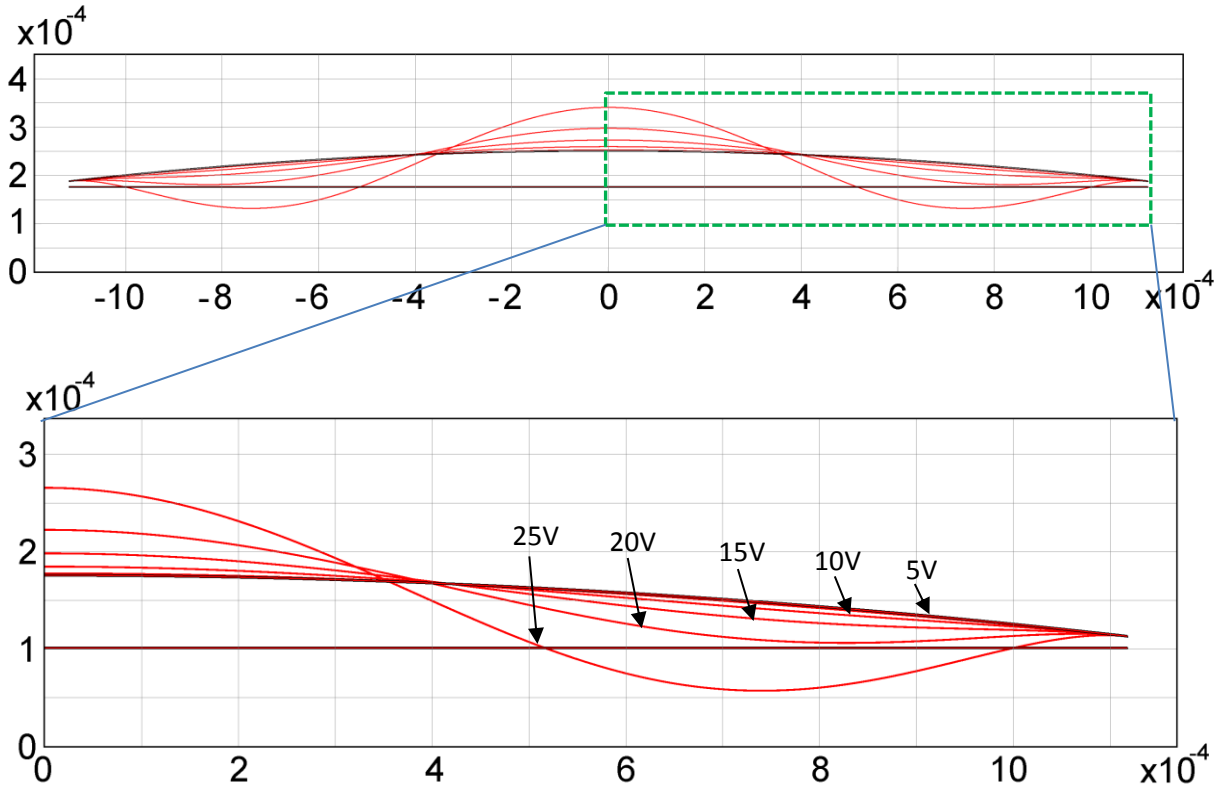

Figure 2.14 Simulation results showing a cross-section of the deflected membrane for actuation voltages 0-25V. Deflections of the membrane are scaled by a factor 20 in all the plots. Maximum positive displacement is 5μm, minimum negative displacement is -7μm. All axis unit is meter.

The total volume transfer and force for 0-20V is given in Table 2.3. Although all the data listed in Table 2.3 is obtained from a 2D simulation, the range of both force and volume change are in fairly good agreement with the deflection measurement and volume transfer analysis discussed in the next subsection. This simulation confirms the same bidirectional deflection of the membrane observed from experimental results shown in Figure 2.11. Note that for voltages below 150V, the trend is the same as what simulation results suggest, however, after 150V, parylene membrane partially collapses, which is believed to be due to imperfection in fabrication.

Table 2.3 Simulation results of directional volume displacement and force.

Actuation Voltage	+y-direction ΔV	Force
5 V	-1.367×10^{-17} m^3	1.397×10^{-5}
10 V	-1.291×10^{-16} m^3	6.117×10^{-5}
15 V	-7.780×10^{-16} m^3	1.650×10^{-4}
20 V	-5.130×10^{-15} m^3	4.375×10^{-4}

2.2.2.3 Volume Transfer

Due to bidirectional deflection of the membrane, the net volume displacement under the back side membrane has been measured to evaluate functionality of the EMA. In other words, negative net volume change under the back side membrane implies that the back side chamber is contracted and the change in its volume is transferred to the front side chamber. Two techniques have been utilized to measure this volume transfer. First, the surface profile cross section of the membrane across diameter is measured and with axial symmetry assumption, the volume under the measured profile (i.e. a curve) is obtained by numerical integration. If the membrane partially collapses (such as the case shown in Figure 2.11 at 200V), the total chamber's volume is estimated by a positive volume under a bell-like surface on right and a negative semi-toroid shape on left. In the second method, the volume under the membrane and above the substrate plane is directly measured based on the 3D profile of the membrane obtained by LEXT OLS4000 interferometer. It should be noted that both described methods could incorporate error in the measurements. In the former, the axial symmetry assumption and 3D shape approximation, and in the latter, measurement noise caused by imperfect reflection of the laser beam from the surface can result in the error.

Table 2.4 lists the obtained volume displacement for devices with various sizes and the resultant front side deflection based on calculation at 200 V. Additionally, if the deflection of the front side membrane is known, the pressure, therefore the force applied to the front side

membrane causing this deflection, can be calculated. To calculate the pressure and force, plate theory relations for thin circular membranes with presence of residual stress is used [36]. The residual stress in the calculations is assumed to be 30 MPa, compressive [37].

Table 2.4 Volume change measurements with LEXT interferometer and resultant calculated front side deflection, liquid pressure and generated force at 200V.

	D mm	**ΔV μm^3**	**ΔL_{front} μm**	**ΔP kPa**	**ΔF mN**
Device 1	4.47	6.79×10^7	43.2	3.64	11.4
Device 2	4.47	1.48×10^7	94.3	12.3	38.6
Device 3	2.24	1.31×10^7	33.4	13.5	10.6

2.2.2.4 Force vs. Voltage

In Section 2.2.2.3, the pressure and force characterization of the EMA based on surface analysis and volumetric transfer of liquid calculations are reported. In this section, a method for direct measurement of the force and pressure for the fabricated EMA structures is described. Using a very sensitive μ-gram-range scale in the set-up schematically shown in Figure 2.15 inset, the force generated by EMA can be directly measured. As shown in this figure, a moderately soft rubber tip is placed over the scale's plate, to probe each of the small hydraulic cells. With a 1 mm^2 tip area, however, devices smaller than 2 mm in diameter could not be tested. The EMA chip is secured to a manually controlled XYZ stage. The stage height is lowered until the tip touches the membrane, then, the pressure is increased by further lowering of the stage to set the initial contact force, which is measured by the scale. Next, the actuation voltage is applied and the force generated by EMA is directly measured. Figure 2.15 shows force vs. voltage curve for 0.1 mN and 0.5 mN initial contact forces. As the voltage increases the membrane moves, exerting a force downward on the rubber tip, which is measured by the scale. The force monotonically increases with the voltage. From experimental results plotted in Figure 2.11, it is noted that no significant deflection is observed below 100 V. Therefore, membrane deflection

below 100 V is very small, thus no data point is measured below this actuation voltage. The difference in the plots may originate from a change in the effective contact area between actuator's membrane and the tip. The higher initial contact force increases the contact area as the curved membrane is pushed against the tip, resulting in a more realistic measurement. The variance in the measurement is about 25%. However, if the effective contact area had quantified, the accuracy of the measurements would have been significantly improved.

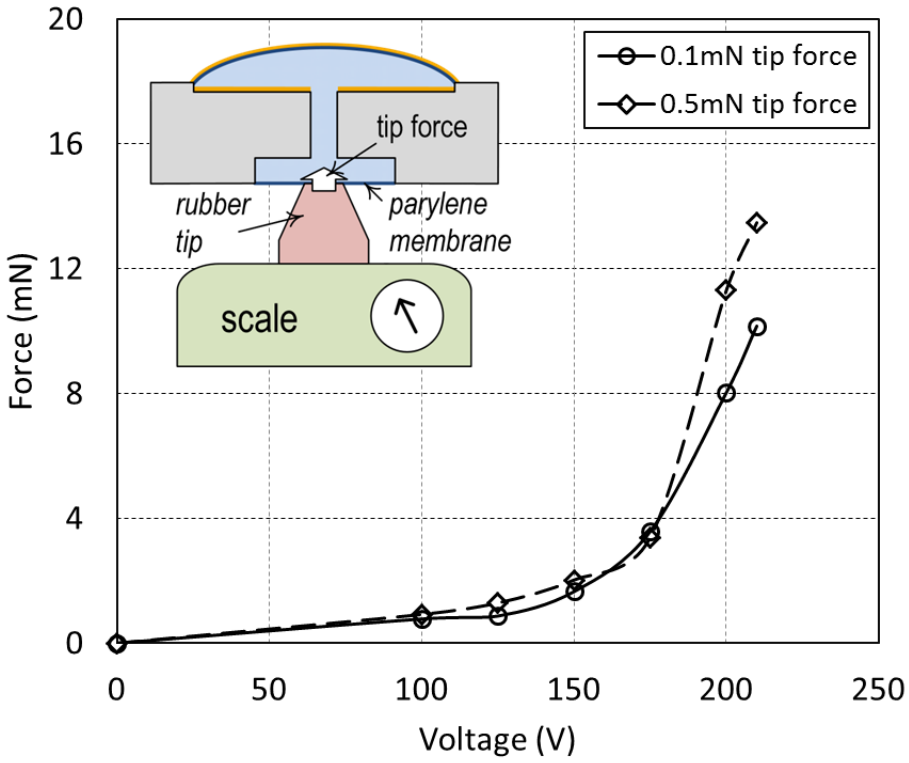

Figure 2.15 Direct force measurement for the cell with 4472µm diameter of the backside membrane at 0.1 and 0.5 mN of initial tip contact force. Inset image schematically shows how the rubber tip touches the actuator.

Table 2.5 lists the measurement results in comparison with previous calculations of force using varying gap capacitance actuation theory and volumetric liquid transfer analysis based on the measurement of the surface profile. In the volumetric analysis, the deflection is calculated by using the amount of displaced volume. Given the deflection, the pressure and force on the

membrane can be obtained through plate theory as described in Section 2.2.2.3. At lower actuation voltages (+100 and +150 V), differences in predicted and measured forces may be due to further changes in the effective contact area of the tip with the membrane. In addition, due to large shape deformation of the actuator's curved electrode in voltages greater than 150 V, the force predicted by the theoretical model is different from that of measurements by a factor two.

Table 2.5 Comparison between direct force measurements, Analysis based on surface profile measurements and theoretical calculation of forced generated by a curved electrode capacitance.

Actuator with 4.47 mm diameter backside chamber	**F (mN) 100 V**	**F (mN) 150 V**	**F (mN) 200 V**
Theory (gen. Force by capacitance)	5.819	13.09	23.28
Analysis (volumetric transfer)	5.23	7.41	8.83
Measurement 1 (0.1 mN tip force)	0.776	1.65	8.028
Measurement 2 (0.5 mN tip force)	0.619	2.024	11.30

2.2.2.5 Power Consumption

EMA uses capacitive actuation, therefore consumes less power compared to thermal or piezoelectric actuators. The total capacitance of the EMAs ranges from about 120 pF to 1 nF for cells with back side diameter of 1.5 mm to 6 mm. This value includes parasitic capacitances and capacitances by running long metal traces over parylene layer on top of silicon wafer for interconnections. Knowing the maximum applied voltage is 200V, the power consumption for EMA cells ranges from 2.4 μW to 20 μW per cycle, depending on the size. This level of power consumption is considerably less than piezoelectric actuators (with approximately the same size) that operate in mW range [38].

2.2.2.6 Frequency Response

In order to obtain the frequency response of the devices, the Polytec MSA-500 Laser Doppler Vibrometer (LDV) has been used. In this test, the back side membrane is electrostatically actuated and the speed of its deflection is measured as the actuation frequency is swept by a

chirp signal from 0 to 100Hz. Figure 2.16 shows the response of an EMA with back side diameter of 4.47mm. According to this measurement, the bandwidth of this device is about 5Hz based on full width at half-maximum (FWHM) measure. In the spectrum shown in this figure, a resonant frequency of about 2Hz can be observed. Additionally, there are a couple of high deflection peaks in the 15-25Hz band.

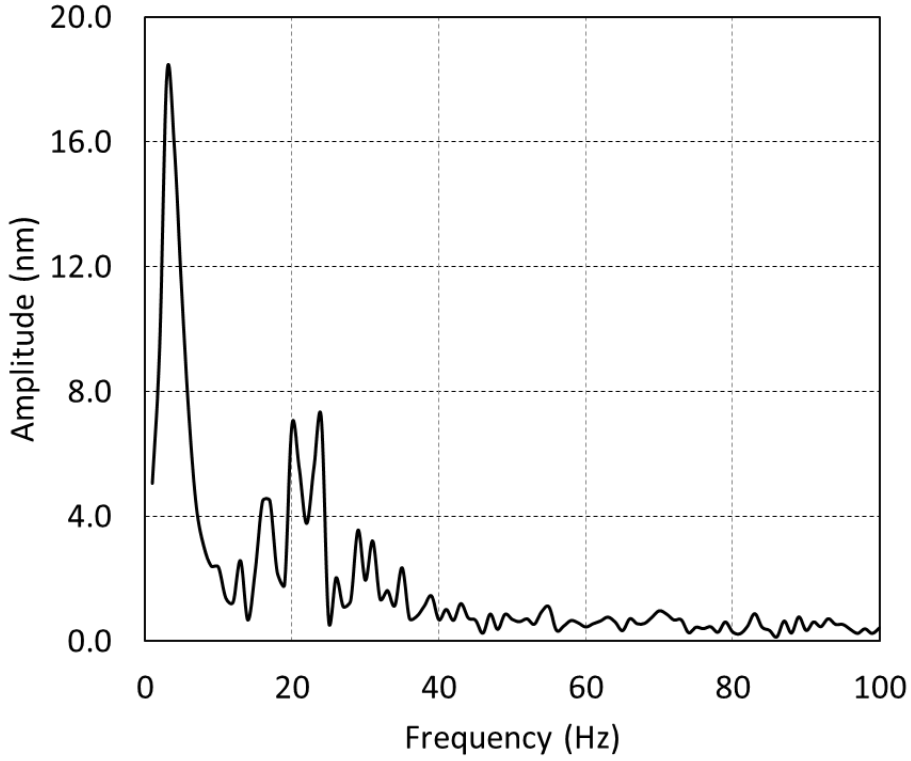

Figure 2.16 Frequency response measurement with Polytec MSA500 LDV.

2.2.3 Discussion

The EMA structure introduced in this chapter is a reliable paradigm in applications where high force or large out of plane deflection is required. EMAs with back side diameter of 4.47mm showed maximum out of plane deflection of slightly less than 100 μm. The maximum force generated with an EMA with back side diameter of 4.47mm is measured to be about 38 mN. The generated force and deflection together are large enough that can fully deflect a PDMS valve

structure in a micro-fluidic system. This exhibits the efficacy of EMA for fluid manipulation in lab-on-a-chip systems.

The EMH structures are robust in sensing or actuation units since the capacitive gaps are enclosed. Aging is not a noticeable issue in the EMA devices due to use of a stable and inert low vapor-pressure fluid. These devices have shown almost the same performance after over three years of fabrication in that they could be operated in sensing and actuation mode without noticeable change of performance. Fatigue of parylene membrane will not be problematic since the maximum pressure applied on the membrane is well below its yield strength. Additionally, almost all processing steps are performed at low temperature, namely at room temperature. The low temperature fabrication process substantially alleviates intrinsic and residual stress. The deposition of parylene on liquid also results in low stress parylene film since first, the deposition temperature hardly exceeds 60°C and second, the liquid substrate provide the compliance needed during deposition to further reduce stress [39]. It is shown that deposition of parylene on silicone results in thin films with a very low tensile stress of about 1 MPa [40].

EMA structures can also be used in parallel configuration to further amplify deflection in that a common front side chamber is connected to multiple back side chambers. In this fashion, as the back side membranes are electrostatically actuated, displaced liquid from multiple chambers is accumulated and pushed into the single front side chamber, deflecting its membrane. This architecture can also be used to form a micro-scale out-of-plane digital actuator; one by one actuation of the back side membranes causes step-wise accumulation of the fluid into the front side chamber, and therefore its step-wise membrane movement.

Utilizing the introduced EMH structure in sensing mode can maintain high sensitivity over large range and parallel exploitation of EMH structures in sensing mode can further amplify

sensitivity. In sensing mode, parallelization of multiple front side chambers that are connected to a single back side chamber can multiply the effect of measurand on the back side capacitive sensor, therefore increase sensitivity. For instance, if two front side chambers are parallel to a single back side chamber, a constant pressure on the front side causes twice the capacitance change on the back side, compared to that of a single front side chamber.

Electrostatic force amplification can be further enhanced by addition of nano-particles suspended in the silicone oil that have an electrical dipole. The introduced dipoles can significantly increase equivalent permittivity of the oil; therefore amplifying electrostatic force generation [41]. Additionally, other low vapor pressure materials with lower viscosity can be utilized to increase the bandwidth of the EMA devices. The silicone oil used for fabrication of second generation EMA has dynamic viscosity of 175 cP. Krytox® [42] and Fomblin® [43] with viscosities of about 60 cP can be utilized for fabrication of EMAs.

2.3 Conclusion

For the first time, the concept of integrated electrostatic actuation with micro-hydraulic structure is exhibited in EMH structures. Integration of electrostatic elements with micro-hydraulics is beneficial in two ways: 1) electrostatic force amplification due to high permittivity dielectric material, and 2) mechanical amplification through micro-hydraulic structure. Experimental results show the advantage of the EMAs that can be considered as a new design paradigm in MEMS devices, where high force and/or large deflection are required. Integration of electrostatic components enables this structure to be used in sensing mode as well, in which sensitivity is decoupled from full-scale range. This separation allows for highly sensitive devices with large dynamic range. High performance hair-like airflow sensors and force (tactile) sensors based on EMH structures will be discussed in Chapters 4 and 5.

3 Chapter 3: Electrostatic Micro-Hydraulic Optimization

3.1 Introduction

In Chapter 2, the basic EMH structure is introduced and its operation in actuation mode (EMA) is studied. Although fabrication of the first generation of EMH structure was mainly conducted as a feasibility study, it producedhigh performance devices in most aspects except response time. In this chapter, a thorough analysis of the first generation EMH system is reported. This study shows the slow response time is mainly due to large fluidic resistance of the channels and high viscosity of the fluid used. By developing a FEA model using COMSOL™, a more optimally-designed EMH architecture is introduced, fabricated and characterized.

3.2 Modeling, Simulation and Design

It is hypothesized that in EMH devices introduced in Chapter 2, the dominant slow response time arises from viscous fluid flow. To verify this, a 2-D multi-physics model in COMSOL™ 3.5 is developed (Figure 3.1) that uses three linked modules: structural mechanics *(Plain Strain), Moving Mesh* and fluidics *(Incompressible Navier-Stokes). Moving mesh* is used since a large deflection of the top parylene membrane is observed[1]. In order to simulate the response time of the micro-hydraulic system, a step pressure is applied on the back side membrane and the deflection in the center of the front side membrane is monitored to measure the "settling time" needed for the system to reach steady state. The tool calculates the transient response of the front side membrane. The lower the fluid viscosity, the faster the device will be.

[1] Newer versions of COMSOL™ (4.0a and above) have a built in FSI (Fluid Solid Interaction) module that can be used for this type of simulations, which are more time and resource efficient. However, most of the results presented in this chapter are provided before arrival of latest COMSOL™ versions.

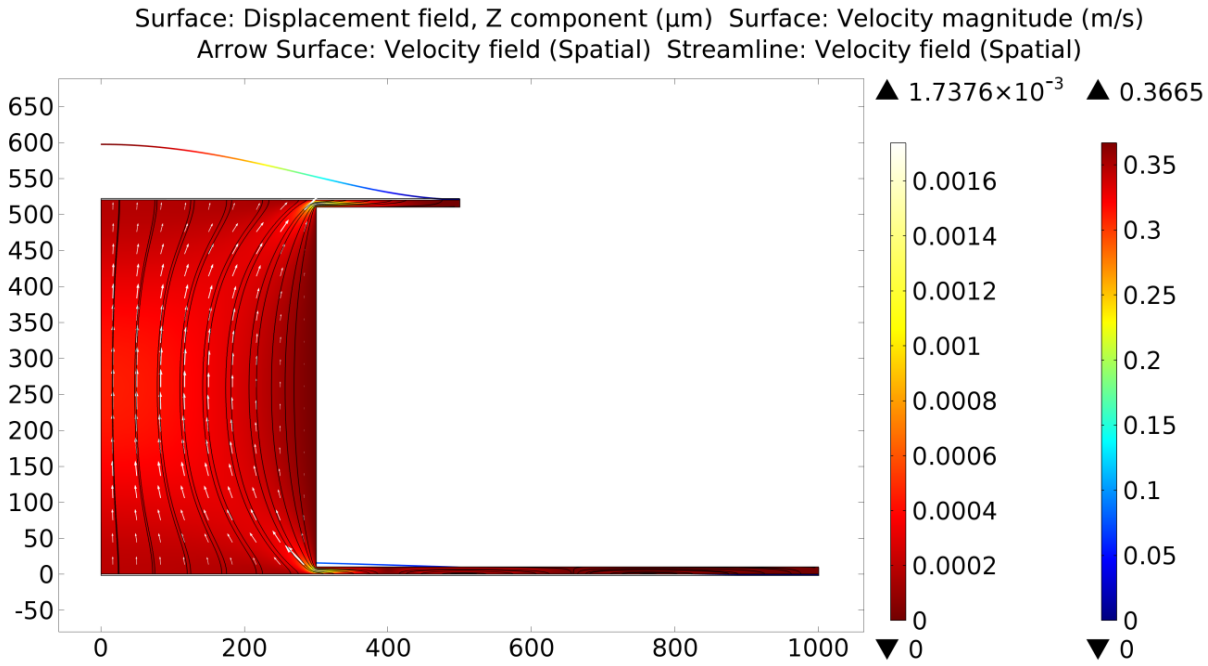

Figure 3.1 Snapshot of COMSOL™ simulation, showing displacement of the membranes, velocity field streamlines, direction and magnitude at 1 msec.

Figure 3.1 is a snapshot of the right half of an EMH structure cross section, in a 2D COMSOL™ simulation. It shows geometry of the device, deflection of the front side parylene membrane, flow streamlines and flow velocity field.

After the model is developed in COMSOL™, three different fluids, including silicone oil, water and air are used. In this simulation, air is considered to be incompressible. In the model, the depth of the front side chamber is 10 µm and that of the back side is 5 µm. The parylene membrane thickness is 1 µm. The simulation results are plotted in Figure 3.2. For a 200-µm wide channel, silicone oil with dynamic viscosity of 175 cP has a settling time of about 20 seconds. The settling time for water (1 cP) is dramatically reduced to 200 msec and the same trend is observed for air (0.0178 cP) with settling time of about 2 msec. Parameters used for these simulations are listed in Table 3.1.

Table 3.1 Parameters used for simulation of straight-wall micro-hydraulic device.

Fluid Dynamic Viscosity at 25˚C	Silicone oil	175 cP
	Water	1 cP
	Air	0.0178 cP
Device Geometry	Front side chamber depth	10 μm
	Back side chamber depth	5 μm
	Parylene membrane thickness	1 μm
	Channel width	200 μm
	Front side membrane width	1 mm
	Back side membrane width	2 mm

This shows that the simple model of fluid resistance, relating resistance directly to viscosity, is valid for this structure (Eq. 3.1) and Poiseuille flow [39] is the dominant component in this system, which means the flow inside the channel connecting the front and back side chambers is similar to a pipe flow. Fluidic resistance of a channel (R_f) based on Poiseuille flow is:

$$R_f = \frac{128\,\mu L,}{\pi D^4} \qquad \textit{Eq. 3.1}$$

In which L is the channel length, μ is dynamic viscosity of the fluid and D is the hydraulic diameter of the channel [39].

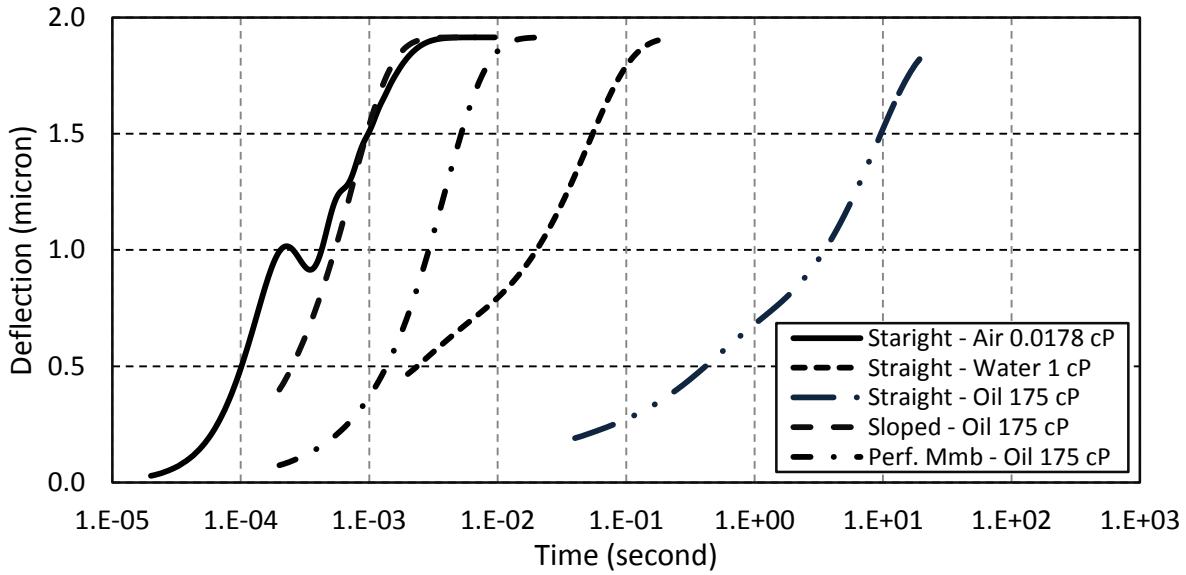

Figure 3.2 Simulation results comparing step response of fluids with various viscosities using straight-wall geometry, and comparing silicone oil response for three architectures: straight-wall, sloped-wall, and sloped-wall with perforated membrane.

3.2.1 Electrical Circuit Analogy

A hydraulic system can be modeled with an equivalent electrical circuit. Electrical analogous parameters for pressure and flow are voltage and current, respectively. A resistance in the equivalent electrical circuit models any element/structure in a hydraulic system that causes pressure drop. A fluid capacitor is an element whose volume changes with respect to pressure, or can store potential energy. Inertance, similar to inductance, is an element that stores kinetic energy, for instance, momentum or kinetic energy of a pipe can be modeled by an inertance. Table 3.2 lists the analogy between a fluidic system and an electrical circuit.

Table 3.2 The hydraulic system analogy with electrical circuit elements, adopted from [44].

Variable or Equation	Description	Units	Electrical Analogy
$\boldsymbol{q}$ (flow)	A *through* variable, what goes in comes out (except for a capacitor).	m^3/s	$\boldsymbol{i}$ (current)
$\boldsymbol{p}$ (pressure)	An *across* variable, defined as the difference of this quantity across the element.	$Pa = N/m^2$	$\boldsymbol{v}$ (voltage)
$p = q\boldsymbol{R}$	Resistance, due to pipe or constriction. It is often nonlinear.	$R = p/q = Pa/(m^3/s)$ $Pa{\cdot}s/m^3 = Ns/m5$	$v = i\boldsymbol{R}$
$q^2\boldsymbol{R} = p^2/\boldsymbol{R}$	Dissipation	W	$i^2\boldsymbol{R} = v^2/\boldsymbol{R}$
$p = \boldsymbol{I}\, dq/dt$	Inertance. Momentum and kinetic energy of water in pipe.	$Pa/(m^3/s^2) = Pa{\cdot}s^2/m^3$ $kg/m^4 = Ns^2/m^5$	$v = \boldsymbol{L}\, di/dt$
$E = \frac{1}{2}\boldsymbol{I}q^2$	Energy	J	$E = \frac{1}{2}\boldsymbol{L}i^2$
$P(s) = Q(s)\boldsymbol{Is}$	Impedance	$Pa{\cdot}s/m^3 = Ns/m^5$	$V(s)=I(s)\boldsymbol{Ls}$
$q = \boldsymbol{C}\, dp/dt$	Fluid capacitor, such as a tank or pressure chamber.	$(m^3/s)/(Pa/s) = m^3/Pa$ $= m^5/N$	$i = \boldsymbol{C}\, dv/dt$
$E = \frac{1}{2}\boldsymbol{C}\, p^2$	Energy	J	$E = \frac{1}{2}\boldsymbol{C}v^2$
$P(s) = Q(s)\boldsymbol{1/Cs}$	Impedance	$Pa{\cdot}s/m^3 = Ns/m^5$	$V(s) = I(s)\boldsymbol{1/Cs}$

Due to the specific geometry of the EMH, closed-form solution for some of the lumped equivalent electrical elements cannot be obtained. However, use of a qualitative equivalent circuit is beneficial for better understanding of the optimization process in the succeeding sections.

The equivalent electrical circuit for the micro-hydraulic structure shown in Figure 3.1 can be formed by identifying parts contributing to pressure drops, change in volume as a result of pressure change, and delivery of kinetic energy. Based on streamlines shown in Figure 3.1, the liquid moves laterally in the bottom chamber toward the channel, enters the channel and again moves laterally to reach the corners of the front side chamber. Therefore, three fluidic paths from the bottom to the top exist, and each will have a resistance associated with it. Additionally, there are two orifices in the structure, as the liquid moves from the bottom chamber to the channel, the sharp corner causes pressure drop, which is equivalent to added resistance. Similarly, when the fluid enters the top channel, the pressure drops again, moving past the sharp corner. Parylene membranes operate as fluidic capacitors, in other words the volume under each membrane changes when pressurized. Finally, any inertial movement of the liquid has an associated kinetic energy; therefore, three inertances for both chambers and the through-wafer channel should be considered. The equivalent electrical circuit model is shown in

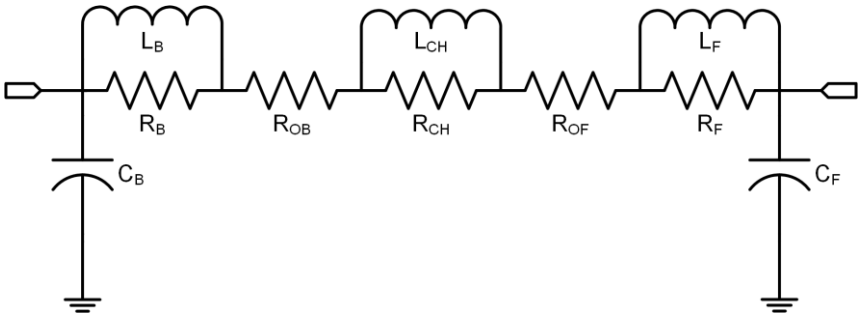

Figure 3.3 The straight-wall EMH equivalent electrical circuit model. R_F and R_B are front and back side chamber resistances, R_{CH} is the channel resistance, C_F and C_B are front and back side parylene membrane capacitances. L_F and L_B are inertance due to fluid flow in front and back sides chambers and L_{CH} is the channel inertance. R_{OF} and R_{OB} represent the orifices on the front and back sides.

3.2.2 Straight-Walls vs. Sloped-Walls

To improve the response time of the EMH structure shown in Figure 3.1, the fluidic resistance (R_B, R_{OB}, R_{CH}, R_{OF} and R_F) between front side and back side chambers should be

minimized. The geometry of this "straight-wall" channel EMH structure can be modified so that the overall fluidic resistance is lowered. R_{CH} can be modeled by R_f of a Poiseuille flow, given in Eq. 3.1. Based on this equation, the best way to reduce the resistance in the system is to modify the channel width, as the fluidic resistance is inversely proportional to the channel width to the fourth power. Therefore, the channel should be widened as much as possible. In addition, in order to remove any additional resistance caused by the narrow gap between either the front side or back side membrane and the recesses (R_F, R_B), and compensate for pressure drop due to orifices (R_{OB} and R_{OF}), the recess and silicon underneath are eliminated. This new design geometry is referred to as "sloped-wall" channel (Figure 3.4). Once the chambers are essentially eliminated in the sloped-wall geometry, the associated inertances are eliminated as well, however, the channel resistance and inertance change to R'_{CH} and L'_{CH} as shown in Figure 3.5-left. In going from the straight-wall to the ideal sloped-wall geometry (without perforated Si electrode), the larger effective channel diameter causes a > 6,000× reduction in the response time of the micro-hydraulic device with silicone oil, from 20 sec to 3 msec as depicted in Figure 3.2.

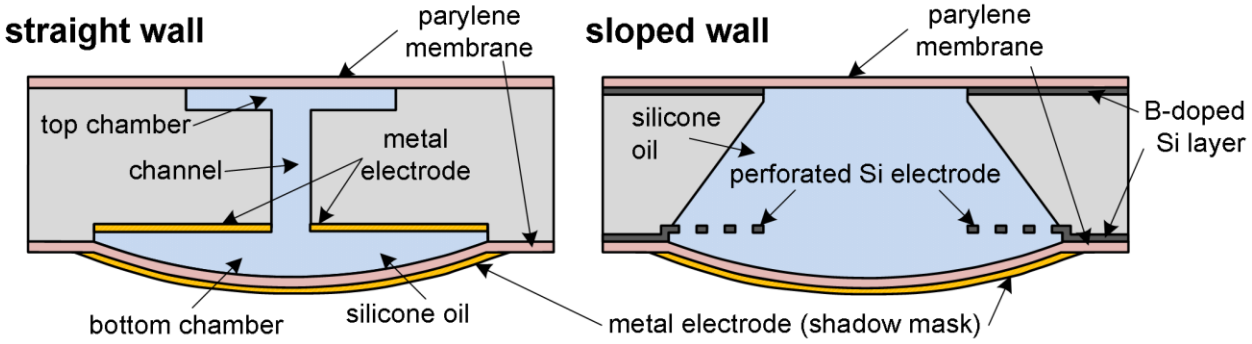

Figure 3.4 Schematic cross section view of straight- and sloped-wall EMH structures.

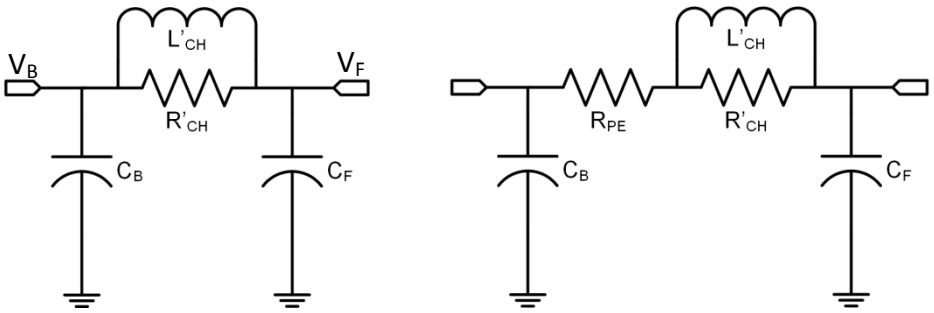

Figure 3.5 Sloped-wall EMH equivalent circuit models, with (right) and without (left) perforated electrode.

In the straight-wall architecture, electrostatic sense/actuation of the backside membrane was achieved using a metal electrode on the Si recess (Figure 3.4) and a second metal film on the flexible parylene membrane. However, the sloped-wall design does not provide a location for this electrode as the silicon bulk is removed to improve the speed of the device. Therefore, a suspended perforated electrode as shown in Figure 3.4 is added. The perforated electrode adds a small resistance to the fluidic path (R_{PE} as shown in Figure 3.5-right); therefore, it slightly increases the predicted response time from 3msec (with no membrane) to 20msec, as shown in Figure 3.2. Nonetheless, the overall improvement in response time with the re-designed architecture is still 1000× better. The perforated membrane has a large center opening with a diameter the same as the channel width in the straight-wall architecture. For the simulations in Figure 3.2, the perforated section of this membrane consists of 20 μm wide, 10 μm thick silicon blocks with spacing of 20 μm. Figure 3.6 is a snapshot of simulation results of water in the sloped-wall EMH with perforated membrane at 0.9 msec. In this simulation, the front side parylene membrane fluctuates before settling at 0.9 msec, causing the downward fluid movement, therefore, vortices that can be seen on the right corner of the channel.

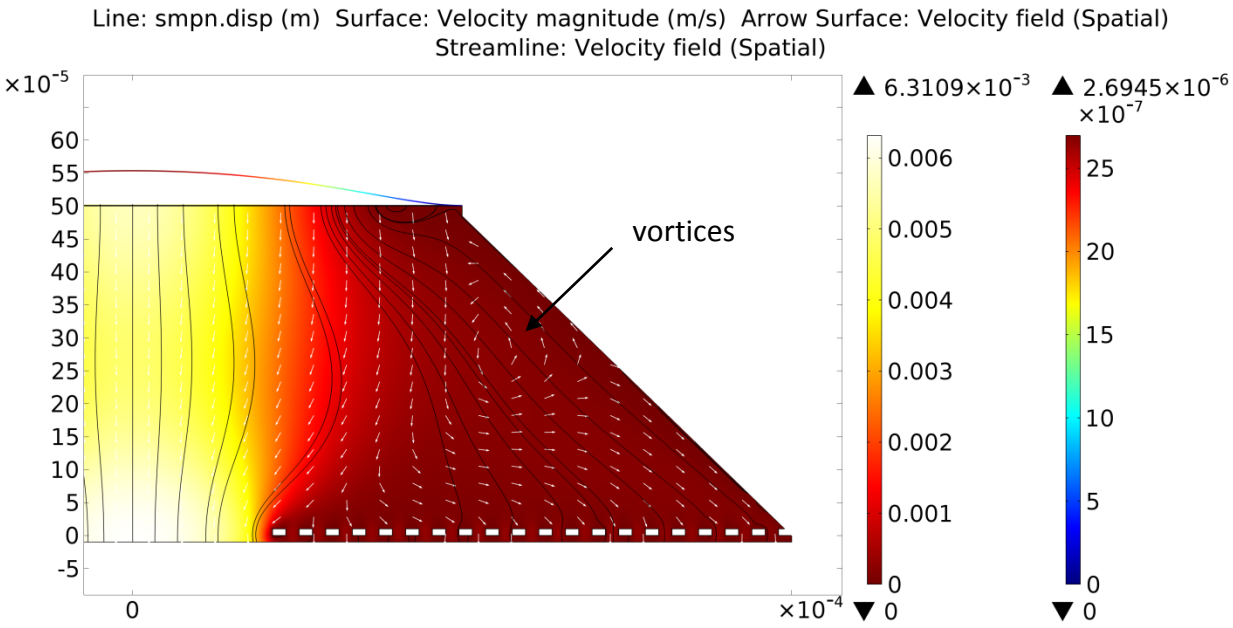

Figure 3.6 Snapshot of COMSOL simulation of sloped-wall structure with perforated membrane, showing displacement of the membranes, velocity field streamlines, direction and magnitude at 0.9 msec.

3.2.3 Sensing Mode vs. Actuation Mode

In all the simulations so far, a constant pressure is applied to the back side (large) membrane and the front side (small) transient response is monitored. This mode of operation is similar to the EMA actuation mode, except the electrostatic force is replaced by a uniformly distributed force on the back side. However, the EMH can be operated in the sensing mode, in that the front side membrane is pressurized and back side deflection is sensed electrostatically. The concept of the EMH structure being used in both sensing and actuation modes is shown in Figure 3.7.

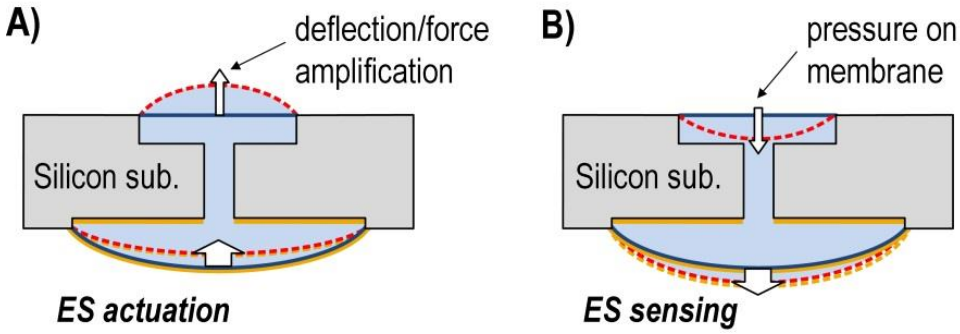

Figure 3.7 Electrostatic micro-hydraulic structure for sensing and actuation.

The response time of the EMH structure in sensing and actuation modes are not necessarily the same. In sensing mode, the elasticity of the back side membrane contributes to response time, whereas in actuation mode, that of front side determines the response time. Using the equivalent electrical circuit helps to address this behavior. The transfer function between nodes A and B is not the same as transfer function between B and A. For example, in the circuit shown in Figure 3.5-left, it is assumed that the transfer function between nodes B and F is defined as their voltage ratio and the overall channel impedance is represented by Z_{CH}. Therefore, the F-B transfer function is: $\frac{V_F}{V_B} = \frac{1}{1+Z_{CH}C_F s}$, while the B-F transfer function is given by: $\frac{V_B}{V_F} = \frac{1}{1+Z_{CH}C_B s}$. From this example it is clear that the time constant of these two transfer functions are not the same. Therefore, for time response optimization, the EMH is assumed in sensing mode as it will be used for realization of hair-like air flow and tactile sensors.

3.2.4 Perforated Membrane Optimization

Based on simulation results depicted in Figure 3.2, the perforation size and pattern must be chosen to co-optimize rise-time (which favors no membrane) and capacitance (which favors a solid membrane). The co-optimization becomes more complicated as one of the electrode plates of this capacitance is curved. In this section, the effect of perforation pattern and size on the curved electrode capacitance is studied. Using the results of capacitance modeling, various perforation patterns and sizes are tested to minimize the response time of the EMH system.

3.2.4.1 Capacitance Modeling

The figure in Table 3.3 shows the geometry of the curved electrode capacitance. It is intended to learn how the capacitance changes as the flat bottom electrode plate is reduced in size and perforation pattern altered. To obtain the flat electrode size effect, the curved electrode capacitance is modeled in COMSOL™. Using electrostatic module with 2D axial-symmetry, the

center opening size is varied and total capacitance is measured. It is assumed that the electrodes are inside a dielectric box with relative permittivity of 1. One electrode is grounded and 1V is applied to the other one. Continuity boundary condition is assumed for outer edges of the dielectric box containing the capacitor and axial symmetry condition for the symmetry axis. Details of the structure geometry and parameters used in this simulation are listed in Table 3.3.

Table 3.3 Geometry of curved electrode capacitance and definition of perforated membrane parameters used for COMSOL™ simulations.

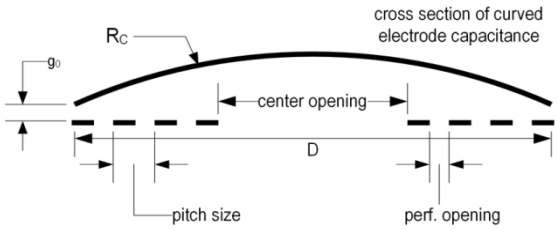

Top Electrode	R_C	30 mm
	Thickness	1 μm
	g_0	10 μm
Bottom Electrode	D	4 mm
	Center opening	20 – 100%
	Pitch size	80 μm
	Perforation opening	0 – 94%
	Electrode thickness	15 μm

Figure 3.8 and Figure 3.9 depict snapshots of the simulation results, showing both electric field and potential. As can be seen in this figure, electric field density around the perimeter is higher compared to the center. To calculate the capacitance, charge density is integrated over the surface and divided by applied voltage, in this case 1V. Therefore, the charge density integral is the total capacitance in Farad.

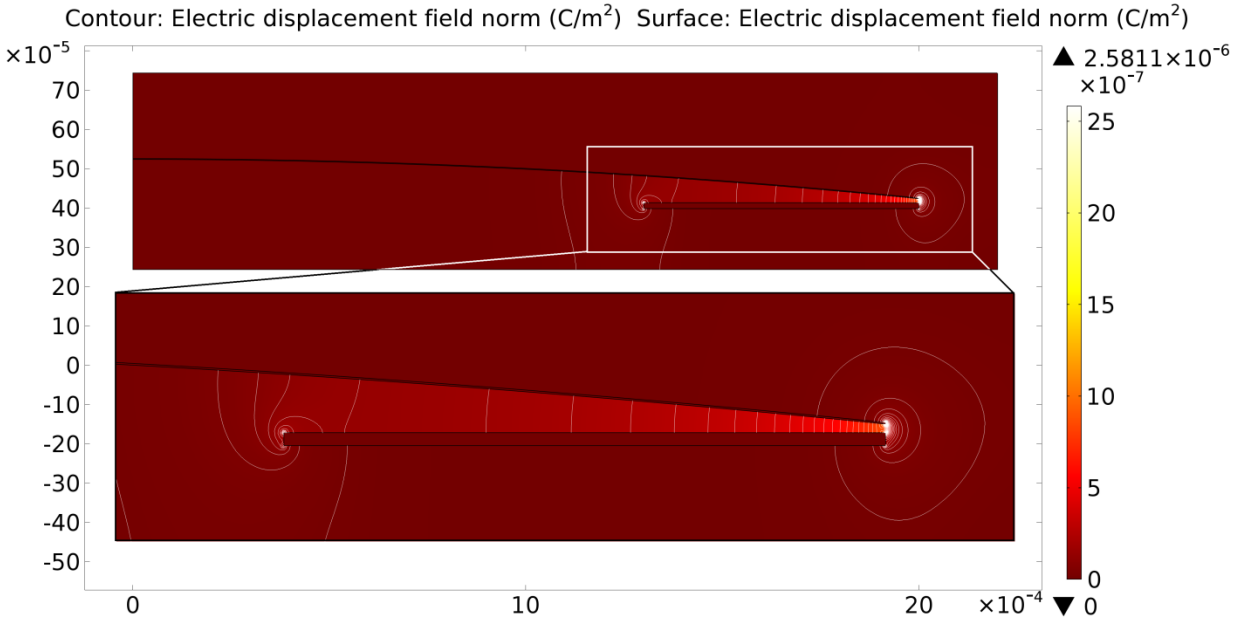

Figure 3.8 Snapshot of COMSOL™ 2-D axial symmetry simulation of center opening size effect on capacitance, showing electric displacement field (equal to charge density) and electric field contours.

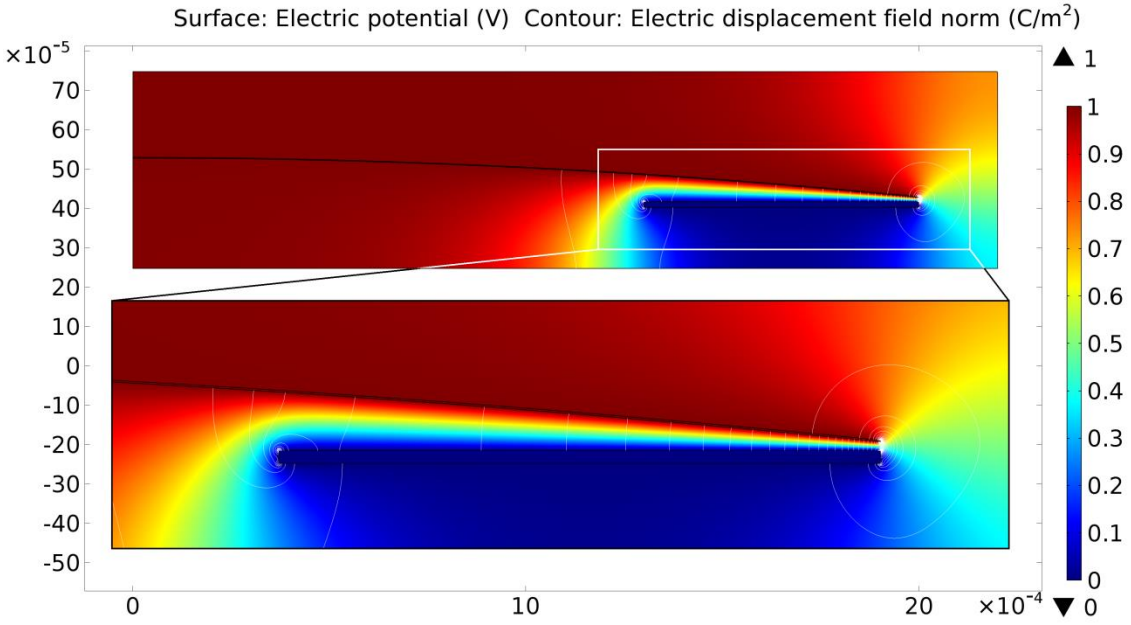

Figure 3.9 Snapshot of COMSOL™ simulation, showing electric potential and electric field contours.

Figure 3.10 shows simulated capacitance vs. center opening size, stated as a fraction of the membrane diameter. A capacitance change of ~ 100 pF/m occurs when the opening widens from 0 to 40%, and when the opening changes from 95% to 100% of the diameter. This illustrates

that, due to the curvature of the electrode on the parylene membrane, the perimeter of the capacitor disproportionately contributes to total capacitance. Therefore, a large center hole can be added to aid fluid flow.

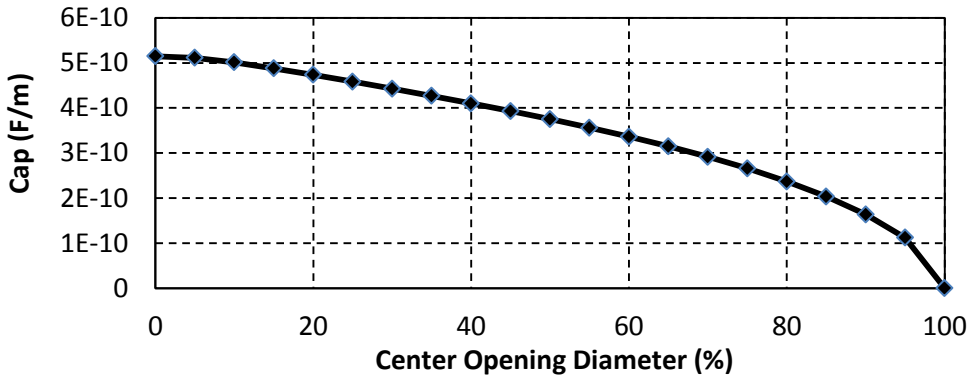

Figure 3.10 Capacitance change versus center opening diameter, given as a percentage of the membrane diameter, here 4mm.

In order to study the perforation pattern effect on the capacitance, a 2-D model (no axial symmetry) is made in COMSOL™. The geometry of the perforation is varied and capacitance is measured, in that, the bottom electrode is divided into 50 pieces (the bottom electrode diameter is 4 mm in this simulation, so each block has a width of 80 μm) and perforation ratio – defined as the ratio of the perforation opening to the pitch size - is changed (Table 3.3). Boundary conditions are the same as the other capacitance model, except for axial symmetry. Details of parameters and geometry of the structure are listed in Table 3.3.

Figure 3.11 and Figure 3.12 show surface charge density and the electric potential distribution, and Figure 3.13 shows simulated change in capacitance vs. perforation ratio in the perforated electrode. Due to large fringing fields, the perforation ratio can be high (94%) without incurring significant (> 20%) reduction in base capacitance.

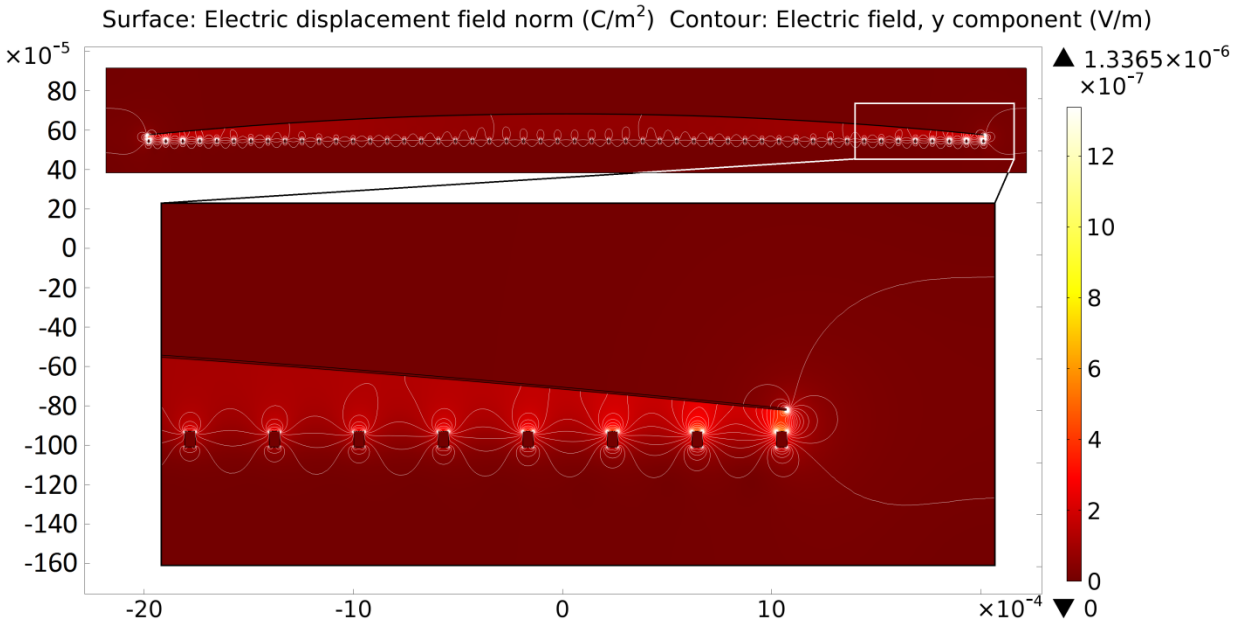

Figure 3.11 Snapshot of COMSOLTM 2-D simulation of perforation pattern effect on capacitance, showing electric displacement field (equal to charge density) and electric field contours.

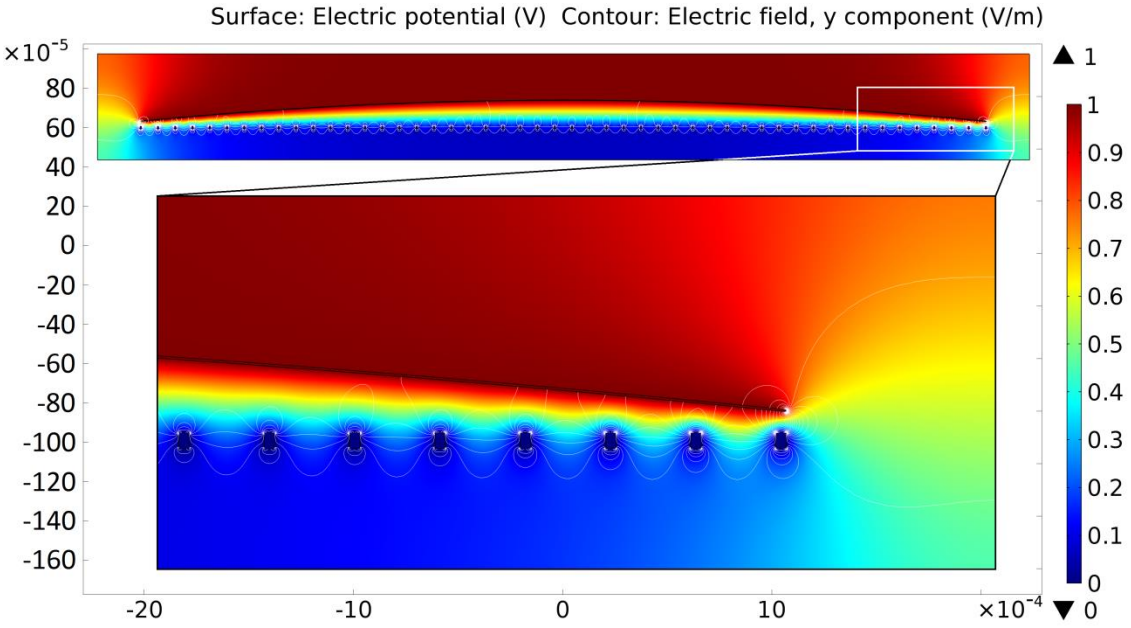

Figure 3.12 Snapshot of COMSOLTM 2-D simulation of perforation pattern effect on capacitance, showing electric potential and electric field contours.

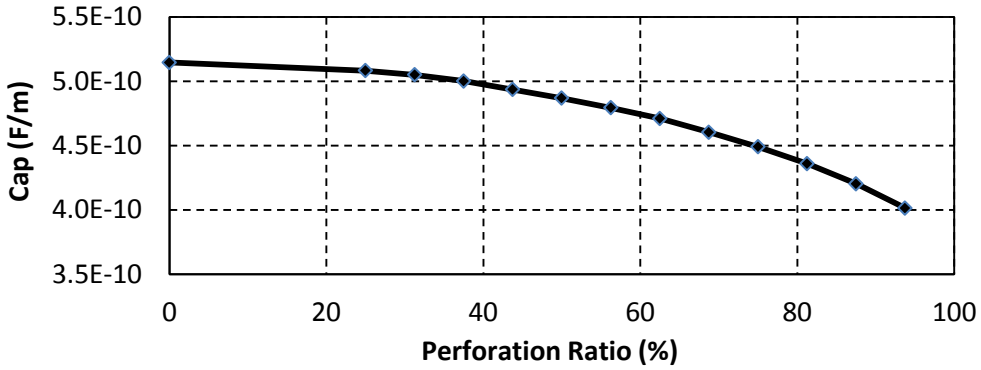

Figure 3.13 Total capacitance vs. perforation ratio. Perforation ratio is the perforation opening size divided by the perforation pitch, here 80μm.

3.2.4.2 Transient Response vs. Opening Size

In this section, the transient response of the sloped-walls EMH structure in sensing mode with various center opening sizes is studied. The 2-D COMSOL™ model used in this structure is configured in sensing mode, i.e. a step pressure is applied to the front (smaller) side membrane and the transient response of the back side is calculated by COMSOL™. The capacitive electrodes are on the back side and the flat electrode has a center opening whose diameter is varied. Front side diameter is 0.5 mm and that of the back side is 1 mm. Boundary conditions are the same as those used in simulations in Section 3.2.2 and no-slip condition is applied to all the edges of the annulus form membrane inside the liquid. The membrane on the back is not perforated. Figure 3.14 plots the variation of the settling time with respect to center opening diameter stated in percentile of the back side membrane diameter. The settling time is defined as the time elapsed from application of the step pressure to the time at which the deflection of the membrane enters and remains within a 5% percent error band of the final value. It should be noted that for values above 1 sec, the settling time is extrapolated based on the transient curve up to 1 sec. This extrapolation is time saving as each simulation run takes many hours to complete.

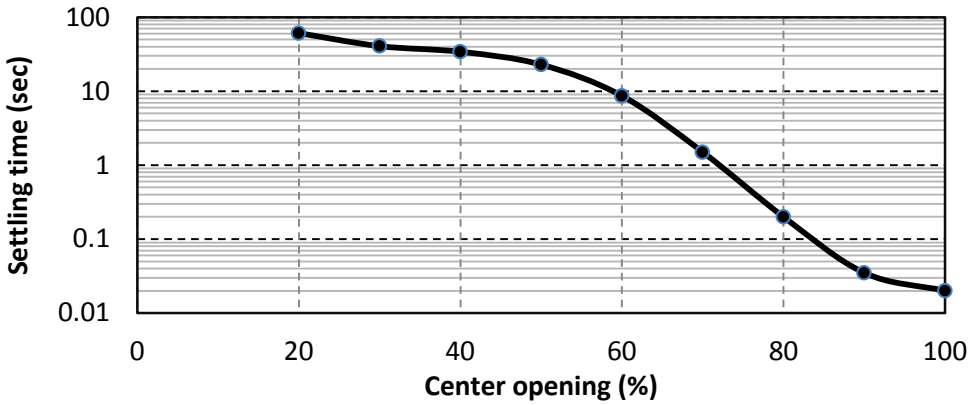

Figure 3.14 Variation of membrane settling time vs center opening diameter in sensing mode.

3.2.4.3 Transient Response vs. Perforation Pattern

In this section, the combined effect of perforation and center opening size on the membrane is studied. The goal is to design a sloped-wall EMH structure with settling time as small as possible, while maintaining sensing capacitance. Based on capacitance modeling in Section 3.2.4.1 and transient response modeling of the EMH structure in Section 3.2.4.2, it is known that the center opening size of 25-55% causes 10-30% reduction in capacitance, while it can significantly increase the speed. Therefore, perforation combinations are chosen as follows: perforation ratio of 60% and 80% and center opening size of 24%, 45% and 55% are tested. The COMSOL^{TM} model is the same as the one used in Section 3.2.4.2, only the membrane is perforated. Boundary conditions are the same as before. Figure 3.15 shows a snapshot of this COMSOL^{TM} simulation, with perforated membrane and no center opening. In this figure, deflection of the back side membrane, velocity field along with the streamlines and direction of flow (arrows) at time 100 msec are plotted. Figure 3.16 plots the response time of the perforated membrane with abovementioned perforation ratio and center opening size combinations. Based on these analyses, perforation ratio of greater than 80% and center opening sizes ranging from

50% to 65% of the membrane diameter are chosen. This will cause 32-43% capacitance reduction while increasing device speed by more than 400× [45].

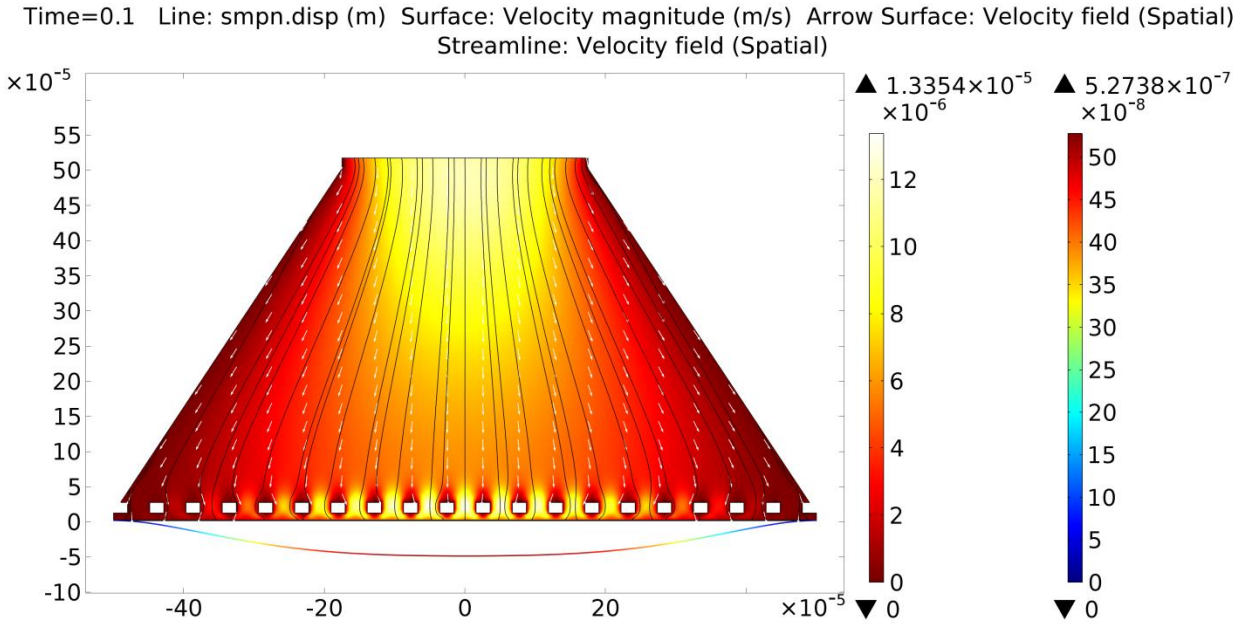

Figure 3.15 Snapshot of COMSOL simulation of sloped-wall structure with perforated membrane in sensing mode, showing displacement of the back side membranes, velocity field streamlines, direction and magnitude at 100 msec.

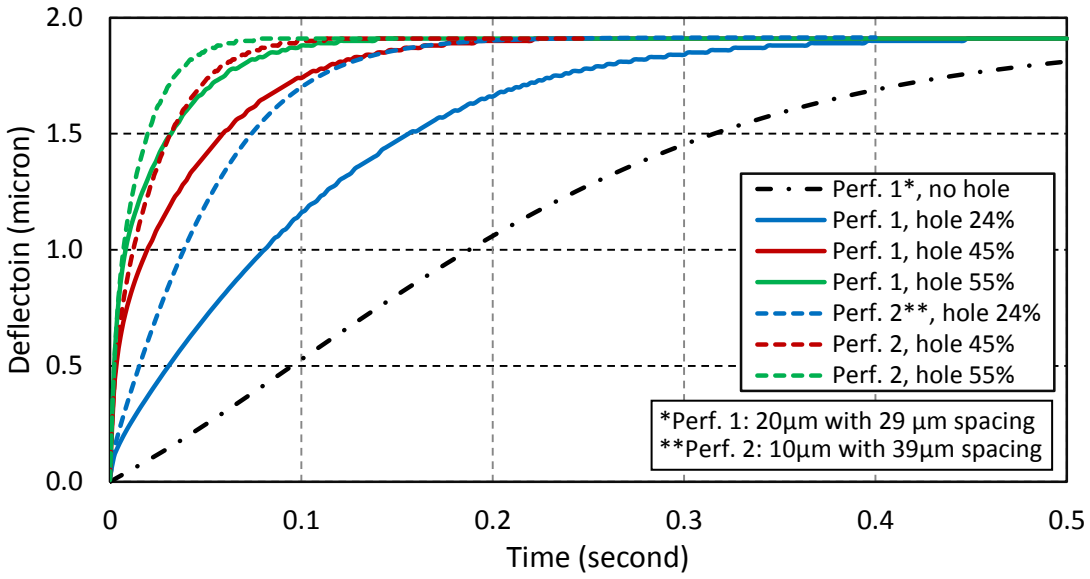

Figure 3.16 Comparison of transient responses for perforated membranes with two different perforation patterns and various center hole openings. Perforations 1 and 2 consist of 29-µm and 39-µm gaps between adjacent 20-µm and 10-µm wide silicon traces, respectively. The hole percentage is the ratio between the open hole diameter and the membrane diameter.

It should be mentioned that all the simulations are performed in 2D and the results approximate the actual device geometry. The perforated membrane in the 2D model is actually a "striped" structure with infinite long elements, whose cross section is given in figure of Table 3.3. Nevertheless, in the final design, the perforated membrane is a plane with an array of circular holes (Figure 3.19) and the diameter of the holes to pitch size of the array is the perforation ratio. It is clear that the 3D perforation results in lower fluidic resistance. Hence, it is expected that 2D COMSOL^{TM} simulations overestimate the settling time.

3.2.5 Parylene Thickness

EMH structures for sensing and actuation are required to have symmetric response time. In other words, rise and fall times of the structure should be the same. It is expected that the system parameters affect rise time and fall time differently: rise time is set mainly by hydraulic system response time while fall time is determined by membrane elasticity. Using the COMSOL^{TM} model developed in Section 3.2.4 with a pulse input pressure instead of a step pressure, rise and fall times of the EMH structure in the sensing mode are obtained. To study the effect of membrane elasticity, parylene with 1 µm, 1.5 µm and 2 µm thicknesses are used. Coarse steps in thickness variation are chosen since the parylene deposition tool cannot reliably control the thickness of parylene. The maximum thickness accuracy is within ±200 nm. The results are plotted in Figure 3.17. These simulation results show that with variation of parylene thickness the rise time in all three cases remains almost the same, whereas, the fall time changes significantly with the membrane thickness. Therefore, it can be concluded that the dominant rise-time component is hydraulic response time, while parylene membrane elasticity dominates the fall-time. As shown in Figure 3.17, a change in the membrane thickness increases its

moment of inertia, which reduces the fall time and maximum deflection. For the device geometry modeled here, a 2 μm thick parylene film results in a symmetric time response [46].

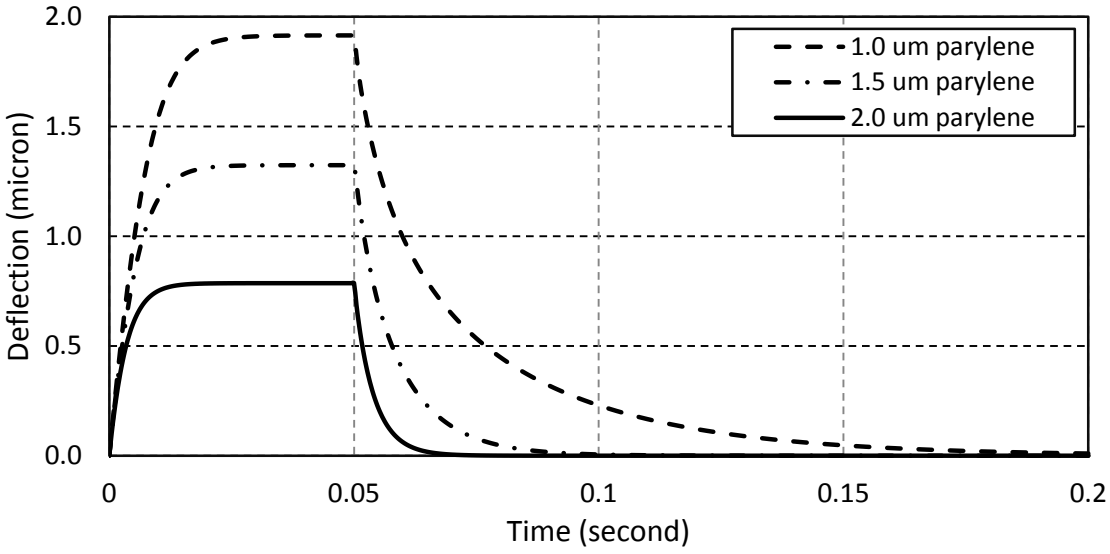

Figure 3.17 Simulated rise and fall of the backside membrane in response to pulsed pressure on the front side, i.e. simulated sensor operation.

3.3 Fabrication

For fabrication of the sloped-wall EMH structure, the same silicone fluid, Cytop™ hydrophobic layer and direct parylene coating on liquid technique are used. However, to accommodate the perforated structure, the fabrication process established for the first generation EMH structures requires modification. Figure 3.18 schematically shows the fabrication process of the sloped-wall EMH. It starts with the definition of a backside recess by DRIE, followed by deep boron diffusion. This recess determines the capacitance gap. The deep boron diffused layer has a thickness of about 13 μm. The perforation pattern and front side chamber's opening are DRIE etched 20 μm deep through this layer on the front and back sides, followed by EDP to etch the channel and release the electrode while other features on the front side are protected with a blanket 1 μm LPCVD oxide layer. Perforated patterns are designed in a way that the

anisotropically-etched pyramid under each opening overlaps with adjacent ones to fully release the electrode and form sloped-wall channels. After the EDP etching step, the protective oxide layer is stripped in HF. Hydrophobic Cytop^{TM} layer is sprayed on and patterned on both sides. This layer repels the silicone fluid so that the oil will be contained in Cytop^{TM} free areas. The silicone oil (1,3,5-trimethyl-1,1,3,5,5-pentaphenyltrisiloxane) is dispensed and kept in place due to surface tension and hydrophobic Cytop^{TM} layer. This particular silicone oil has a very low vapor pressure, so it does not evaporate inside the parylene deposition vacuum chamber. Once the oil is dispensed on the wafer, in a single deposition run, a 2 μm parylene layer encapsulates the silicone liquid. The final metal layer forming the second electrode is deposited through a shadow mask on the backside. Figure 3.19 shows fabricated EMH chips with perforated electrodes. This fabrication process is highly reproducible, in that over 100 EMH chips have been successfully fabricated. In a typical fabrication run, almost all devices survive until liquid dispensing step, after which about 80% are processed to the final stage. This shows the fabrication process has high yield and it is highly reliable.

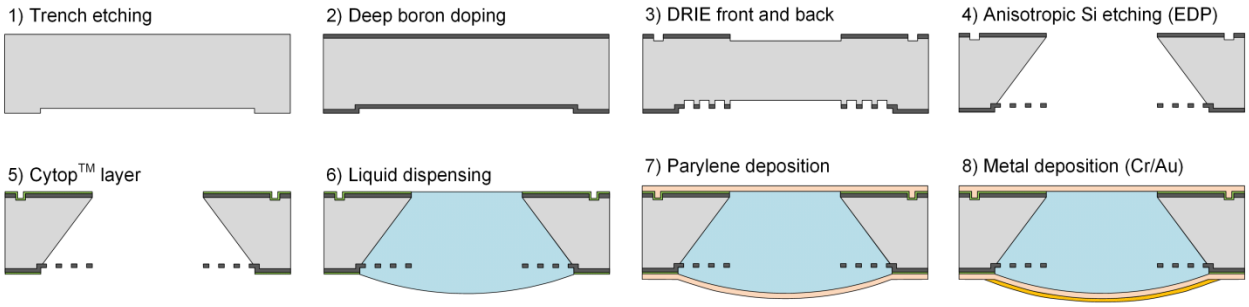

Figure 3.18 Fabrication process of 2nd generation EMH.

The silicon chip is mounted on a glass interposer, which is a glass substrate that is recessed in selected areas to protect the backside membrane and provide interconnections (Figure 3.20). The recesses are deep enough to allow backside membranes to fully deflect at the full-scale force range. Using the glass interposer, direct wire bonding to the device is made possible; wire

bonding cannot be performed on substrates with parylene coating. Another advantage of the glass interposer is reduced parasitic capacitance due to running long metal traces on the glass instead of thin parylene membrane. The packaged device is shown in Figure 3.20.

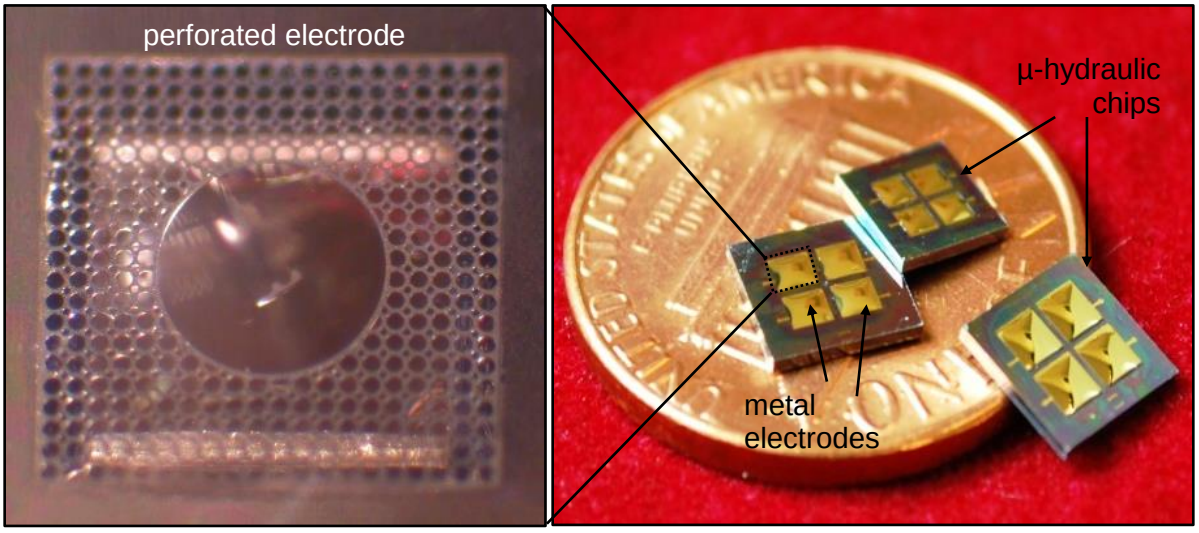

Figure 3.19 Second generation EMH devices. Left: perforated membrane of the μ-hydraulic chip seen through silicone oil and parylene before metal deposition.

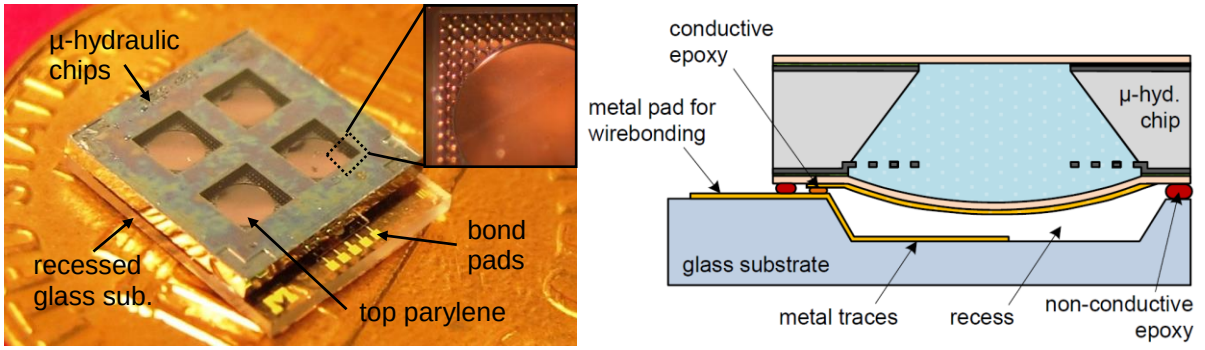

Figure 3.20 Right: μ-hydraulic chip on top of the glass interposer. Left: A packaged device including the glass chip and perforated electrode seen through top side parylene.

3.4 Experimental Results

To characterize the fabricated EMH structure, sense mode operation is mimicked by actuating the front-side with a piezoelectric beam actuator and measuring backside deflection by laser Doppler vibrometry (LDV). The LDV function generator directly actuates the piezo-electric beam and velocity of the membrane is measured by the tool based Doppler effect. The

velocity is then integrated to obtain displacement. With this technique, the frequency response of the devices can be measured. It should be noted that the frequency response of the piezro-resistive beam is separately measured and its bandwidth is far above the bandwidth of EMH structure. The LDV measurement setup is schematically shown in Figure 3.21.

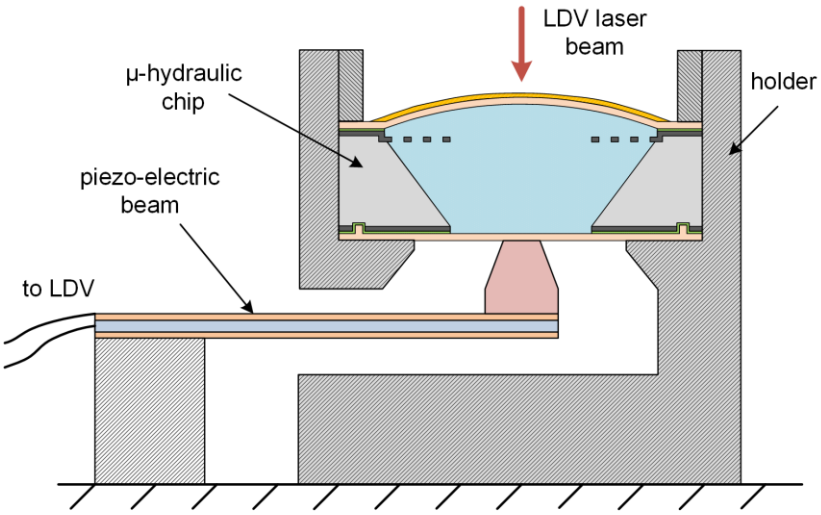

Figure 3.21 LDV measurement setup, the piezo-electric part is actuated by LDV tool, and the deflection on the membrane is measured by laser beam.

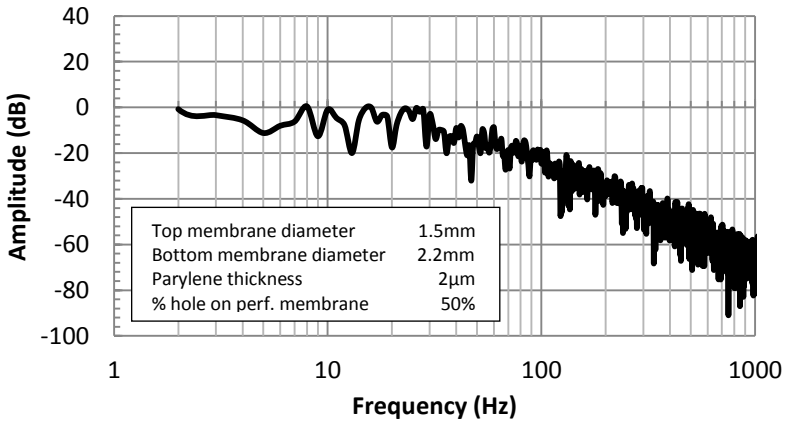

Figure 3.22 Frequency response of a fabricated sloped-wall device with perforated membrane, which shows bandwidth of about 50 Hz, equivalent to a response time of approximately 25 msec.

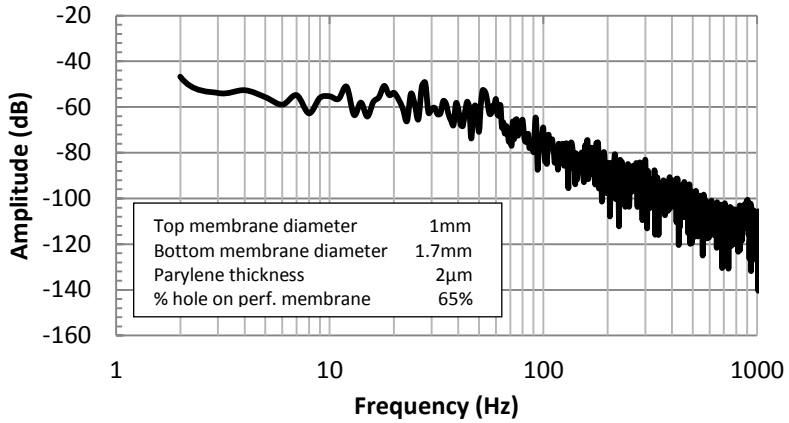

Figure 3.23 Frequency response of a fabricated sloped-wall device with perforated membrane, which shows bandwidth of about 70 Hz, equivalent to a response time of approximately 18 msec.

Frequency response is measured for three different devices, two of which are plotted in Figure 3.22 and Figure 3.23. These devices vary in size and/or perforation pattern. They exhibit a maximum bandwidth of 70 Hz, which corresponds to an 18 ms sensor response time. As can be seen from these figures, EMH structures of various geometries show bandwidths of 50 to 70 Hz. The bandwidth range comes from variation in the center hole opening on the perforated electrode. A 50 Hz bandwidth corresponds to the smallest center opening size (i.e. 50% of electrode diameter) while 70 Hz corresponds to the largest center opening size (i.e. 65% of electrode diameter). The third device with opening diameter of 55%, exhibits a bandwidth of about 60 Hz. The bandwidth range of EMH devices is comparable to pneumatic and piezoelectric hydraulic devices which require external actuators [1, 14, 31, 15, 2, 3, 35, 34], while in this work, the electrostatic sense/actuate element has been integrated into the micro-hydraulic device.

3.5 Discussion

The EMH structure presented in this work is a second order system. Depending on the structure geometry, architecture and material physical properties, the response of the system in

the time domain can be over-damped, under-damped or oscillatory. This behavior of the system can be observed in FEA simulations as well. To bring the system to the brink of oscillation, the damping factor in the structure should be minimized. In this system, the fluidic resistance functions as a damper. This resistance depends on structural architecture (e.g. sloped-wall vs. straight-wall) and viscosity of the fluid. Therefore, sloped-wall is chosen as it providesminimal fluidic resistance. Three fluids (e.g. air, water and oil) to exhibit all three types of time domain response behaviors are examined. For this simulation, the COMSOL^{TM} model in Section 3.2.2 is used and air is considered to be incompressible.

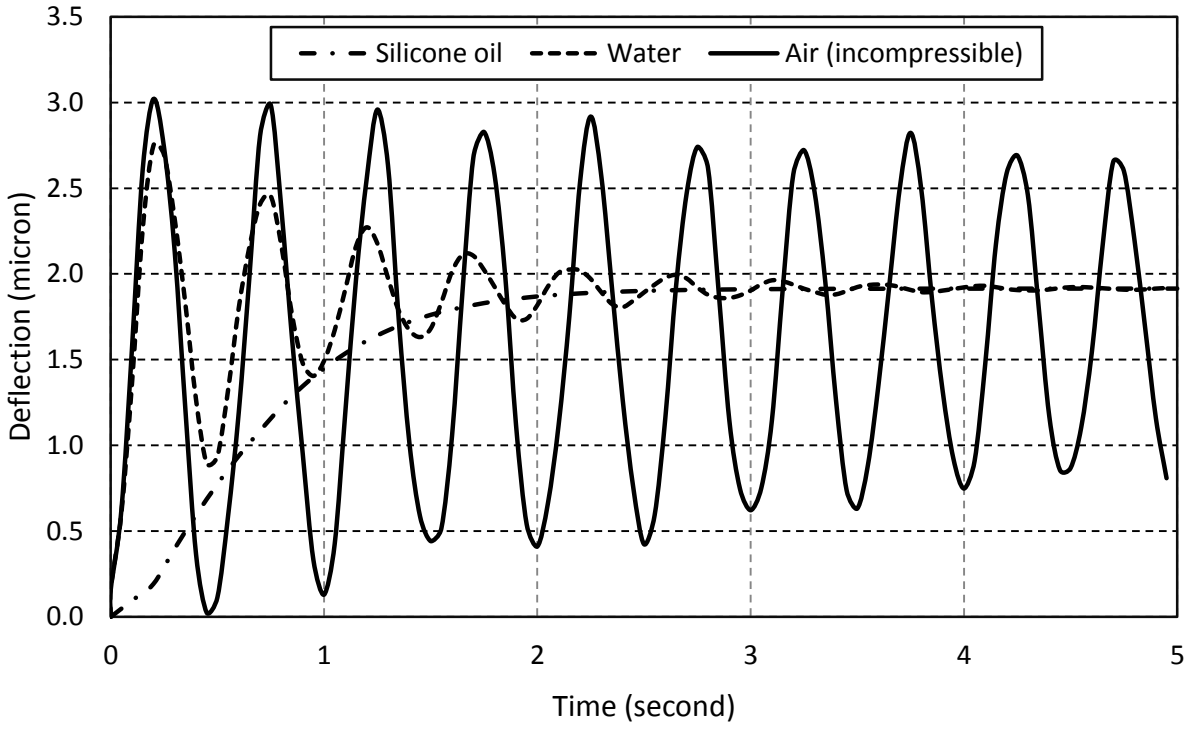

Figure 3.24 Transient response of sloped-wall micro-hydraulic (without perforated membrane) with various types of liquids.

Transient responses of the three fluids in sloped-wall EMH system is plotted in Figure 3.24. Silicone oil has the highest viscosity, therefore maximum damping with the rise time of 1.7 msec (10% to 90% measure). Water response is under-damped with the overshoot of 45%, rise time of

0.2 and settling time of 3 msec. Air response time is very close to oscillation; overshoot is 63%, rise time is slightly less than 0.2 msec and settling time is greater 50 msec. If a thinner parylene membrane (thicknesses smaller than 1.5 μm) is used, the membrane resonates.

Depending on the application, the EMH can be designed to operate in resonance or damped mode. For applications such as pressure sensing, neither resonance nor under-damped responses are desired. Therefore, should the EMH be used with lower viscosity fluids, the architecture of the fluidic path has to be redesigned for optimum time domain response. For instance, one might increase the fluidic resistance to avoid oscillation of the membrane. In this chapter, however, minimum fluidic resistance is chosen since the silicone fluid has high viscosity. Resonating EMH structures can also be very useful. They can be utilized for realization of 2-D haltere-like gyroscopes [47] or for other forms of inertial force measurements. In case of resonating devices, minimum fluidic paths and damping are required. Due to presence of liquid, however, micro-hydraulic resonance devices will exhibit high damping, therefore low quality factors.

Bandwidth of the sloped-wall EMH system discussed in this section can be further improved by utilizing lower viscosity material, lighter fluid, thinner silicon substrate and thicker parylene layer. Lower viscosity material directly reduces the fluidic resistance and lighter material causes the fluidic inertance to be lowered (reduced density), therefore both may contribute to increased bandwidth. Moreover, using thinner substrates directly reduces both fluidic resistance and inertance, hence further increasing the bandwidth. Additionally, by thickening the parylene layer fluidic capacitance is reduced, consequently bandwidth is increased. This improvement, however, comes at the expense of deteriorated sensitivity, since for a given pressure, thicker parylene deflects less than a thinner parylene. Nonetheless, for applications which bandwidth is

the first priority, sensitivity may be traded off for bandwidth. With these modifications, the EMH bandwidth may be increased up to the acoustic range, i.e. a few kHz.

EMH structures in sensing mode will facilitate realization of very low power sensors. Low power consumption of the EMH sensing unit is due to its passive mode of operation in that extremely low power is needed to charge the capacitors, compared to thermal or pizeo-resistive transduction mechanisms. In both thermal and piezo-resistive methods, either a large current is needed to heat up the sensing element or bias a bridge circuit. For EMH based sensors, however, the overall power consumption equals to readout circuitry power usage, which can vary from hundreds of microwatts to a few milliwatts.

EMH units size can be scaled to smaller geometries. Fabricated EMH cells have footprint sizes ranging from less than 1×1 mm^2 to 2.2×2.2 mm^2. Their sizes can be further shrunk; however, the size reduction might adversely affect the performance. In order to practically accommodate an appendage on the front side, the EMH front size cannot have diameters smaller than 200μm, therefore, if the hydraulic amplification is set to unity (i.e. the front and back sides have the same surface area), the EMH footprints including the interconnections are within 250×250 μm^2 area. If hydraulic amplifications of about 5 is desired, the footprint will increase to about 500×500 μm^2. Reducing the size, however, lowers both sensitivity and bandwidth. The former is lowered due to reduced base capacitance and the latter is deteriorated because of the significant increment in hydraulic resistance with reduction is channel geometries. Reduced base capacitance can be compensated by taking advantage of liquids with higher permittivity and using lower viscosity materials helps mitigate the effect of hydraulic resistance increase on bandwidth. The scaling is discussed in future works subsection of Chapter 6.

3.6 Conclusion

In this chapter, a novel optimally designed high-speed EMH structure has been introduced. Dynamics of this system have been analyzed through simulation and the results are used to develop a new architecture which reduces the response time of the EMH by several orders of magnitude. The EMH structure is well suited for high performance, low power sensing applications where wide dynamic range and high resolution are needed. It can also be used for devices where large out of the plane actuation is required. The new micro-hydraulic structures are successfully fabricated and tested. The devices offer a high measured bandwidth between 50 to 70 Hz, and based on simulations the rise and fall times should be symmetric. In the future, other fluids with low viscosity could be used to achieve even faster devices.

4 Chapter 4: μ-Hydraulic Hair-like Air Flow Sensors (HAFS)

4.1 Introduction

Hair-like structures are extensively used in nature in various forms for sensing and actuation. They can have numerous functionalities including sensing of flow, rotation, sound, vibration, and actuation for thermal control, liquid manipulation and many other applications. In passive mode, they are used for thermal isolation, shielding, air particle filtration, etc. Hairs have several attractive features that make them a generic platform for various applications. For instance, they have very large surface to volume ratio, a critical property for efficient interaction with the environment. They also can be raised or retracted to accentuate/minimize their function, for instance thermal isolation. Furthermore, hairs have high aspect ratio, therefore producing a very small footprint while maintaining large mass and surface area. When hairs are used as a sensory organ, they take advantage of local signal transduction. These and many other features potentially enable new functionality and improved sensor performance.

Hair-like structures can provide air flow sensing with high accuracy and high resolution. The hair-like post is immersed in a fluid and dragged by fluid flow. The drag force exerted on the hair deflects it, which is then sensed by neural system underneath. Hairs can be used to detect small flow speeds since even a very small flow velocity causes hair deflection, which results in amplified force at the base that can be sensed. It is reported that flow velocities as small as 30 μm/s can be sensed with this mechanism [22]. The dimension of hair can determine its dynamic range and frequency response. For instance, tall hairs are sensitive to smaller flow velocities while their bandwidth is narrower, compared to those of short hairs [48]. Hairs with small

footprints enable dense array fabrication to provide redundancy and fault tolerance. In some cases, arrays of non-homogenous hair-like sensors can be used to broaden the functionality of the hair sensors. For instance, crickets use an array of non-homogenous hairs to cover a wide scope of frequency and range [48]. These make the hair structures a potentially excellent architecture for flow velocity measurement.

Many research groups have studied hair-like structures for flow sensing [22, 21, 27, 20, 23, 16, 49, 25]. However, they usually use either very fragile structures or exposed sensitive elements, both of which limit the use of the hair sensors in outside environments [21, 23]. Examples of these hair-like air flow sensors (HAFS) and their features are investigated in Chapter 1. Additionally, the concept of micro-hydraulic structures that can decouple sensitivity and range by spatially separating the applied and sensed deflections [50], is introduced in Chapter 2 and Chapter 3. To achieve high sensitivity in conventional capacitive sensors, a narrow gap is needed which lowers the range due to limited maximum plate deflection. On the other hand, when a large measurement range is required, a wide gap is needed, which deteriorates sensitivity. In contrast, a micro-hydraulic structure can provide a wide gap on one side for large dynamic range and a narrow gap on the opposite side for high resolution sensing. Furthermore, sensors utilizing micro-hydraulic structures may be more robust to use in the outside environment due to the enclosed capacitive gap. The enclosed gap protects the sensing mechanism from external particles such as water droplets and dust that might otherwise disrupt sensing. In addition, due to the use of liquid gap capacitive sensing [50, 45, 3], the sensor capacitance increases by a factor equal to the permittivity of the liquid (~ ×3 in this case), and hence the sensitivity is enhanced. As a result, sensors utilizing micro-hydraulic structures are robust devices that can deliver high sensitivity over a large dynamic range.

4.2 Principle of Operation

The micro-hydraulic HAFS and array of HAFS are schematically shown in Figure 4.1. It consists of two major parts, the micro-hydraulic sensing unit [50, 34, 51] in the base and the hair appendage attached on top of EMH system. To create an air flow sensor, the hair-like post that extends from the surface out of the plane of the substrate converts the air drag force into pressure on the boss and thus on the front-side membrane. The boss pushes the liquid toward the back side, deflecting the back-side membrane. A pair of metal electrodes is deposited on the back side parylene membrane and on the substrate underneath to form a capacitor. As flow speed increases, the membrane deflects, and the capacitance decreases monotonically.

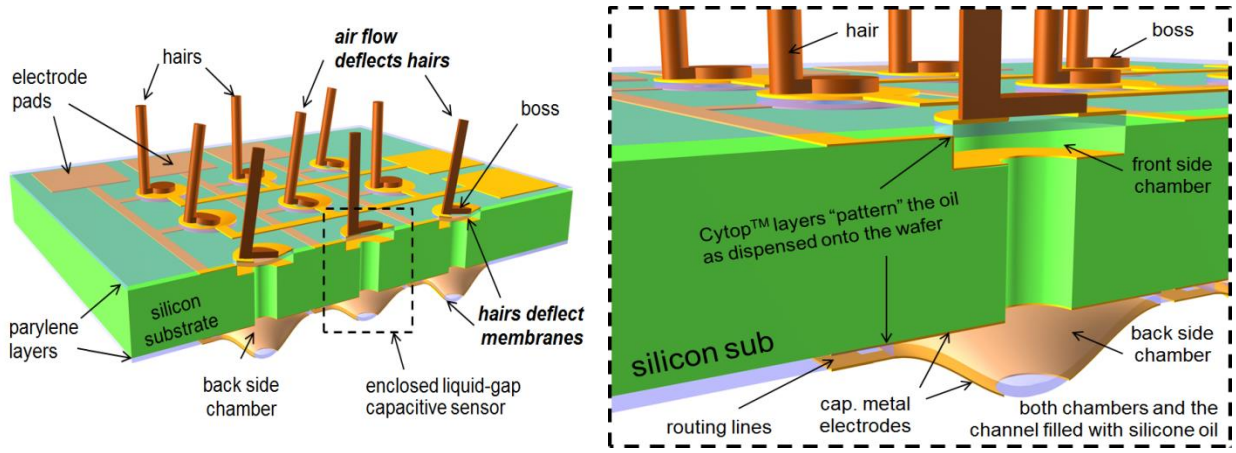

Figure 4.1 Array of micro-hydraulic HAFS structure.

In this chapter, two generations of micro-hydraulic HAFS are investigated. The first utilizes the straight-wall channel configuration described in Chapter 2 along with prefabricated "pins" as hairs [50]. The second utilizes an optimally designed integrated hair-boss structure for substantial improvement of the HAFS performance. In the first generation, hairs are manually attached to micro-hydraulic chips using a micromanipulator to form HAFS [50, 45]. Manual handling of the sensor components slows fabrication and causes large process variation. On the contrary, in the second generation HAFS, after optimization of the hair-boss structure stereo-

lithography apparatus (SLA) is used to fabricate an array of 3-D integrated hair-boss structures that can be attached to micro-hydraulic chips at the die or possibly the wafer level. The SLA machine used for hair-boss fabrication is Viper SI2 (3D Systems, Inc.) [52], which operates based on laser-assisted polymerization of Accura® ClearVue [53] polymer. This technique allows for precise positioning of the sensor over the micro-hydraulic sensing cells. The hair-boss structure and its dimensions are optimized to further improve the sensitivity of HAFS. Intentional asymmetries in the design of the integrated hair-boss, along with off-center positioning of the hairs on top of micro-hydraulic chip, are used to build, for the first-time, a 2-D directional flow sensor using an array of four HAFSs.

4.3 First Generation Micro-Hydraulic HAFS

The first generation HAFS utilizes the straight-wall micro-hydraulic unit described in detail in Chapter 2 of this dissertation. To form the HAFS, the hair appendage (prefabricated pin) should be added to EMH system and a process should be developed to allow for the integration without altering the mechanical properties of the EMH.

4.3.1 Hair Integration with EMH

A technique to integrate a silicon boss as a platform for attaching hair appendages is established. In this technique, to form the bossed membrane schematically depicted in Figure 4.1, the fabrication process is slightly modified. As shown in Figure 4.2 parts 5-1 and 6-1, after liquid dispensing, a 100μm-thick silicon disk is put over the fluid, and then parylene is deposited. The disk does not sink and is aligned in the center due to surface tension. The bossed membrane is shown in Figure 4.3. Figure 4.4 is surface profile of a bossed membrane.

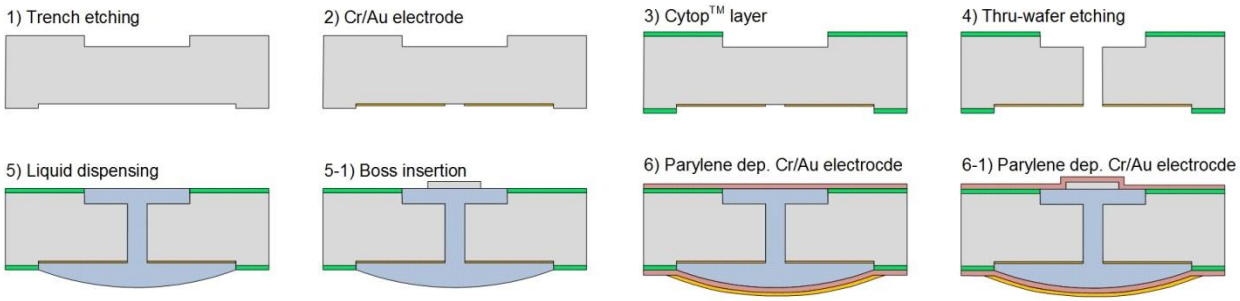

Figure 4.2 Fabrication process of modified EMH structure. Trenches and through-wafer channels are formed by DRIE. Cytop™ is a spin on polymer that makes the surface hydrophobic. Therefore, the fluid will be contained in Cytop™ free areas. . In the parylene deposition step, surface tension keeps the liquid in place. Integration of the boss is shown in process steps 5-1 and 6-1.

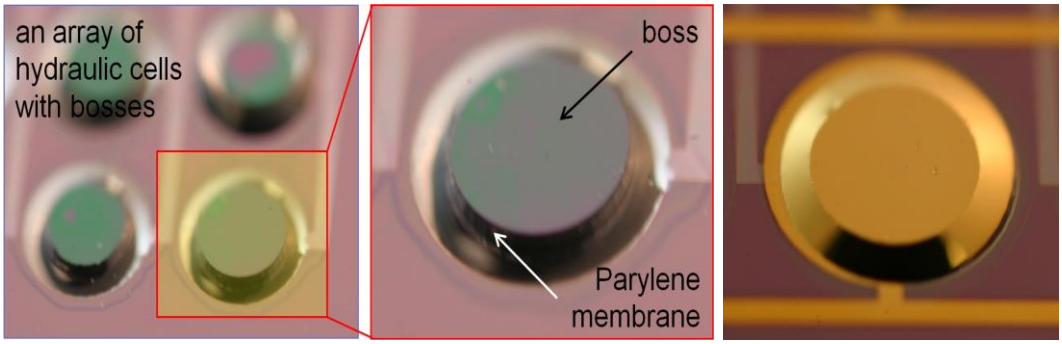

Figure 4.3 An array of micro-hydraulic cells with bossed top membranes. As shown in the figure, the boss does not sink into the fluid and is self-aligned in the center.

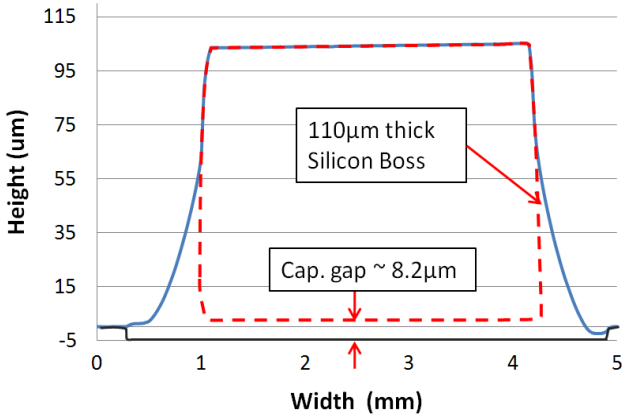

Figure 4.4 Surface profile of one cell with bossed membrane over a 4.5 µm trench. As shown in the image the boss is aligned in the center and it rests in a fairly flat position.

After boss integration, a pre-fabricated pin can be attached to the boss in a minimally invasive way without excessive adhesive/paste reflow or residues, which might alter the parylene membrane mechanical properties. An air flow sensor is made by attachment of a hair on a

bossed membrane using silicone elastomer epoxy. Figure 4.5 shows the first generation of micro-hydraulic HAFS. The boss under the pre-fabricated pin can be clearly seen.

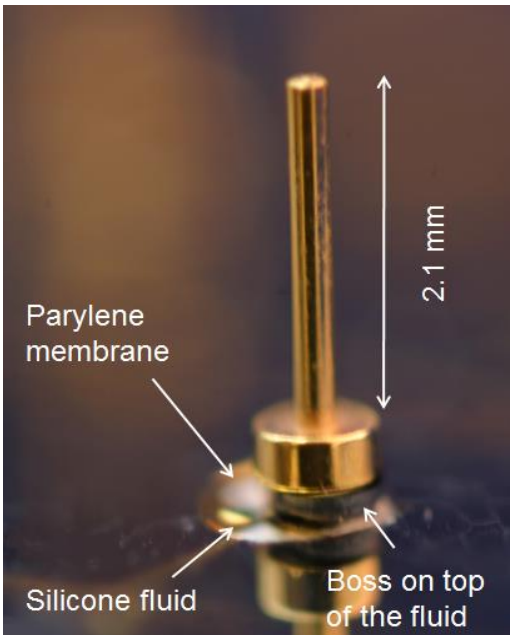

Figure 4.5 The first generation micro-hydraulic HAFS. In this hair sensor the hair (a prefabricated pin) is attached to the front-side membrane over the boss. On the top left, the back side of an array of four cells is shown.

4.3.2 Experimental Results and Analysis

The fabricated devices have been tested in a wind tunnel. The sensors are placed in the laminar flow region of the tunnel. The air flow speed is monitored with a commercial hotwire anemometer located next to the sample while the capacitance change is measured with a HP 4284A LCR meter. Figure 4.6 shows measured capacitance change versus air flow speed. The sensor operates over a wide range up to 10 $m \cdot s^{-1}$. Five different sensors were fabricated and measured. For five different devices, the low flow sensitivity was found to range from 230 to 440 $fF/(m \cdot s^{-1})$, with an average of 333 $fF/(m \cdot s^{-1})$. For the device shown in Figure 4.5, the low flow sensitivity is 315 $fF/(m \cdot s^{-1})$. Therefore if the capacitive readout circuit can detect a capacitance change of 1 fF, the minimum detectable flow is ~3 $mm \cdot s^{-1}$.

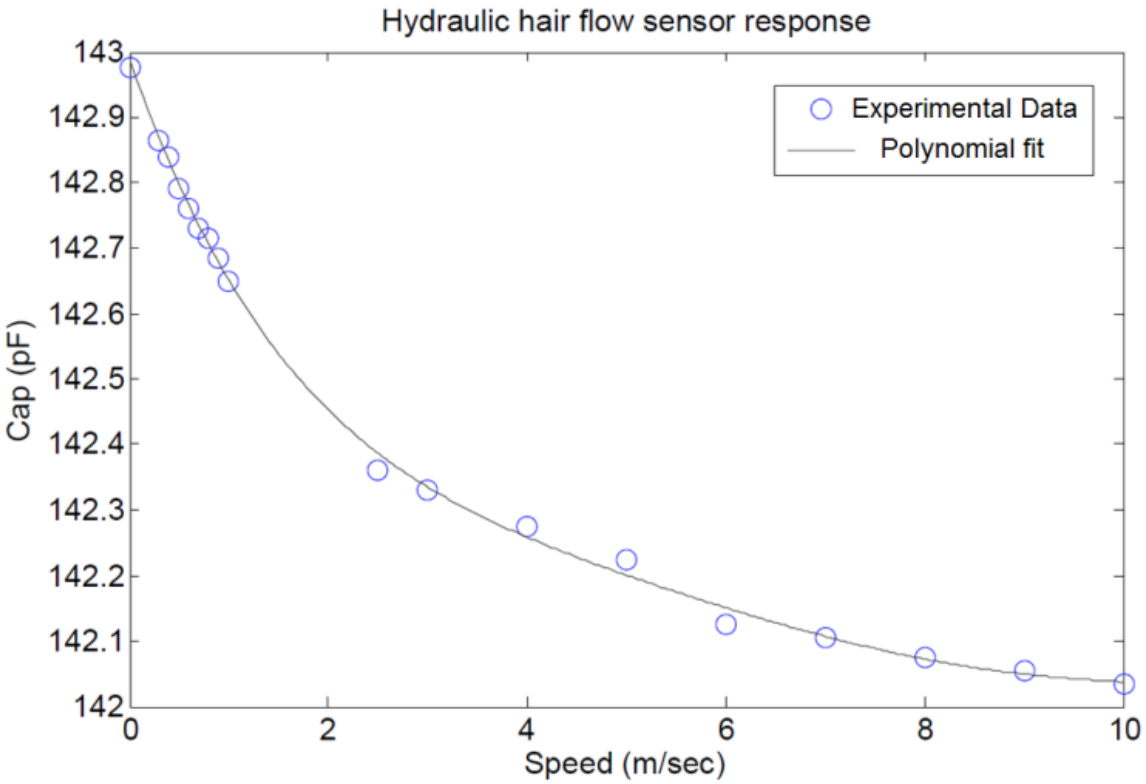

Figure 4.6 Micro-hydraulic air flow sensor response to air flow speed. In the low flow region (for 0-1 m.s^{-1}) the capacitive rate of change is 315fF/m.s^{-1}. The data fit line is a 5th-degree polynomial. The variation of measured data from the fit line is used to determine the 1 cm.s^{-1} resolution of the sensor.

To verify the experimental results, the structural mechanics component in the MEMS module of COMSOL™ is used to model the micro-hydraulic hair air flow sensor. The dimensions of the fabricated device characterized in Figure 4.6 were used in the model (Table 4.1).

Table 4.1 Dimensions of fabricated device used in making the COMSOL model. Dimensions match the device characterized in Figure 4.6.

Parameter	**Value**
Parylene membrane thickness	1 µm
Front parylene membrane diameter	1 mm
Back parylene membrane diameter	2.24 mm
Hair height	1.9 mm
Hair diameter	220 µm
Boss thickness	118 µm
Boss diameter	474 µm
Front side recess depth	4.5 µm
Back side recess depth	2 µm

The simulated membrane and hair structure are shown in Figure 4.7. For a given air flow, the resultant drag force on the hair is calculated analytically. This force is then applied to the hair tip in COMSOL™, which predicts the resultant deflection of the tip and the 3-D membrane displacement. From the displacement, the volume change under the front-side membrane is calculated. Assuming the silicone oil is an incompressible fluid such that the entire liquid volume change is transferred to the back side, the back side membrane deflection is calculated. Using the capacitance-gap relation of a curved electrode capacitor, the expected change in back side capacitance is determined. The back side curved electrode geometry and the equations used to calculate the volume and capacitance between the curved electrode and the flat electrode are given in Table 4.2. Note that these equations assume that the height of the liquid droplet is much smaller than its diameter.

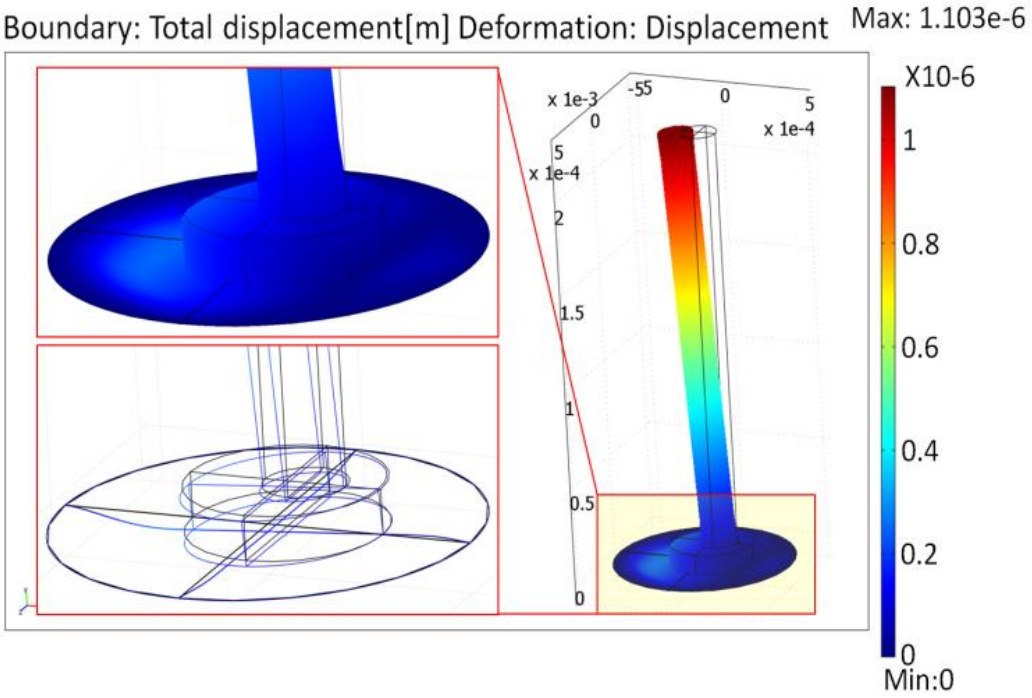

Figure 4.7 Simulation result of a hair deflected in response to air flow with a speed of 1 m.s-1 (i.e., a drag force of 0.157 μN is applied to the hair tip.) The radial displacement is plotted at 128.5× its actual value, for visibility.

For the geometry of the device characterized in Figure 4.6, simulation predicts that at 1 $m \cdot s^{-1}$ of air flow (or 0.157 μN at the hair tip), the tip of the hair appendage will be deflected by 1.103 μm. This deflection is shown on the right in Figure 4.7, where the radial deflection is amplified in the plot by a factor of 128.5 in order to make it visible. This causes a front side membrane deflection of 300 nm and a volume change of 6.28×10^{-14} m^3 under the front side membrane. This corresponds to a predicted back side maximum membrane deflection of 32 nm resulting in a capacitance change of 150 fF. This is of the same order of magnitude as the measured result of 230 fF capacitance change for 1 $m \cdot s^{-1}$. Differences between the experimental and simulation results may come from ambiguity in calculations of the fluid drag force and drag coefficient at very low flow speeds (i.e., at low Reynolds number as seen in [3, 54]), and from non-idealities of the fabricated device, including slight curving of the front side membrane. Note the ~10× hydraulic amplification ratio between the front-side and back-side membrane deflection (300 nm vs. 32 nm). Table 4.3 summarizes the results.

Table 4.2 Geometry and formulas used to calculate the capacitance change on the backside of the air flow sensor

Cross section of cap. electrodes	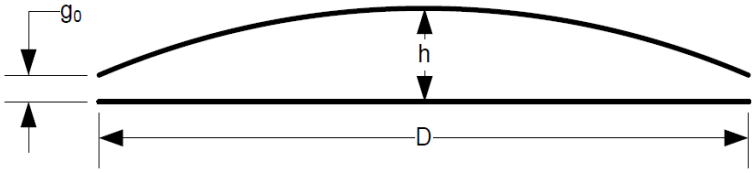
Volume	$\pi\left(\frac{D^2+4h^2}{D^2}\right)\times\left[\frac{1}{3}\left(\frac{D^2-4h^2}{D^2+4h^2}\right)^3-\left(\frac{D^2-4h^2}{D^2+4h^2}\right)+\frac{2}{3}\right]$ $if\ D \gg h \rightarrow Volume \cong \frac{\pi}{8}hD^2$
Capacitance	$\pi\varepsilon\frac{D^2+4h^2}{4h}ln\left(\frac{g_0+h}{g_0}\right)$

Table 4.3 Summary of results for 1 m.s^{-1} air flow.

Simulation results and experimental data	
Maximum deflection of the front side membrane	300 nm
Liquid volume transfer	6.28×10^{-14} m^3
Maximum deflection of the backside membrane	32 nm
Backside capacitance change (Modeling)	150 fF
Backside capacitance change (Measured)	230 fF

4.4 Second Generation Micro-Hydraulic HAFS

4.4.1 Design

To achieve high speed micro-hydraulic HAFS, the sloped-wall EMH structure described in Chapter 3 is used. Contrary to the first generation HAFS where prefabricated pins were used as hairs, an integrated hair-boss structure is fabricated and utilized to convert the fluid drag to hydraulic pressure. The hair-boss structure is made using high-precision stereo-lithography technique, which allows for die-level, and potentially wafer-level integration of hairs with the EMH structure. Multiple simulations are run to optimally design the integrated hair-boss structure within the stereo-lithography fabrication constraints. It is intended to optimize the hair location and boss diameter, as schematically shown in Figure 4.8. Using simulations, cross-axial sensitivity of the hair sensors is examined to properly position them in an array for 2D directional air flow sensing.

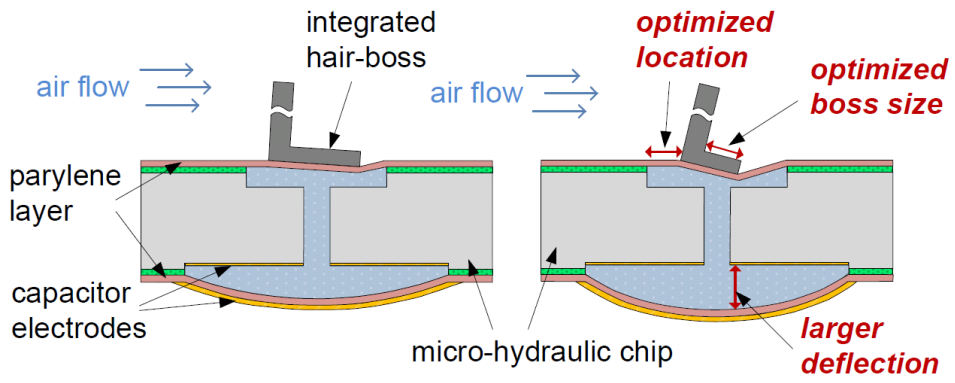

Figure 4.8 Cross section of a single HAFS. The image on right schematically shows performance improvement of HAFS with optimized hair location and boss diameter.

4.4.1.1 Hair-Boss Optimization

To obtain the maximum sensor response to air flow, the geometry of the hair-boss should be optimized so that for a given flow speed, maximum volume change under the front side membrane occurs. In the first set of simulations, the boss diameter is subject to optimization. A 3D model in COMSOL™ using the structural mechanics component is made. In the model, a 100 µm thick silicon disk is used on top of a parylene membrane, a point force is applied to the center of the boss, and its diameter is varied while the parylene membrane deflection and volume change under the membrane are monitored. Boundary conditions are as follows: fixed surfaces around the perimeter of the parylene membrane (or anchored), all other surfaces are free to move and a vertical downward point force is applied to the center of the boss. It is clear that that the optimum location for the boss is in the center of the parylene membrane, since the most compliant part of the membrane is its center [51]. Details of this simulation are listed in Table 4.4. As seen from simulation results in Figure 4.9, the smaller the boss, the larger the deflection. However, due to fabrication constraints, the boss diameter is chosen to be 50µm to obtain the maximum volume change under the membrane. Fifty micronsis the minimum feature size of the SLA.

Table 4.4 Parylene mechanical properties and dimension of the structure used for boss size optimization.

Geometry & physical properties of the parts	**Value**
Parylene membrane diameter	500 µm
Parylene membrane thickness	2 µm
Silicon disk thickness	100 µm
Parylene Young's modulus	3.2 GPa
Parylene Poisson ratio	0.40

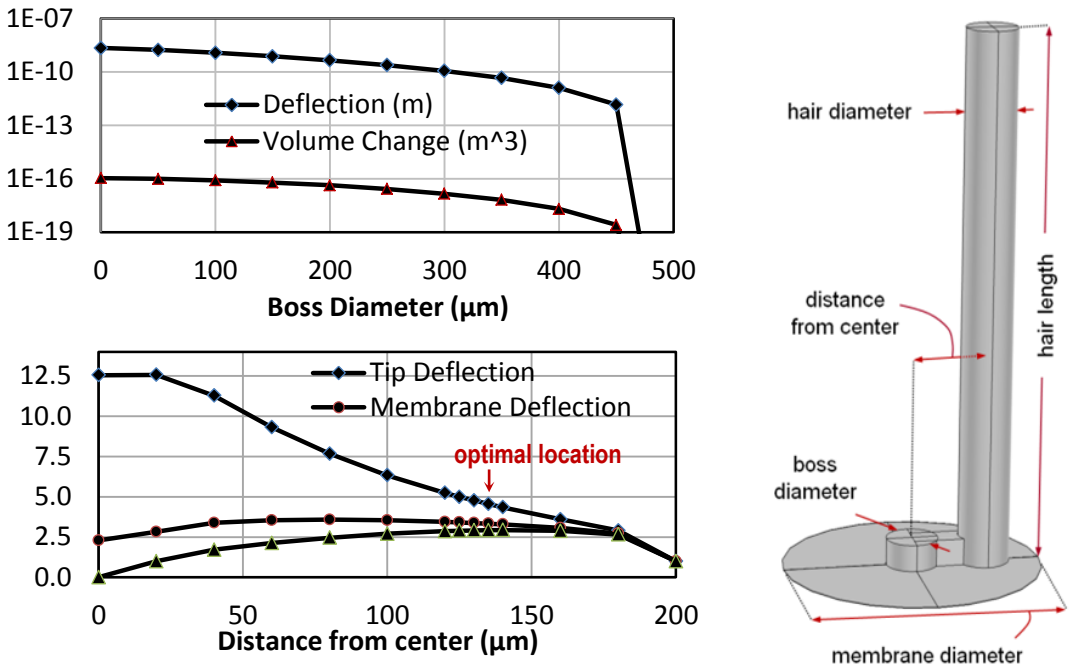

Figure 4.9 ***Top left****: parylene membrane deflection and volume change under 500 µm front side membrane as boss diameter changes.* ***Bottom left****: tip and membrane deflection and volume change vs. hair location, at constant boss diameter (all normalized to their value at 200 µm, membrane radius: 250µm).* ***Right****: schematic of hair-boss over membrane, with design parameters.*

Table 4.5 Parylene mechanical properties and dimension of the structure used for hair location optimization when the boss in the center has constant diameter.

Geometry & physical properties of the parts	**Value**
Parylene membrane diameter	500 µm
Parylene membrane thickness	2 µm
Boss diameter	50 µm
Hair length	1 mm
Hair diameter	100 µm
Si arm width (arm connecting hair to boss)	50 µm
Parylene Young's modulus	3.2 GPa
Parylene Poisson ratio	0.40

In the second set of simulations, the optimum location of the hair is found to maximize the front side membrane deflectionto achieve maximum volume displacement during constant air flow. In these simulations, for a given hair length, boss diameter and parylene membrane, a constant force is applied to the hair and the resultant hair tip and membrane deflections, and volume change under membrane are calculated by COMSOL™. When the hair location is

changed, the arm that connects the hair to the boss is also extended. It is noteworthy to mention that the hair-boss structure performs as a lever that amplifies the drag force caused by the fluid flow and applies it to the center of the membrane. The amplification ratio is equal to the hair length over the distance from the hair location to the center of the membrane. The geometry details used in this simulation are listed in Table 4.5 and it is assumed that both the hair and the boss are made out of silicon. For the boundary conditions, the perimeter of the parylene membrane is set as fixed surfaces, all other surfaces are free to move, and a lateral point force is applied to the hair tip, along the hair-to-boss axis. The results are of the simulations are shown in Figure 4.9. It is clear from this figure that the optimum point for the hair location is at 56% of membrane radius from the center. It should be noted that the tip deflection and volume change under the membrane do not necessarily follow the same trend. For instance, the maximum tip deflection happens when the hair is positioned at the center of the membrane, atop the boss; whereas, the net volume change under the membrane is at its minimum, zero. This occurs, since when the hair deflects, the membrane is partially moved upward, and partially downward. When it is in the center, its upward and downward deflections are symmetric and cancel out. Therefore, the net volume change under the membrane is zero.

4.4.1.2 Directional Flow Sensing

Off-center positioning of the hairs makes their response asymmetrical to the flow angle. In this part, cross-axial response of the micro-hydraulic HAFS is examined. To simulate this, the model developed for Section 4.4.1.1 with some minor modifications is used. In that model, the hair-boss structure is affixed on top of a parylene membrane. The hair is located at 56% of membrane radius and boss diameter is kept constant at 50μm. A point force is applied to the hair tip and its angle with respect to hair-to-boss axis is varied while the volume change under the

parylene membrane is measured. This equivalently resembles the variation of flow angle. Boundary conditions and geometry of the model are the same as those of the model discussed in Section 4.4.1.1.

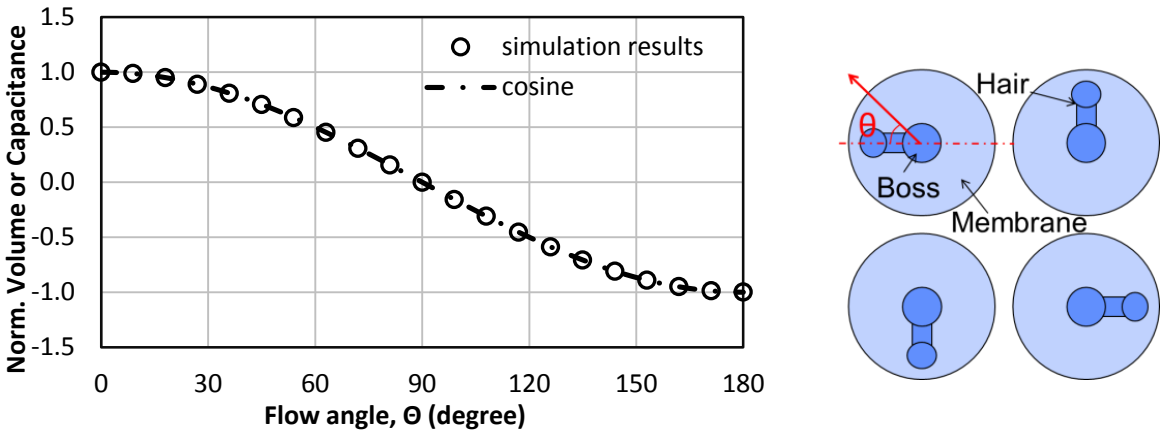

Figure 4.10 Simulation of volume change under a parylene membrane vs Θ. The y-axis is normalized and scaled for comparison. The figure on the right shows four HAFS from top, and definition of Θ.

The simulation results are shown in Figure 4.10. It is clear from the results that due to the intentional asymmetry of the hair-boss structure and its off-center position, each HAFS measures a projection of the airflow along its hair-to-boss axis. Therefore, if two HAFSs are perpendicularly positioned, the air flow direction in the wafer plane can be quantified. Two mirrored HAFS allow differential measurements to mitigate sensor response to inertial movement, temperature variations, or other common mode signals, which are critical for applications on mobile platforms. Consequently, by orienting four HAFSs as shown in Figure 4.10, a 2-D airflow vector can be measured differentially.

4.4.1.3 Range Calculation

Maximum measurement range of the sensors is set by the maximum stress on the front side membrane that does not exceed parylene yield strength. To calculate the stress level on the membrane, the drag force on the cilia, which is a function of fluid velocity, should be calculated.

This force also depends on hair geometry, fluid properties, velocity and distance from leading edge. The drag force modeling has been studied in different texts [22, 21, 49]. The model used in reference [21] is chosen herein. In this model, to obtain the drag force, a variable drag coefficient (C_D) is defined which itself is a function of Reynolds number and thus a function of flow speed. It is also assumed that the flow velocity (u_i) and therefore, piecewise drag force (F_{D_i}) is constant over the i^{th} infinite small piece (i^{th} out of n infinite small lengths) of the total hair length.

$$F_{D_i} \cong \frac{1}{2} C_D(u_i) \rho d {u_i}^2 \Delta h, \qquad \textit{Eq. 4.1}$$

$$lnC_D(u_i) \cong -0.67 lnRe(u_i) + 2.5, \qquad \textit{Eq. 4.2}$$

$$Re(u_i) = \frac{\rho u_i d}{\mu}, \qquad \textit{Eq. 4.3}$$

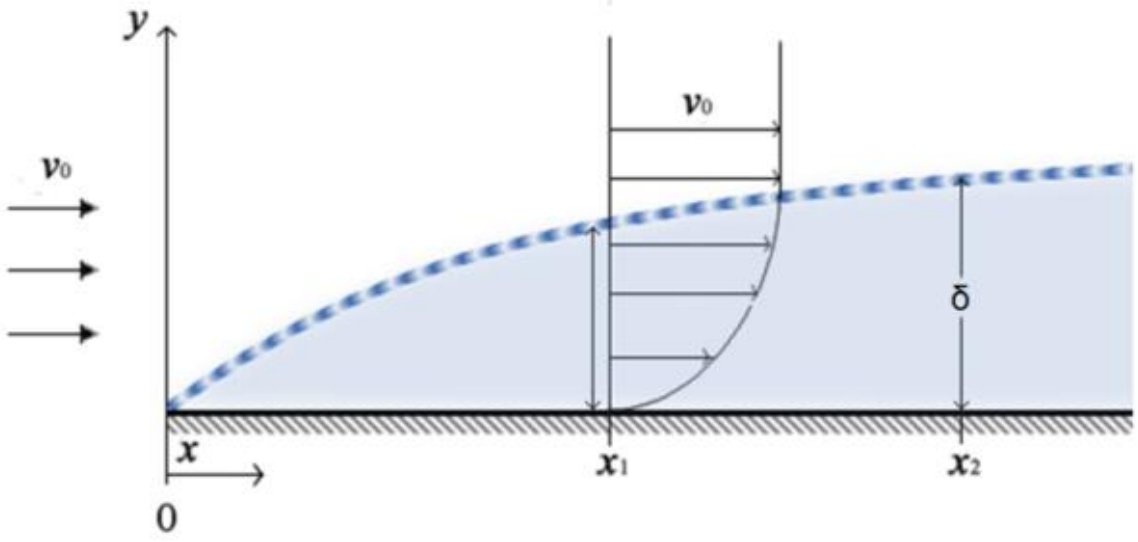

Figure 4.11 Schematic depiction of boundary layer, its thickness (δ_x), distance from the leading edge (x) and distribution of flow speed across the layer.

In these equations, ρ is the density of the fluid, d is the diameter of the hair and μ is the dynamic viscosity of the fluid. In this fashion, the variation of the flow velocity over the length

of the hair due to boundary layer formation is taken into consideration. The vertical distribution of velocity, $V_x(y)$, is a function of boundary layer thickness (δ_x) and velocity of the flow at infinitely far away from the surface of substrate (v_0). The boundary layer thickness (δ_x) related to distance from the leading edge (x) as shown in Eq. 4.4. Figure 4.11 shows the concept of boundary layer and schematic distribution of the flow speed in the boundary layer.

$$\frac{\delta_x}{x} = \frac{4.79}{\sqrt{x.Re}}, \qquad \textit{Eq. 4.4}$$

$$V_x(y) = v_0 Sin\left(\frac{\pi y}{2\delta_x}\right), \qquad \textit{Eq. 4.5}$$

To obtain the total drag force, an infinite small section of the hair over which the flow speed is constant is assumed. Therefore, the drag coefficient is constant, so, drag force acting on this infinite small section can be calculated using Eq. 4.1 when C_D and u_i are known. Once the F_{D_i} is found, with integration over the hair length, total drag force can be obtained. A numerical model is developed in Matlab to calculate the drag force acting on a hair with given dimensions.

Figure 4.12 shows three drag force estimation curves, each of which corresponds to a certain distance from the leading edge. The distance from the leading edge determines how deep the hairs are submerged into the boundary layer. The effect of boundary layer can be clearly seen in Figure 4.12 as the drag force is reduced when the distance from the leading edge is increased. The largest distance from the leading edge is equivalent to maximum drowning of the hair in the boundary layer. In addition, it is clear that as the hair submergence deepens into the boundary layer, the reduction in drag force over the hair length intensifies.

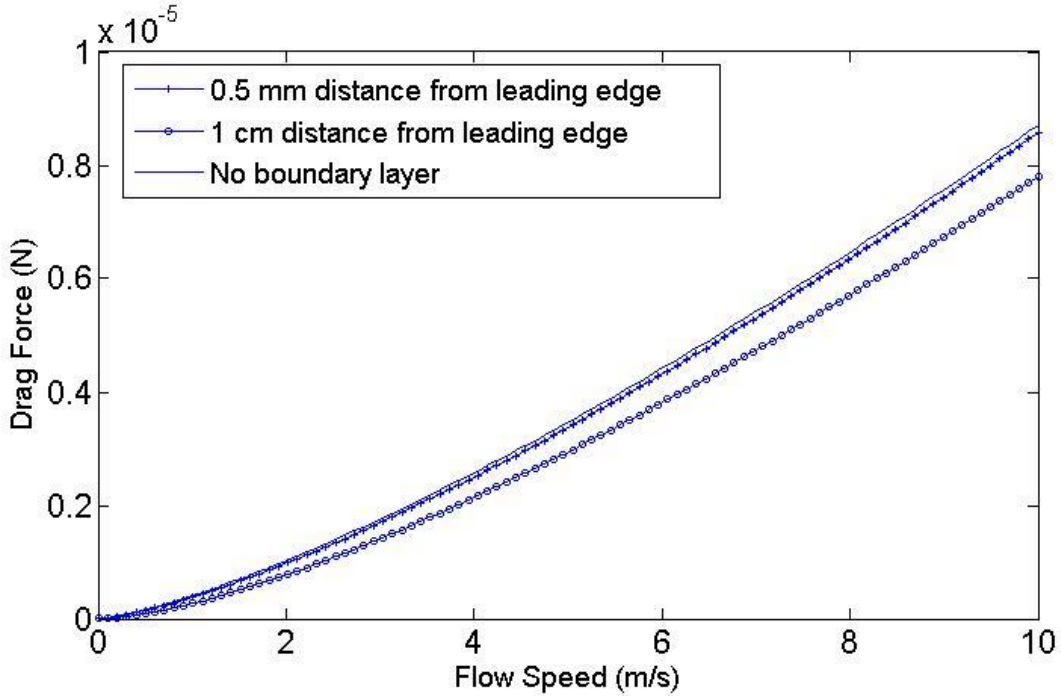

Figure 4.12 Drag force as a function of air flow speed. The nonlinearity of the drag force with respect to flow speed increases when the distance from the leading edge is increased.

Boundary layer submergence of the hair affects the drag force at low flow speeds more than at higher speeds. The calculation shows that the drag force decreases by 4 orders of magnitude at 0.1mm/s of flow speed when located 1 cm away from the leading edge, while at 10 m/s it is reduced only by less than 25%. Therefore, in designing the hairs, a higher hair length that can be extended out of the boundary layer is desired. The drag force equations and calculation methods in this section can be used to estimate the full-scale range of the HAFS.

Using the same 3D model made in COMSOL™ and described in Section 4.4.1.1, full-scale range of the HAFS can be calculated. To obtain the full-scale range, a point force is applied to the hair tip and von Mises stress on the parylene membrane is monitored. The point force is increased until the maximum stress exerted on the membrane reaches the parylene yield strength. This value is the maximum allowed drag force that can be tolerated by the HAFS, which sets the full-scale range. Since the relation between drag force and flow velocity is known, for the

maximum allowed drag force, corresponding flow velocity can be found. This velocity is the full-scale range of the micro-hydraulic HAFS. Although the micro-hydraulic HAFS can be theoretically operated up to this velocity, a precaution margin equal to at least 20% of the full scale range should be taken into account when operating the HAFS. Knowing the parylene yield strength is 59 MPa, the maximum measurement range of the HAFS can be estimated. In Table 4.6 calculation results depicting maximum flow velocity for EMH structures with various front side diameters are listed. For calculated results in this table, it is assumed the front to back surface area ratio of EMH is 5, thickness of parylene is 2 μm and the curvature radius of the backside electrode is about 25 mm. For maximum range, the maximum stress is set to 25 MPa and the corresponding flow is calculated.

Table 4.6 Calculated maximum measurement range of HAFS, along with base capacitance and deflection and capacitance change at 1 cm/s of air flow for various geometry of EMH structure.

Membrane diameter (μm)	Base cap. (pF)	Cap. change at 1 cm/s air flow (fF)	Top mem. defl. at 1 cm/s air flow (nm)	Max flow (m/s)
300	6.42	0.00431	0.545	80.3
400	7.44	0.0168	0.986	81.7
500	8.48	0.0420	1.41	75.3
600	9.58	0.0847	1.81	64.9
700	10.70	0.148	2.22	63.2
800	11.86	0.234	2.59	62.9
900	13.04	0.345	2.98	68.4
1000	14.26	0.486	3.39	70.6

4.4.1.4 Capacitance vs. Flow Speed Modeling

In the previous subsection, the relation between the drag force and flow velocity is studied. In order to obtain capacitance change in response to flow velocity on the top membrane, the base capacitance of the curved electrode structure is needed. Once the capacitance versus curvature is known, the curvature change of the curved electrode as a result of the volume displacement should be calculated. This curvature change will lead to the capacitance variations in response to

flow. Therefore, capacitance change versus flow velocity can be estimated. In Table 4.2 cross section of a radial curved electrode capacitance is schematically shown. Additionally, in this table, the volume under a spherical shell is calculated. The equations for the volume calculations are listed in inside the first row of Table 4.2. The volume under the shell can be approximated in case of $D \gg h$. By using equations listed in Table 4.2, when the volume under the shell increases as a result of fluid volume displacement, the curvature changes, thus, capacitance change can be estimated. The result of predicted capacitance change in response to 1 cm/s flow speed is listed in Table 4.6. Note that the shape of the shell is assumed to remain spherical when additional liquid is transferred to the bottom chamber. This assumption may not be accurate; therefore, this method is an approximation. It should be mentioned that due to complexity of drag force equations, a close form formulation for the air flow sensor gauge cannot be presented.

4.4.1.5 Hair Length and Diameter

Based on the results obtained from drag force calculations, the longer the hair, the greater the drag force. In addition, longer hairs will stand out of the boundary layer, thus are helpful to further increase the drag force. However, increasing the hair length results in bandwidth reduction since air damping significantly increases with hair length [49, 55]. Consequently, there should be a tradeoff between the length and bandwidth of hair sensors such that an optimum point based on a figure of merit can be achieved. However, in micro-hydraulic HAFS architecture, the factor that sets the overall frequency response of the HAFS, is the micro-hydraulic bandwidth, which is far below the hair bandwidth [55, 46]. On the other hand, there are some practical fabrication constraints. For instance, 10 mm long hairs cannot be securely affixed on a flexible membrane in a 50-100 μm footprint size. As a result, a hair length of 4-5 mm is chosen, which has proven to be practically feasible.

Diameter of the hairs also can increase the drag force. However, the relation is not linear. As shown in [55], for a hair with circular cross section the drag force increases with approximately the square root of the hair diameter. Another issue with the increased diameter of hairs is change of the flow regime from laminar to turbulent at lower flow velocities. This change to turbulence is not desired since it may cause difficulties in flow measurement. Nonetheless, fabrication limitations play an important role in determining the hair diameter. To test their mechanical stability, multiple hairs with diameters ranging from 100 μm to 350 μm and height of 4-5 mm have been fabricated with stereo-lithography technique. The results show that structures with diameters less than about 200 μm do not have mechanical strength to be used and integrated with the EMH. Should more advanced techniques become available, narrower hairs will be used. Additionally, in some instances, hairs with vane-like structures are fabricated (Figure 4.14). The vane with rectangular cross section increases the hair cross section in direction of the flow and reduces it in the perpendicular direction. This means by using the rectangular vane, drag force, thus sensitivity of HAFS, increases in flow direction, while drag and sensitivity are both reduced in perpendicular direction. Therefore, using vane-like hairs helps the directional sensitivity of the sensor.. However, vane-like hairs can cause flow detachment at lower velocities due to rectangular cross sections, therefore enter the HAFS into turbulent region of operation at lower velocities.

4.4.2 Fabrication

For the second-generation micro-hydraulic HAFS, the high-speed sloped-wall micro-hydraulic structure is used. This micro-hydraulic system is extensively described in Chapter 3 and references [45, 46].

4.4.2.1 SLA Fabrication

To fabricate hairs, a process that allows batch fabrication of three dimensional, tall structures with the ability to precisely position them over micro-hydraulic chip is needed. An auxiliary framework is used that holds the hair-boss in place, attached to a support rim, while it is being attached to the micro-hydraulic chip. By using extruded patterns on the rim and matching grooves on the EMH die, the framework can be mechanically aligned to the micro-hydraulic chip. The stereo-lithography technique can satisfy all the requirements; it provides a fast and low-cost method for making arrays of complex 3-D parts. It also allows for batch fabrication of hairs, with accurate control over hair-boss geometry, including various hair cross-sections/shapes and lengths. For example, flat, sail-like hairs result in larger drag force, therefore higher sensitivity for a given length can be achieved. To attach the hair-boss to the micro-hydraulic chip, epoxy can be applied either manually or by stamping to the bosses. Stamping will provide a more uniform layer of epoxy. Once the epoxy is applied, bosses are brought into contact with the EMH front side parylene membranes. Two types of epoxies have been used, Nu-Sil MED-4211 silicone elastomer and Loctite Hysol 1C^{TM}. After a few experiments, it was observed that Hysol 1C^{TM} provides a better bond between SLA parts and the parylene layer. It should be noted that due to the delicate and temperature-sensitive nature of these structures, the epoxy is cured overnight, at room temperature. Figure 4.13 schematically depicts the integration of SLA hairs with micro-hydraulic chip. It also shows a sample SLA framework, along with the integrated hair-boss, tethers, support rim and extrusions for mechanical alignment. After adhesion, the support tethers are cut, releasing the structures. The final micro-hydraulic HAFS is shown in Figure 4.14. Tethers can be cut either by a sharp precision knife or by a medical cautery. For minimal residues of tethers on the hairs, use of cautery is preferred.

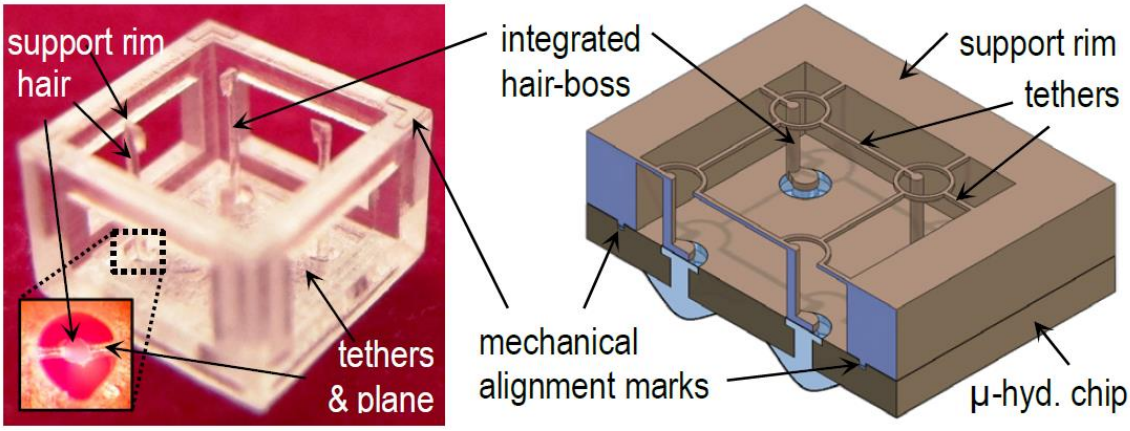

Figure 4.13 Right: schematic drawing of integrated hair-boss along with support rim and tethers (SLA framework) positioned on top of micro-hydraulic chip, Left: fabricated sample.

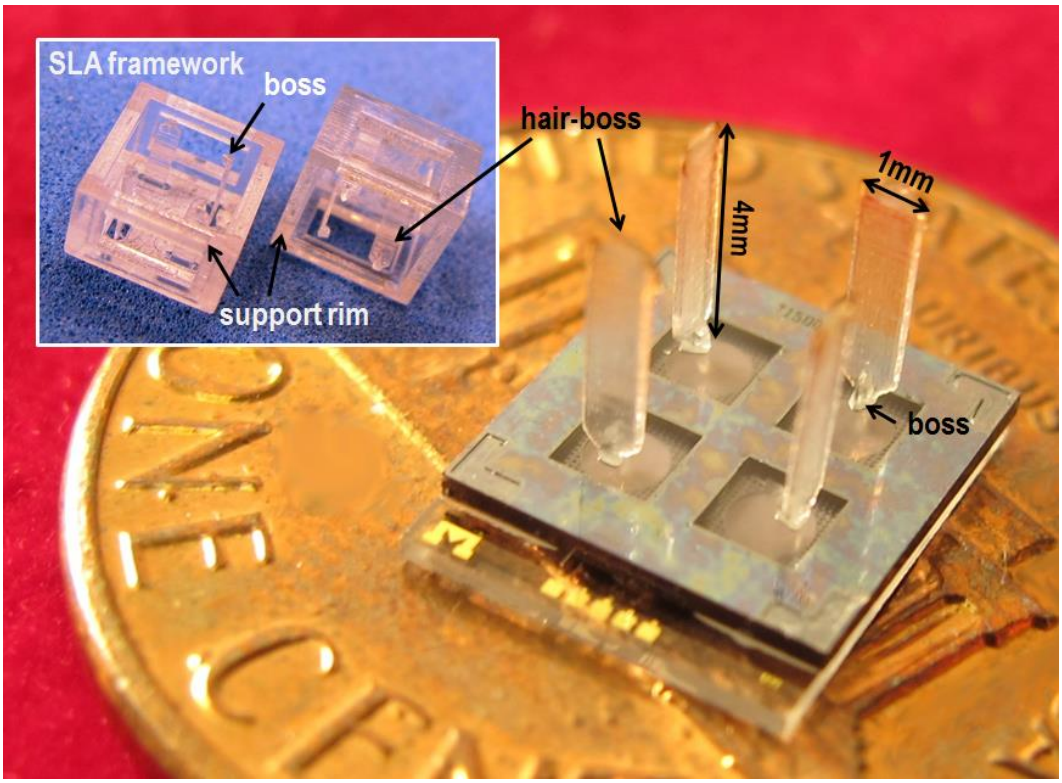

Figure 4.14 Second generation micro-hydraulic HAFS with SLA hair-boss attached with adhesive and SLA tethers trimmed/cut to release the hairs. The inset shows the fabricated SLA framework with hairs with rectangular cross-section (5:1 ratio).

4.4.2.2 Interface Circuitry

To measure the output capacitance of the HAFS, a PCB based on Analog Devices' 7745/7746 capacitance to digital convertor (CDC) is designed. This chip has a 24-bit Σ-Δ

module along with an integrated excitation signal generator that can digitize capacitance changes as small as 4aF at 90Hz update rate with an accuracy of 4fF [56]. An array of four sensors – two pairs, each pair for one direction – allows the extraction of the air flow direction. Therefore, to add directional sensing, one has to be able to convert capacitance of two differential pairs and use AD7746 in differential mode. Figure 4.15 shows a block diagram of the AD7746. Each pair of differential capacitance can be connected to EXCi and CINi(+) and CINi(-), where i=1,2.

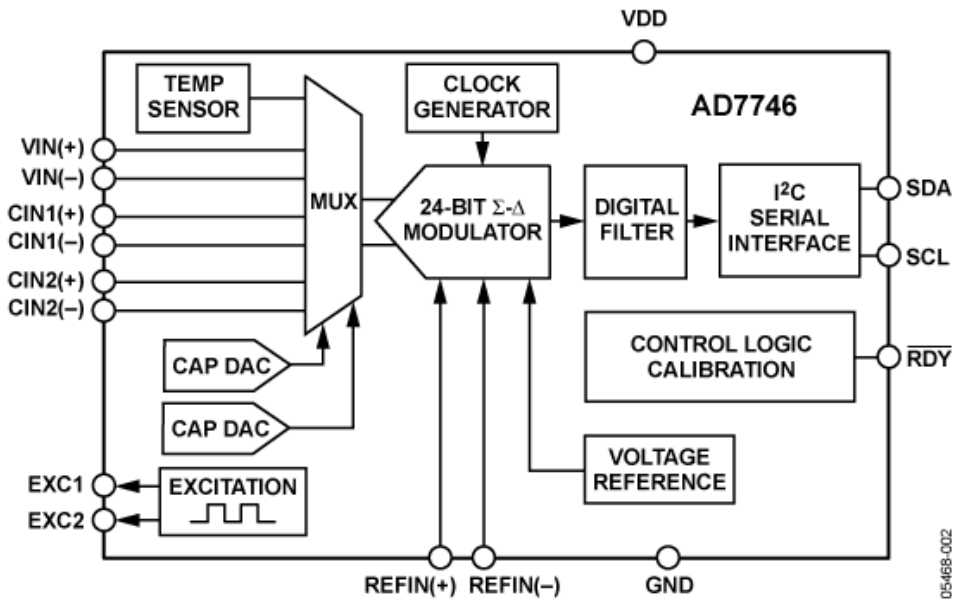

Figure 4.15 Block diagram of AD7746 [56].

The AD7746 has two input channels, each of which can take differential pair capacitance inputs. A mode selection capability has been added in design of PCB, i.e. to be able to switch between single-ended and differential modes by shunting designated pins on a header. With this shunt system, any of the four sensors can be selected for single ended reading. Both channel outputs are encoded into a single I^2C channel. The HAFS are attached to a separate daughter board that will be plugged to the main board. This separation is beneficial in many ways, such as flow shadowing avoidance by circuit components (due to elevation of the sensor) and the ability

for reusing sensor modules with other boards or boards with other sensors. Figure 4.16 shows fabricated circuit with and without sensor board mounted on it and Figure 4.17 shows a sample measurement of the sensor output when set on a lab bench and gusted with nitrogen gun or mechanically stimulated. To measure the circuit noise level at the output, the sensor is covered (quiescence condition) and output is measured to be less than 80 aF.

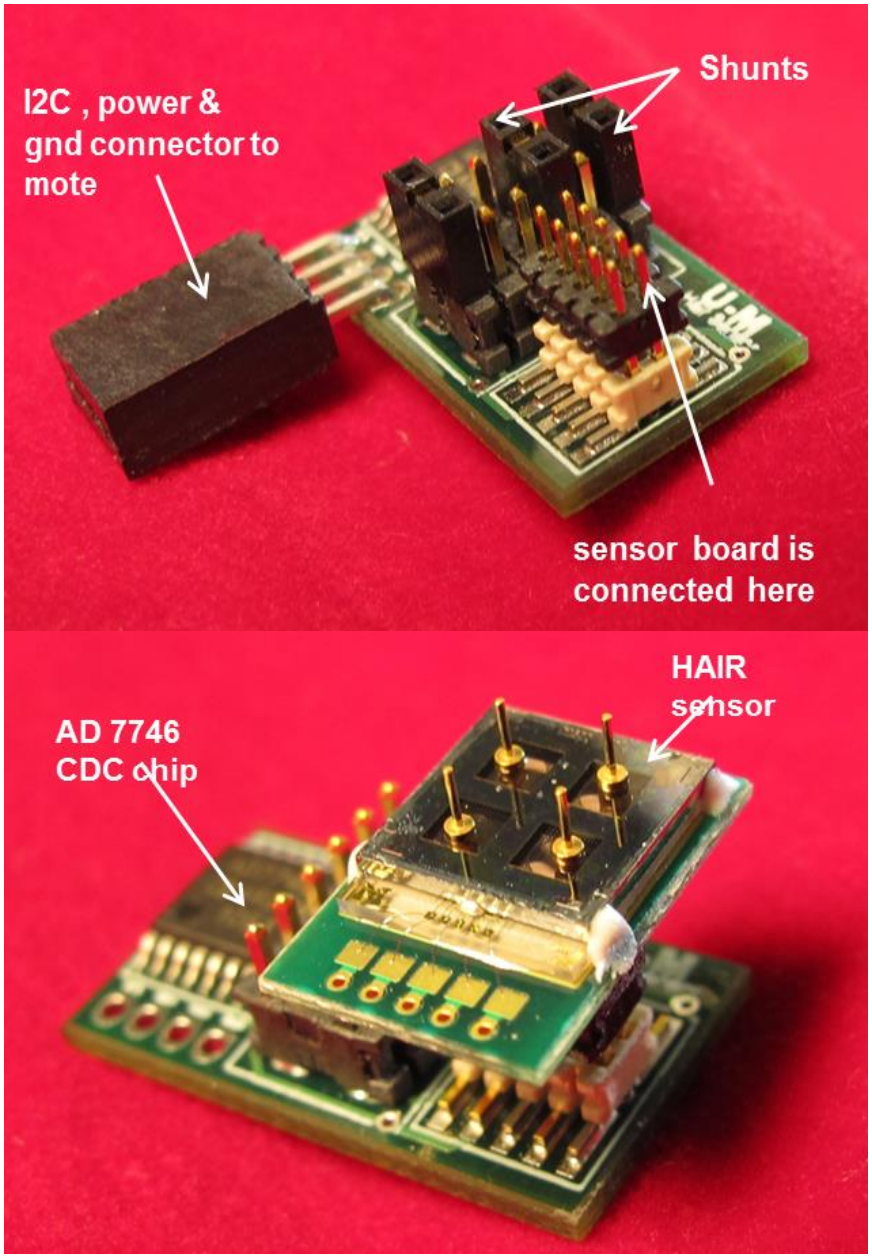

Figure 4.16 Top: Fabricated PCB for CDC interface circuit. Bottom: Sensor module mounted on the header. The sensor die is attached to PCB and wire-bonded to the board.

In order to read both CIN1 and CIN2, after each conversion, the channel is switched. This channel hopping adds significant amount of noise at the output, up to 10 fF. This happens due to unsettled value of CAPDAC (a capacitance value that is reduced from the input capacitance, to bring the base capacitance within the measurement window).

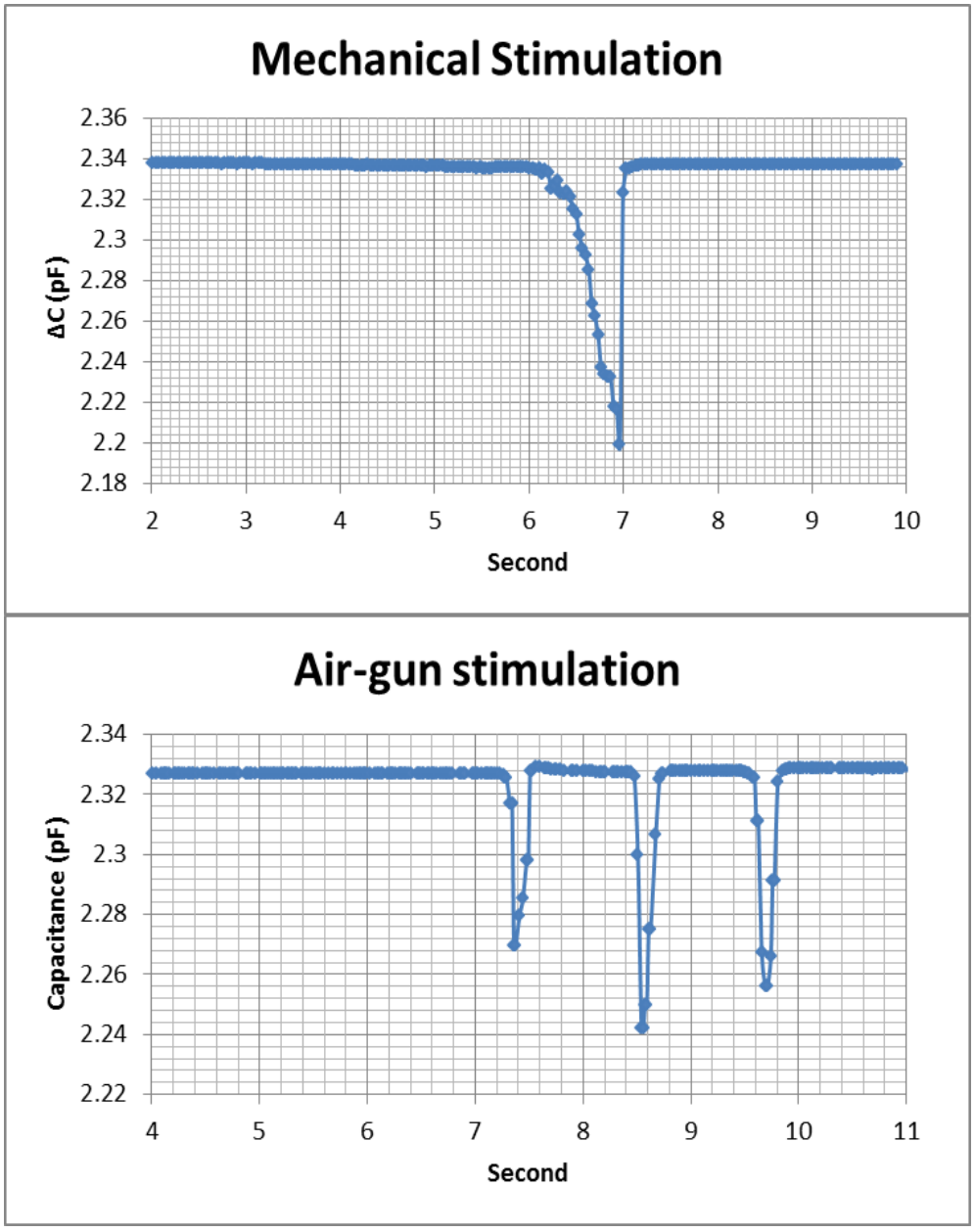

Figure 4.17 Top: Response of the sensor to a mechanical stimulation. Capacitance rise time (which corresponds to air flow reduction) is less than 30 msec. Capacitance fall time (indicating air flow increase) here is limited by the slow external mechanical stimulation. Bottom: Sensor response to fast air flow (air-gun) stimulation. Now the rise and fall times are equivalent.

To avoid increase in the noise level, the 7147 CDC chip from Analog Devices is used. This chip has 13 input channels with a 16-bit Σ-Δ module along with an integrated excitation signal generator that can digitize capacitance changes at maximum 90Hz update rate for each channel with sub-femto Farad accuracy [57]. The AD7147 has a multiplexer at the input that allows any combination of the input capacitances to be measured differentially or single ended. Figure 4.18 shows a sample measurement with this CDC chip. A printed circuit board is also designed for AD7147 with both daughter-main-boards and single board circuit. The first channel is output of two differentially connected HAFSs, and the second channel is a single ended measurement of one HAFS.

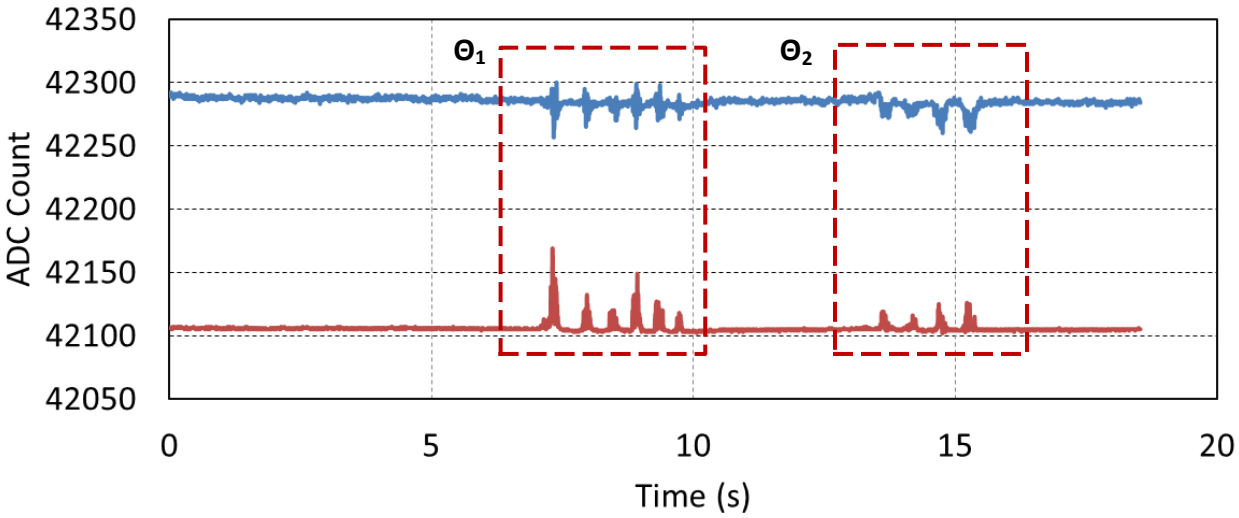

Figure 4.18 Sample measurement with AD7147. Two HAFS in X-axis are measured differentially (bottom data series, red) and Y-axis HAFS is measured in single ended mode (top data series, blue).

4.4.3 Experimental Results

4.4.3.1 Capacitance vs. Flow

To measure the capacitance change of the HAFS in response to flow velocity, the second-generation HAFS made with the sloped-wall EMH structure is tested in a wind-tunnel. In this test, the HAFS capacitance is measured as the flow speed is ramped up. For capacitance

measurement, the circuit described in Section 4.4.2.2 is used. The hair-to-boss axis of the sensor whose response is being monitored is aligned to the flow direction so that the projected flow on the hair is at its maximum value ($\Theta = 0$). These tests indicate that the HAFS has an almost linear capacitance change with air flow speed as shown in Figure 4.19. A full-scale range of greater than 15 $m.s^{-1}$ and maximum sensitivity of 47.9 $fF/m.s^{-1}$ are observed. This is more than ten times of previously reported sensitivity of 3.9 $fF/m.s^{-1}$ achieved using commercially available cylindrical pins that were manually attached as appendages [45]. It should be mentioned that 15 $m.s^{-1}$ is the flow speed limit of the wind tunnel. It may be possible to extend the linear response depicted in Figure 4.19 to a larger flow range.

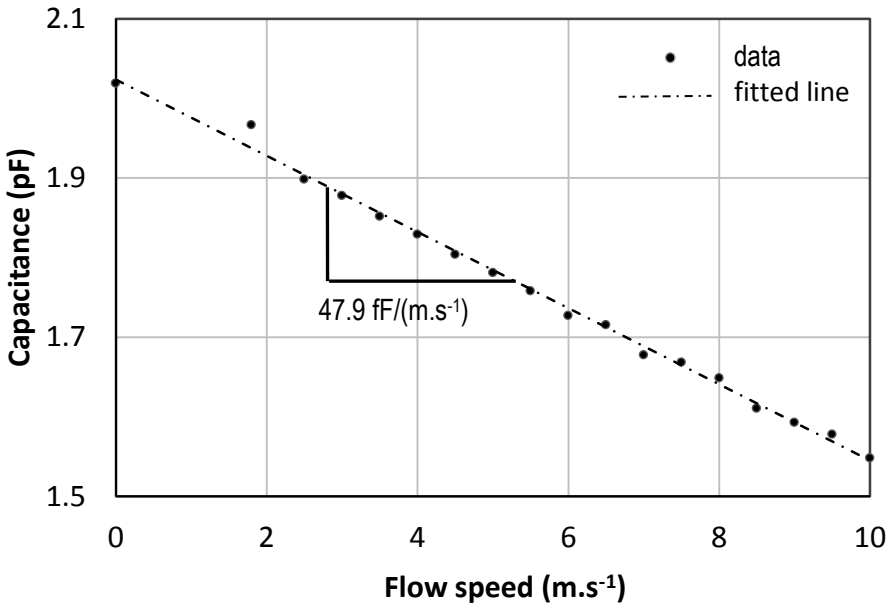

Figure 4.19 Capacitance vs. flow speed for a sample HAFS. Maximum full scale range of 15 $m.s^{-1}$(wind-tunnel limit) is observed.

Using previously developed circuitry with a minimum detectable capacitance change of 80 aF [45], the extrapolated minimum detectable flow speed is about 1.7 $mm.s^{-1}$. This means with the measurement range of 15 $m.s^{-1}$, the HAFS resolution is 1 part in about 8,800, which corresponds to about 78.9 dB of range to minimum detection ratio. In other words, the sensor

can effectively provide 13 bits of data. To the best of our knowledge, this the highest range to minimum detection (or range to resolution) ratio ever reported.

4.4.3.2 Directional Sensitivity and Angle Estimation

For characterization of the directional sensitivity, the HAFS is fixed on top of a rate table and is manually rotated while the hair sensor is fully immersed inside a constant speed laminar air flow. The normalized response of the sensor, which shows an angular resolution of 13°, is plotted in Figure 4.20 alongside simulation data. In this plot, simulation results refer to normalized volume change under the parylene membrane as the flow angle varies. The noise in the experimental data plotted in Figure 4.20 may be partially due to vibration or instability of the rotation stage.

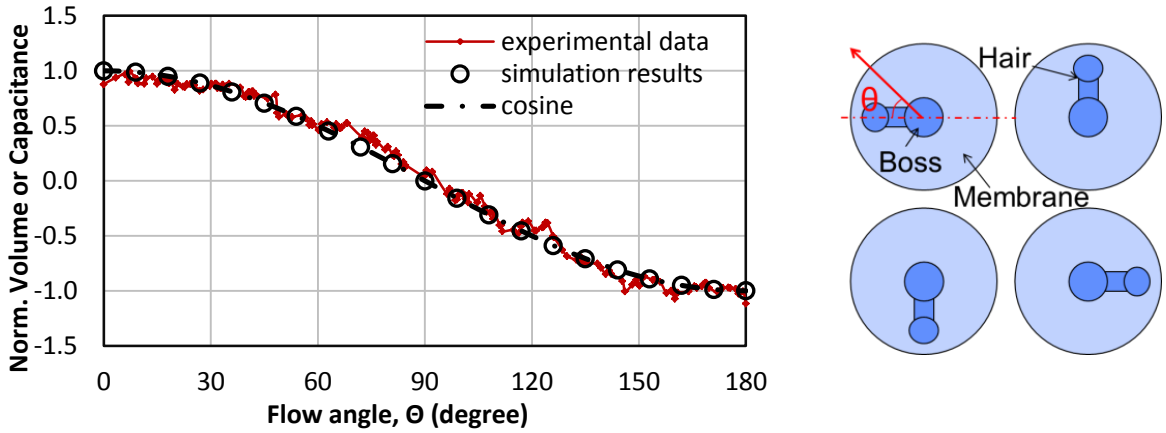

Figure 4.20 Volume change under a parylene membrane (simulation) or capacitance change (experiment) vs Θ. The y-axis is normalized and scaled for comparison. Noise in experimental data is partially due to inertial movement of the rotating stage. The figure on the right shows four HAFS from top, and definition of Θ.

In another experiment[2], two sets of differential cells of HAFS are mounted on a turntable in front of a boxed fan and based on the sensor output, the 2D vector of flow (amplitude and angle) is estimated. It is obvious that the 2D flow estimation is performed in the HAFS substrate plane.

[2] This experiment is performed in Autonomous Vehicle Laboratory, University of Maryland. The data is collected by Mr. Badri N. Ranganathan under supervision of Professor J. Sean Humbert.

The fan generates a rather turbulent flow, therefore, a constant flow velocity is not expected during the experiment. Figure 4.21 shows the sensor's output when the turntable is revolved 5 times and the both HAFS pairs are measured differentially. The turbulence in flow causes spikes in the sensor output. A digital band-pass filter to plot the data presented in Figure 4.21.A is used. Knowing each pair of HAFS measure the projection of flow vector, by using inverse tangent function, and cosine identity relation, both angle and amplitude of the flow vector can be estimated as shown in Figure 4.21-B and Figure 4.21-C. The phase shifts between each HAFS pair output might be due to physical misalignment of the pairs on the platform, i.e. their relative angle is physically less than 90°.

Table 4.7 summarizes performance of the 2-D HAFS made using SLA-fabricated hairs.

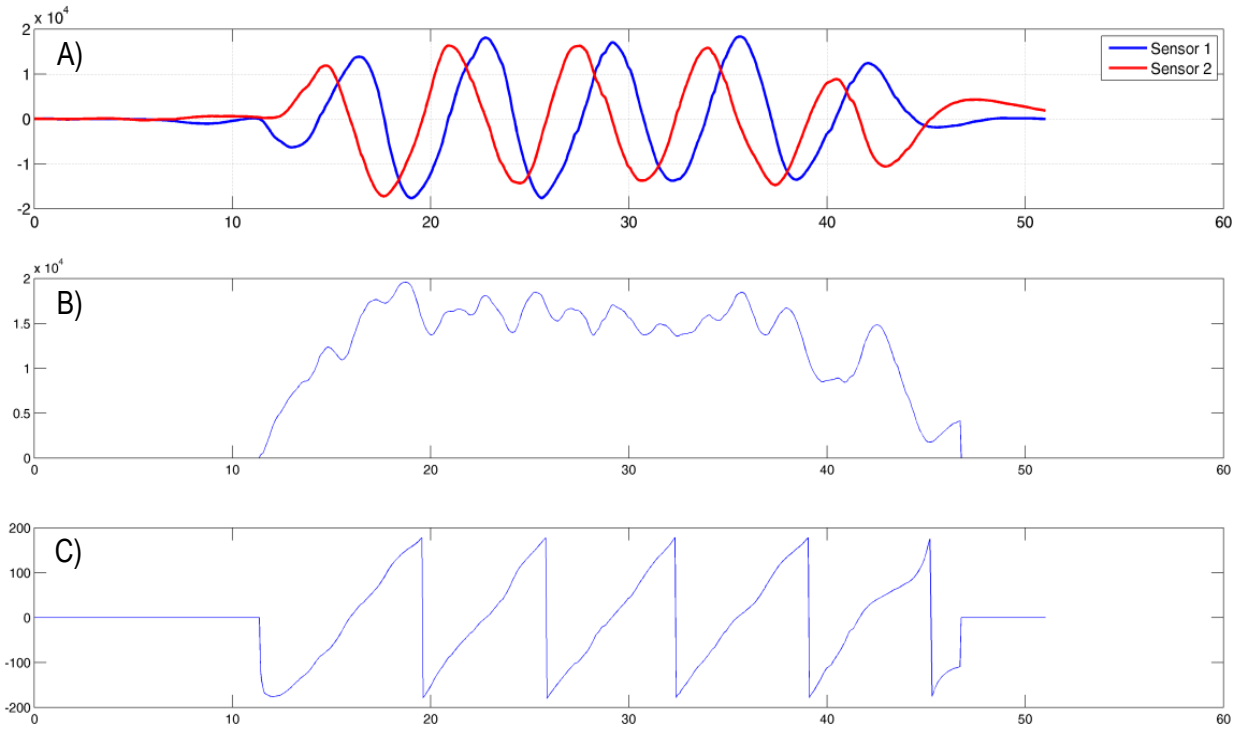

Figure 4.21 Angle estimation with an array of four HAFS.

Table 4.7 Summary of μ-hydraulic HAFS performance.

Supply voltage	3.3 - 5 V
Range	0 – 15< $m.s^{-1}$
Sensitivity	47.9 fF/($m.s^{-1}$)
Speed resolution	~1.7 $mm.s^{-1}$
Range/Resolution ratio	78.9 dB
Angular resolution	~13°
Spatial resolution	1-2.2 mm
Output	I^2C
Bandwidth	50-70 Hz
Power	3.5 mW
Weight (with ckt.)	1.2 - 1.5 g

4.5 Discussion

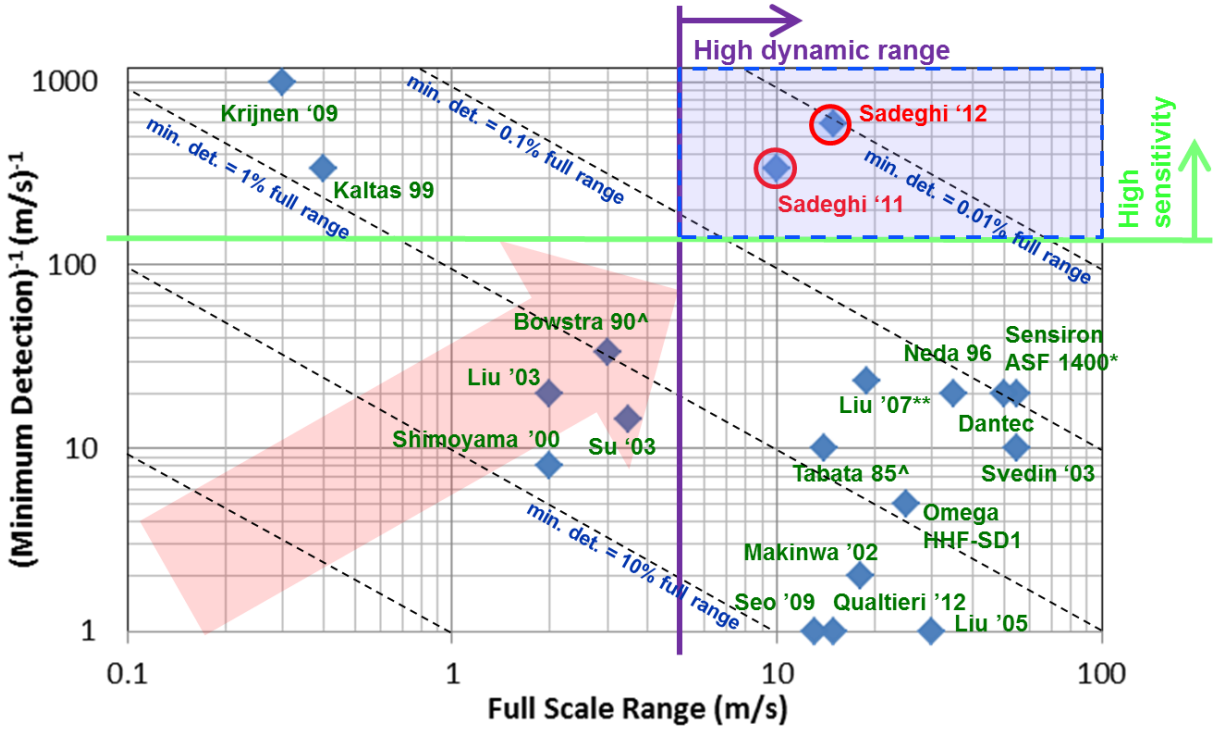

^ Minimum detection limits for data points that are not stated clearly are extracted from measurement graph data points, or assumed to be 0.01 of full-scale range or 10 cm/s.
* One of the finest commercially available Mass Flow Sensors (MFS), converted data from datasheet.
** The paper provides min. det. only for water flow. The equivalent min. det. in air is calculated to be 4.5 cm/s.

Figure 4.22 Comparison between range and minimum detection (resolution) of various flow sensors.

The HAFS presented in this paper can provide one of the largest full-scale to minimum detection ratios among reported sensors. In Figure 4.22, the minimum detection limit (i.e., resolution) and full-scale range of various flow sensors are compared. Top right corner of this

graph shows superior performance for flow sensors. This part of the graph contains sensors with large full-scale range and small minimum detection (or high resolution). From this figure, it is clear that the micro-hydraulic HAFS have the highest full-scale range to minimum detection ratio reported so far, to best of our knowledge. It should be mentioned that this feature is solely provided by utilizing the EMH structure as the sensing element. In this type of sensors, large sensitivity comes with the expense of reduced bandwidth due to using viscous fluid. Nonetheless, the measured bandwidth of about 60-65 Hz is quite acceptable for many applications.

4.5.1 HAFS Performance Improvement

Moving further toward the top right corner of Figure 4.22 needs improvements in both range and sensitivity. Based on theoretical calculations presented in Section 4.4.1.3, full-scale range of the sensors can be up to about 70 $m.s^{-1}$, the flow speed after which parylene starts to deform plastically. Another limiting factor for the range is the adhesion strength of hairs to parylene membrane. This bond may break before plastic deformation of parylene; therefore, the full-scale range is determined by either yield or adhesion strength, whichever comes first. The sensitivity of HAFS can also be improved through EMH sensing unit and hair-boss modifications. The EMH base capacitance can be increased by either gap reduction or use of higher permittivity liquid. Additionally, if the elastic modulus of the EMH membrane is reduced, the sensitivity will be increased, although, a more compliant membrane reduces the bandwidth. The hair length is very important for sensitivity; in fact, HAFS' sensitivity scales almost proportionately with hair length. Hair diameter, however, does not have significant effects on HAFS sensitivity, as it changes with the square root of the hair diameter, approximately. Calculations show that HAFS with sub-$mm.s^{-1}$ sensitivity can be realized.

4.5.2 Integration with CMOS

HAFS introduced in this dissertation, can be integrated with a distributed CMOS circuitry for interfacing and signal conditioning/processing. This distributed array of CMOS circuitry in adjacency of the sensing elements can increase efficacy of the sensor arrays by decentralizing computations over a network, i.e. by parallel processing. Additionally, a local circuitry for each sensing element further enhances sensing performance by bypassing many noise sources before affecting the signal. The introduced process for fabrication of the second-generation EMH involves one high-temperature step that prevents starting the EMH fabrication with a CMOS substrate. However, after deep boron doping and EDP etching steps, an ED-NMOS circuit can be fabricated for each EMH cell, to form the local circuitry on the same silicon wafer. Additionally, EMH fabrication may be started with a CMOS wafer, and the perforated electrode can be formed by a low temperature process (e.g. out of a thick electroplated metal), to avoid high temperature processes that affect the CMOS parts. Integration of HAFS and EMH with CMOS is subject to further investigation for future research projects.

4.5.3 Frequency Response

The characterization of the sloped-wall EMH structure shows a moderately high-speed sensing with 70 Hz bandwidth [46], as extensively described in Chapter 3. Measurement of the micro-hydraulic HAFS bandwidth is not practicalwith the same LDV method utilized for EMH bandwidth measurement, since the hairs are very fragile and cannot be touched by the piezo-electric beam. As mentioned in Section 4.4.1.5 of this chapter, the bandwidth of the hairs is mainly set by the EMH and the over-damping of system due to viscous fluid flow. Additionally, the only mechanism reducing the bandwidth is speculated to be the additional weight of hair-

boss. Therefore, knowing the hair-boss weight is negligible compared to the liquid weight used in EMH structure, the bandwidth of the HAFS is estimated to remain within 50-70Hz range.

4.5.4 Inertial Sensitivity/Differential Measurements

The micro-hydraulic HAFS presented in this work is expected to be sensitive to inertial forces since a considerable liquid mass and parylene membrane form a traditional spring-mass system, conventionally used for inertial sensing. This inertial sensitivity can be mitigated by using differential pairs in that a spatially mirrored set of HAFSs experience the same inertial forces, therefore cancel out inertial force signal if used in differential mode. However, responses to flow velocity will add up in differential mode due to mirrored positioning of the cells.

To characterize the inertial sensitivity of micro-hydraulic HAFS, a covered sensor is located on a shake-table and its output capacitance is measured. Knowing the frequency and amplitude of the shake-table, the acceleration can be obtained. The test is repeated to measure in plane and out of plane sensitivity of the micro-hydraulic HAFS by varying the orientation of the sensor. The preliminary characterization shows out of plane and in plane inertial sensitivity of HAFS are about 2.5 fF/g and 2 fF/g, respectively, as shown in Figure 4.23.

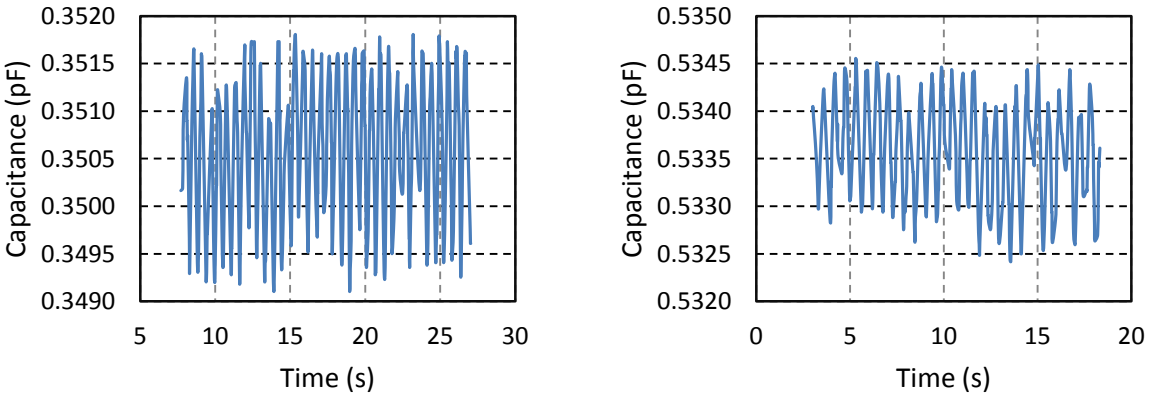

Figure 4.23 Inertial sensitivity measurements, with ±0.5g peak acceleration and frequency of 2Hz, on a shake-table. The left plot shows HAFS inertial sensitivity for vertical motion and the right one shows that of lateral.

4.5.5 Drift Due to Temperature

During experiments, it is observed that the HAFS' base capacitance drifts over time with a very large time constant. This variation can be seen even when the sensor is covered inside a package that isolates it from the background air flow inside the room. This low frequency capacitance drift is speculated to be due to ambient temperature fluctuation. Ambient temperature can effectively vary the dielectric constant of the silicone oil used to form EMH structure. It is clear that the variation of dielectric constant changes the base capacitance. The fluctuation is less than 0.1% of the base capacitance value. For instance, for an EMH with 12 pF base capacitance, the wavering is within about ±4 fF. The base capacitance drift can be effectively controlled once the two HAFSs are differentially measured.

4.5.6 Scaling Considerations

The HAFS presented in this chapter can be reduced in size; however, its performance might be compromised in some aspects. To increase spatial resolution for flow pattern monitoring, smaller HAFS are desired, which means smaller EMH and hair-boss structures should be used. The issues and challenges of EMH scaling are discussed in Chapter 3 of this dissertation. Assuming the EMH can be scaled down while maintaining its performance, change in the hair geometry affects the overall functionality of the HAFS as discussed in Section 4.5.1. Hair diameter can be reduced to accommodate for denser arrays, as the HAFS sensitivity changes approximately with the square root of the hair diameter. In terms of fabrication process, hair-boss with footprint size smaller than 50 μm does not seem to be practically feasible. Therefore, the parylene membrane of EMH should be at least about 200 μm (since the hair-to-boss arm is 50 μm, which occupies about 50% of the membrane radius), which results in the EMH footprint size of about 500 μm, assuming a typical hydraulic amplification of five. Thus, with this

reduction in overall HAFS size, the spatial resolution can be improved to 500 µm. Deep sub-millimeter spatial resolution does not seem to be practical with micro-hydraulic HAFS.

4.6 Conclusion

In this chapter, the concept of hair-like appendages being used in conjunction with micro-hydraulic structure to realize a high-performance air flow sensors is demonstrated. Two generations of HAFS are presented; the first generation is mainly a feasibility study and proof of concept for micro-hydraulic HAFS. For the second generation HAFS, both EMH and hair-boss structures are optimized to deliver a high performance air flow sensor. It utilizes an array of high-speed micro-hydraulic structures to realize a 2-D directional hair-like air flow sensor. An integrated hair-boss structure is introduced and optimized for high performance HAFS. Using the stereo-lithography technique, a fabrication method for precise positioning and simultaneous attachment of arrays of hair-boss structures is developed. The process could be extended to enable wafer-level integration. Fabricated devices have shown more than ten-fold increase in sensitivity over previous uni-directional sensors. An array of four HAFS allows for 2-D directional sensitivity with angular resolution of 13°. The second generation HAFS presented in this chapter have a wide dynamic range while maintaining high resolution. The experimental results show 78.9 dB of range to minimum detection ratio. This range to resolution ratio is one of the highest reported among all flow sensors. Additionally, extrapolated minimum detection of 1.7 $mm.s^{-1}$ of external DC air flow velocity, is the best ever reported.

5 Chapter 5: µ-Hydraulic Force Sensor Array

5.1 Introduction

Highly sensitive, highly dense force sensors are required for robotic tactile interface applications designed to mimic the capabilities of the human fingertip. Previous work has used various structures and mechanisms to achieve this goal. However, in these conventional sensors sensitivity is traded off with either density or range (Table 5.1). Force sensitivity vs. force range is plotted in Figure 5.1 for various published force sensors. Sensors closer to the top right corner have better performance.

Table 5.1 Summary of previously published force sensors

Ref.	Transduction method	Sensitivity	Density (cells/cm^2)	Range (mN)
Najafi et al. [58]	capacitive	27 fF/mN	400	10
Ko et al. [59]	CMOS- cap.	122 fF/mN	1600	0.517
Lee et al. [60]	capacitive	6 fF/mN	52.9	40
Lee et al. [61]	capacitive	6 fF/mN	25	10
Kim et al. [62]	resistive	2%/mN	28.6	600
Muhammad et al. [63]	capacitive	35 fF/mN	95	25
Takahashi et al. [64]	cap. µ-hyd	5 fF/mN	4	-
this work	cap. µ-hyd	260 fF/mN	100	10

In this chapter[3], a micro-hydraulic tactile sensor with the ability to maintain high sensitivity at reduced footprint size to realize an array of force sensors with capability resembling human fingertip touch sensing is introduced. This sensor utilizes an EMH structure as an enhanced sensing mechanism along with a tactile interface appendage fabricated with a low cost, fast prototyping stereo-lithography apparatus. EMH arrays with a minimum pitch size of 1 mm,

[3] The work presented in this chapter was partially done by Ms. Karen Dowling. Her contributions in COMSOL™ simulations, design and fabrication of SLA tactile interface is hereby acknowledged.

comparable to the spatial resolution to that of the human fingertip [65] has been successfully fabricated.

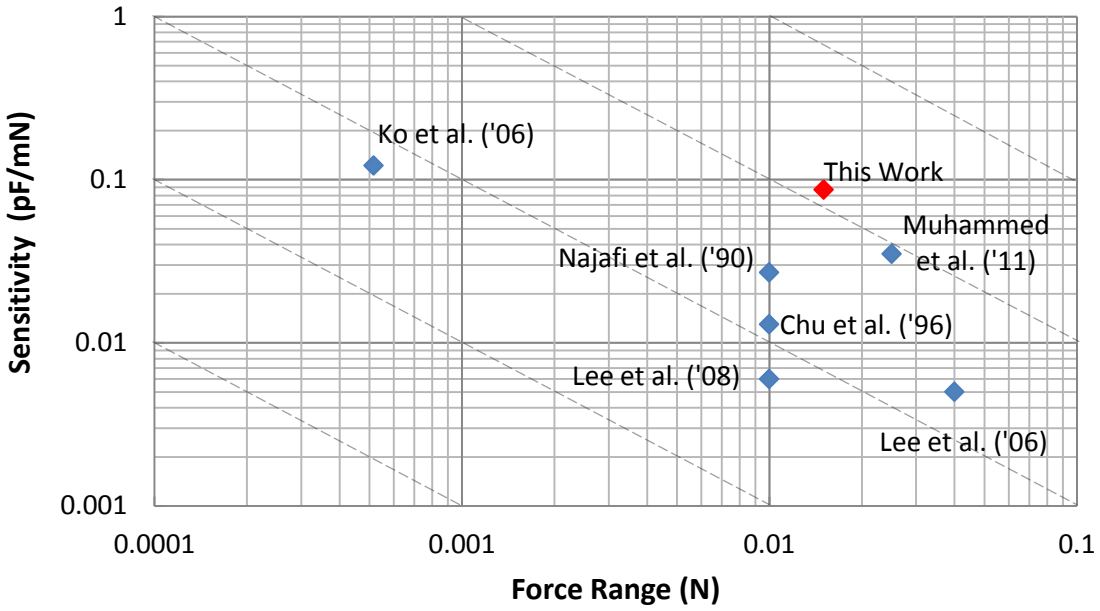

Figure 5.1 Force sensitivity vs. force range

The appendage specific to this force sensor application can be fabricated using a low cost stereo-lithography apparatus (SLA) [66]. The SLA machine used for this work is Viper SI2 (3D Systems, Inc.) [52], which operates based on laser-assisted polymerization of Accura® ClearVue polymer [53]. The SLA is capable of creating a dense array. The SLA technique can have resolution as high as 16 µm. However, based on performed characterization, the smallest structures that can be reliably made include 100 µm walls and 300 µm diameter holes with the minimum feature size of 50 µm. The SLA was chosen over other conventional fabrication methods for a few reasons. First, its resolution fits the dimensions needed for the purposes of this device. While here the device density is limited by the hydraulic fabrication method, the SLA allows for density up to 100 units/cm^2. Second, it is a very low cost method of fabrication for millimeter-sized parts in comparison to conventional micro-fabrication techniques. Finally,

the fabrication of complex three-dimensional (3-D) structures is simplified by SLA. Some of the 3-D structures with intertwined patterns are not even feasible to make using conventional micro-machining methods.

5.2 Design

5.2.1 Structure

Similar to HAFS sensor presented in Chapter 4, the application specific appendage has to convert the measurand into a pressure change applied to EMH structure. The tactile sensor consists of a plunge, which sits on the top parylene membrane of the EMH structure, inside a protective casing (a base and a cap), as schematically depicted in Figure 5.2. The micro-hydraulic system used for this sensor, is the high-speed sloped wall structure described in Chapter 3. A load on the plunge causes deflection in the top membrane and pushes the fluid to the lower membrane, which also deflects. The capacitance between the metal electrode on the bottom membrane and the conductive perforated membrane inside the bottom part of the micro-hydraulic chamber changes in response to the applied force. The tactile plunge is held in place by the casing, which protects the parylene membrane from deformation or rupture by limiting the vertical motion of the plunge to the allowed range of stress for parylene deflection. Each plunge has an individual isolated cavity, as shown in Figure 5.2, to eliminate cross talk.

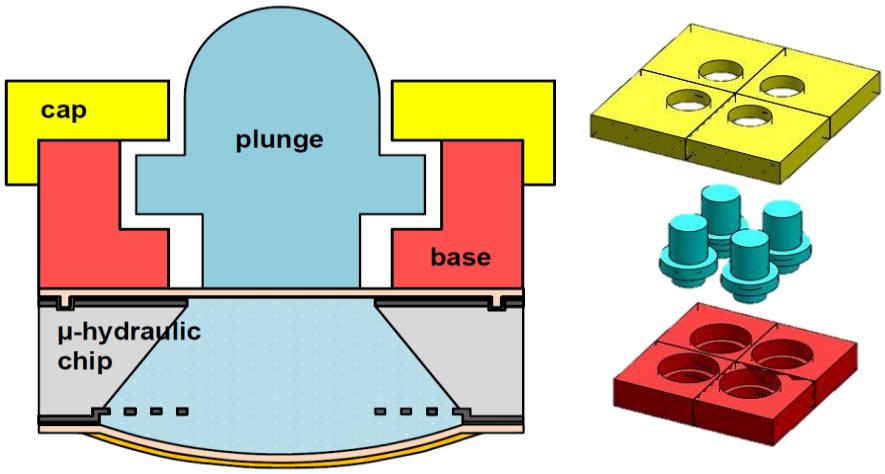

Figure 5.2 EMH structure along with tactile structure design (left) 3-D layout of tactile parts (right).

Multiple simulations are run to co-optimize the deflection range of the plunge on the top membrane, the contact area between the plunge and the membrane, and the thickness of the parylene membrane. The maximum stress on the membrane should be kept below the parylene yield strength of 59 MPa, while maximizing the force range. To do this, a 3-D COMSOL™ model is made that consists of a parylene membrane (Young's modulus: 3.25 GPa) and a rigid cylinder, representing the plunge, sitting on top of it. For the boundary conditions; parylene membrane around the perimeter is fixed and all other surfaces are free to move. Figure 5.3 shows the simulation setup and plotted von Mises stress and deflection with 40 mN force applied to the center of the plunge atop a 5-μm thick parylene membrane. A point force was used to apply force from 1-10 mN and 10-100mN using parametric sweeps. As long as the bending of the cylinder is ignorable compared to the parylene deflection, it can be assumed that the point force applied to the center can represent a pressure distribution on the plunge. The radius of the plunge and thickness of the top membrane were varied from 100 μm to 750 μm and 2 μm to 15 μm, respectively, to determine the optimal design.

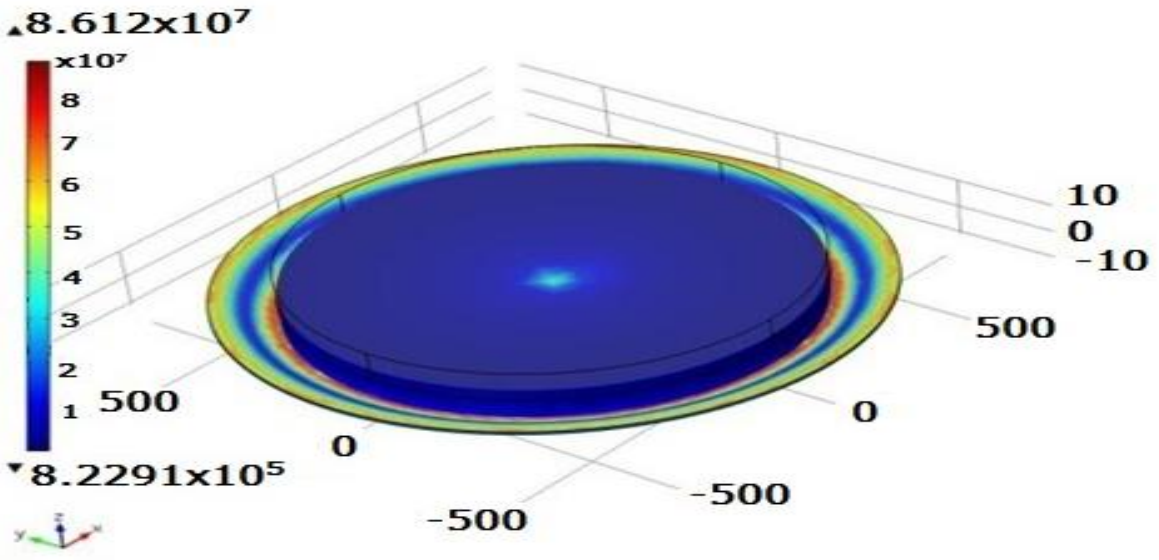

Figure 5.3 Simulation of parylene membrane stress with plunge deflection on surface, with membrane radius 750 µm, plunge radius 600 µm, point force from 0.001N to 0.01N, and 0.01N to 0.1N applied on center (40 mN here).

Based on calculation of von Mises stress in this simulation, the maximum measurable force and corresponding maximum deflection to keep the stress level below parylene's yield strength are obtained (Table 5.2).

Table 5.2 Simulation results for 600-µm button radius on 750-µm membrane radius.

Parylene thickness (µm)	15	10	5	2
Max force (mN)	180	100	20	5
Max tolerable deflection (µm)	24	24	20	29
Cap. change at 1mN (fF)	4.26	10.5	55.0	231

Additionally, the membrane deflection and associated capacitance change at 1 mN force applied (Table 5.2) have been calculated. Based on these results, it is decided to use a parylene thickness of 2 µm (to obtain high sensitivity) and a plunge contact radius of 600 µm. To increase the dynamic range, a thicker parylene may be used without affecting the design parameters for the tactile interface parts (i.e. the plunge and casing).

A test-to-failure on a 2-μm membrane was done to experimentally determine the maximum amount of deflection allowed. For a 2-μm thick membrane, deformation was found only after 100 μm deflection. The difference between this value and the maximum 29 μm deflection predicted in Table 5.2 is most likely due to the initially curved parylene membrane profile. The simulation assumed a flat membrane; however, the membrane is actually curved upward due to the liquid encapsulation method used. Given the larger deflection, it may be possible to obtain a force range 3× larger than that listed in Table 5.2.

5.3 Fabrication

5.3.1 Hydraulic Structure

For realization of tactile sensor, high-speed sloped-wall EMH structures with front side membrane diameter of 1.5 mm are used. The fabrication and features of this micro-hydraulic structure is extensively discussed in Chapter 3. The tactile interface is directly attached to the EMH structure. However, to cover a wider force measurement range, thicker parylene membrane could be utilized while other fabrication parameters are intact.

5.3.2 Tactile Interface

As mentioned above, SLA was used to fabricate the tactile interface parts that are appended to the micro-hydraulic sensing chip to form the force sensor array. Figure 5.4 and Figure 5.5 show the fabricated device and a cross section of tactile interface and assembly, respectively. The SLA tool has been used is the Viper SI2 (3D Systems, Inc.) [52], which operates based on laser-assisted polymerization of some specific resins. The material used for these parts is Accura® ClearVue polymer [53]. It should be mentioned that due to over-curing phenomenon observed in the stereo-lithography process, the designed and fabricated parts geometry do not closely match. The over-curing happens when adjacent laser pulse polymerizes the resin in the

areas that are not supposed to be solidified. For instance, after fabrication of a perforated structure, holes might turn out to be tighter than the original design, since when the laser scans around the perimeter of the whole, the resin inside the hole is partially cured. Some dimensions in the design, are critical and needed to be accurately fabricated (e.g. contact diameter of the plunge, and maximum vertical movement of the plunge). Therefore, SLA part fabrication has been iterated multiple times to closely calibrate critical dimensions in the fabricated parts by adjusted the original design.

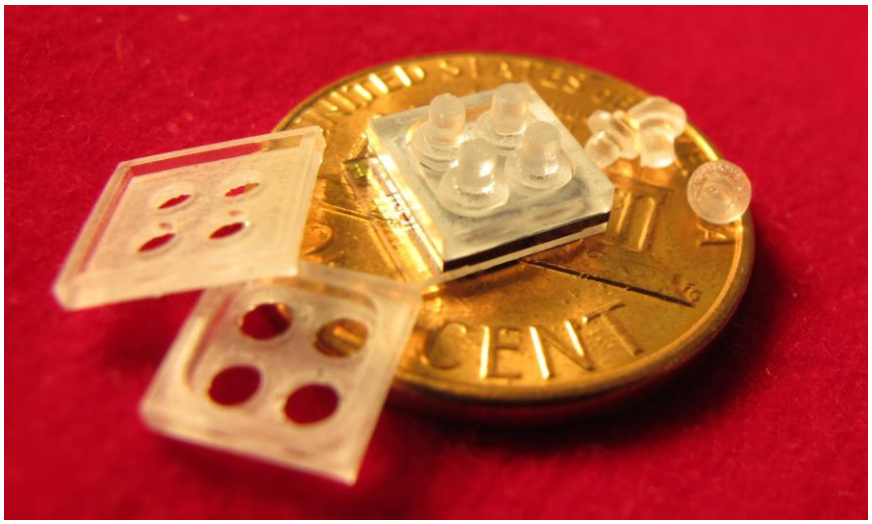

Figure 5.4 Sample μ-hydraulic tactile sensor (without cap), casing, and plunges.

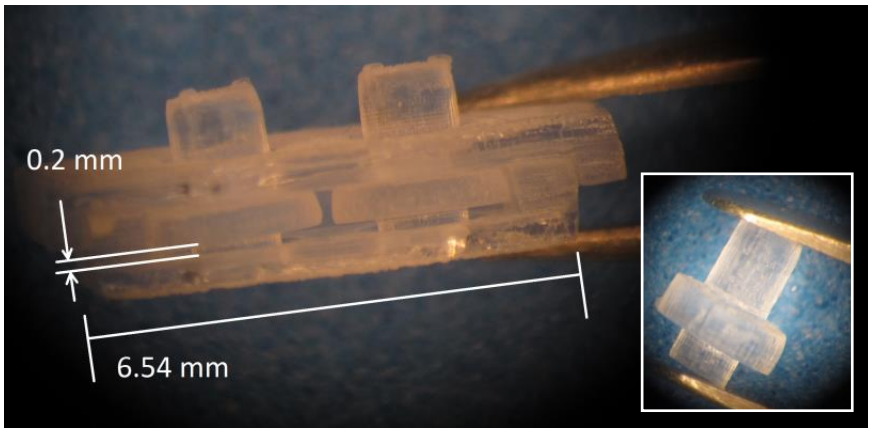

Figure 5.5 Tactile interface, cross section view of deflection space and plunge.

5.4 Experimental Results

5.4.1 Force Tests

To characterize the response of the sensor to force, the device was tested by applying variable loads using milligram-sized weights while the capacitance was measured. The sensor was wire bonded to a PCB designed for interfacing with Analog Devices' AD 7746 capacitance to digital convertor (CDC) chip [56]. The CDC chip is capable of detection of 4 aF capacitance change with maximum base capacitance of 21 pF. This circuit is the same as that used for HAFS measurement described in Chapter 4, by which a minimum detectable capacitance change of 80 aF at quiescence was measured. Figure 5.6 shows the capacitance change vs. force for some devices tested.

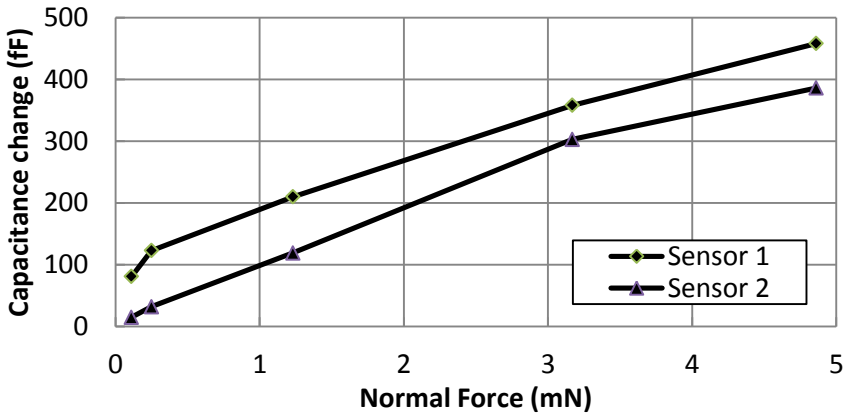

Figure 5.6 Capacitance vs. force for two tactile sensor samples.

The average measured sensitivity is 87 fF/mN and the maximum is 260 fF/mN. This variation is most probably due to misalignment of the casing with the hydraulic chip, which causes off-center positioning of the plunge. The off-center located plunge reduces the deflection of front side and therefore lowers overall sensitivity.

5.4.2 Cross Talk

In order to measure cross talk, a load is applied to a sensor besides the one being measured, and the change in sensor capacitance is monitored. Figure 5.7 plots a cross talk measurement for a micro-hydraulic force sensor array with separated plunges. No cross-talk is observed.

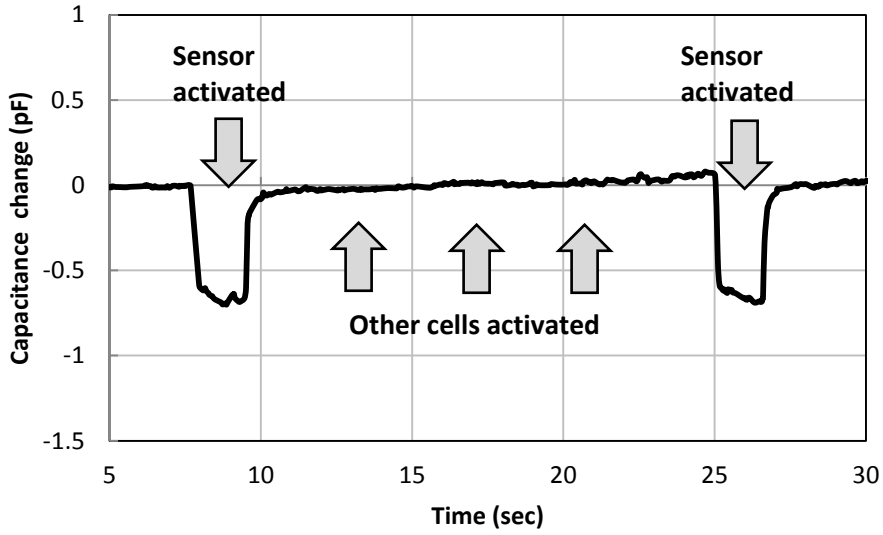

Figure 5.7 Cross talk demonstration of tactile sensor. No cross talk is observed between cells.

To compare with typical architectures for force sensor arrays, an alternate design is considered where an elastomeric sheet that covers the hydraulic structure replaces the plunge and casing. This configuration also provides the needed protection for the membrane. However, the plunge structure is expected to be superior to an elastomeric sheet design due to its abilities to reduce cross talk between sensing cells and to maintain sensitivity. In contrast, a protective elastomeric sheet inherently causes cross talk and reduces sensitivity due to stiffening of the top side micro-hydraulic flexible membrane. To compare the plunge structure to an elastomeric one, a set of hydraulic cells was covered with a 0.85 mm thick sheet of PDMS and tested similarly. The test results suggest that the 0.85mm PDMS sheet demonstrates up to 25% cross talk and a 10× decrease in sensitivity. Figure 5.8 shows the test results with PDMS sheet.

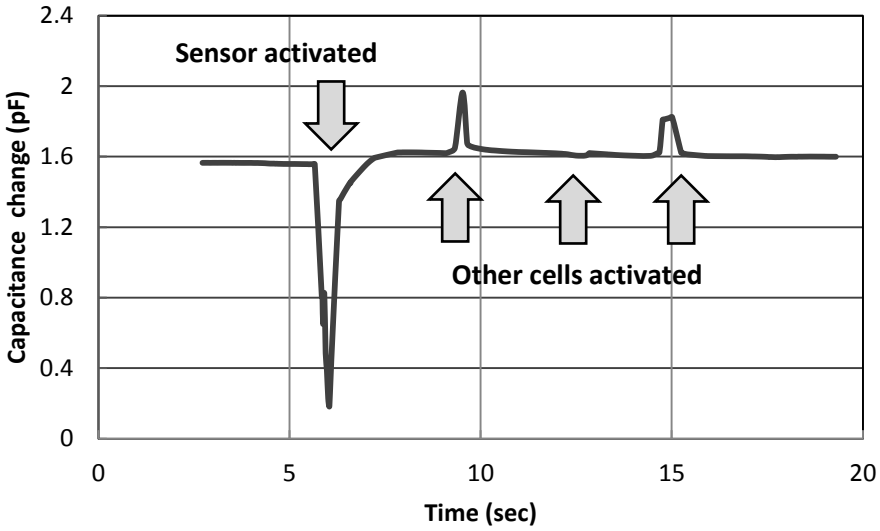

Figure 5.8 Cross talk demonstration of tactile sensor. No cross talk is observed between cells.

5.5 Discussion

These results open up several possible paths for future research in this field. First of all, this work focused on using rigid plunges. With the SLA and other fast prototyping techniques, rubber plunges/buttons can also be used to increase the force range of the sensor, because a softer material can deform to distribute force more evenly on the membrane. This will result in reduced stress level around the contact perimeter at which maximum stress occurs, thus increasing the full-scale force range. Second, different dimensions could be explored. Dimensions were chosen to simultaneously achieve a moderate amount of force and sensitivity range; however, different dimensions could be chosen to achieve other performance specifications. For example, a very highly sensitive sensor could be made with limited force range, or a sensor with large dynamic range could have reduced sensitivity. Similarly, various membrane thicknesses could be tried.

EMH structures can be utilized to realize high-density array of tactile sensors to resemble human fingertip. For this purpose, pins could be used instead of plunge-like structures, where

deflection is limited by the excess height of the pin compared to the casing. Dimensions of both tactile interface and EMH structure could also be revised to increase the density of sensing units. As a demonstration of SLA capability for realization of dense arrays, Figure 5.9 shows an array of 17×17 pins made with SLA Viper SI2 and Accura® ClearVue polymer. The array area occupies slightly less than 1 cm^2. The array is fabricated on a polymer substrate, shown with and without protective casing (colored in red for better visibility). In the present design, the smallest micro-hydraulic sensing unit occupies an area of about 0.79 mm^2, which allows for spatial resolution of slightly less than 1 mm^2. Combining the a large array of EMH sensing units with high density pin-casing tactile interface, a low power, high accuracy tactile sensor arrays with spatial resolution better than that of human fingertip can be realized.

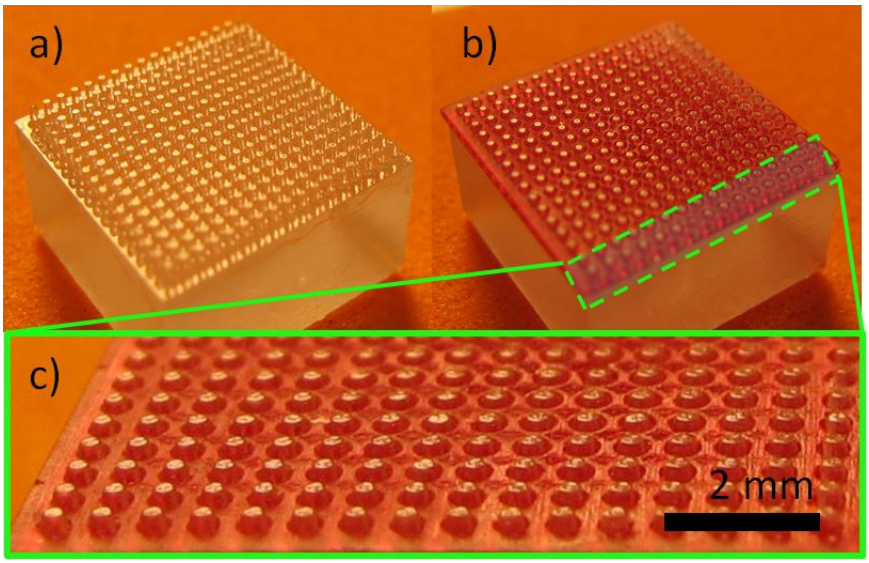

Figure 5.9 A prototype dense array of pins that can be used to make a skin-like force sensor array: a) pin arrays; b) pin arrays with casing (red translucent part); and c) close view of pins passed through the casing to show the protection mechanism.

The EMH structure capability to be used in actuation mode allows object identification and force sensing to be performed simultaneously using the same sensing platform. This feature is uniquely provided by utilization of micro-hydraulic structure. For object or terrain identification, one should probe the stiffness of the material in contact with the sensor. To quantify the

stiffness, the plunge (or pin) can be electrostatically actuated and pushed toward the object, while its deflection being measured. The applied force to deformation ratio gives the modulus of the material, therefore its stiffness. For instance, a tactile sensor integrated with a robot can be used to distinguish the terrain texture on which it is deployed; mud, hard rocks, sands, etc. The object identifier tactile sensors can be used for medical applications where the physician cannot directly touch a tissue for examination. For example, the device can be embedded with an endoscope probe to sense and identify an object inside patient stomach.

5.6 Conclusion

In this chapter, utilization of the EMH structure for realization of another high performance sensor is demonstrated. The EMH core sensing unit is critical for high-accuracy tactile sensors in that it can increase accuracy at maintained measurement range. Here a micro hydraulic force sensor with average sensitivity of 87 fF/mN (maximum observed: 260 fF/mN) and potential to minimize pixel size to 0.79 mm^2, with a full-scale range of 10 mN is successfully created. The full-scale range can be increased up to 180 mN without a change in geometry, but increasing the parylene layer thickness. In addition, capabilities of SLA to be used for a high-density tactile sensor array at low cost are demonstrated. Moreover, the sensor architecture along with the micro-hydraulic design provides completely isolated pixels for minimized cross talk between adjacent cells. This force sensor shows promise for skin-like sensing applications. Compared to other works, it shows higher sensitivity (up to 0.260 pF/mN) with a potential spatial resolution of 1 mm. It is sensitive enough to detect the fall of a 38.5 nL water droplet. Furthermore, this plunge-membrane architecture can be used in actuation applications. For example, the pin can be electrostatically actuated outward; to characterize a surface being probed, or can be used as a miniature piston for air-foil control.

6 Chapter 6: Conclusion and Future Works

In this dissertation electrostatic micro-hydraulic (EMH) systems as a novel sensing/actuation element that can be used in combination with application specific appendages (such as bio-mimetic hair structures) to realize high performance MEMS sensors and actuators is introduced. The proof of concept EMH structure is fabricated, tested, analyzed and optimized. The optimized EMH structures along with two different application specific appendages have been used to demonstrate two instances of high performance MEMS devices; hair-like air flow sensors and array of force (tactile) sensors.

6.1 Summary of Achievements

For the first time, the concept of integrated electrostatic actuation with micro-hydraulic structure is demonstrated in electrostatic micro-hydraulic structures. For making EMH structures, a high-yield, double-sided wafer-level fabrication method has been developed. This technique can also be used for MEMS applications where bubble-free liquid encapsulation is desired. The EMH devices can be exploited for high-performance sensing and actuation. Specifically, EMH actuators have been successfully demonstrated that take advantage of both electrostatic actuation and hydraulic amplification to provide high force and large out of plane deflection. EMH actuators are the first micro-hydraulic actuators with an integrated source of drive force. With these devices, generation of forces on the order of 50 mN should be achievable with a cell diameter of slightly more than 2 mm. This micro-hydraulic actuator structure is likely to be used for a variety of applications such as valves for fluidic circuits, or as the base structure for micro-scale locomotion implementation or actuatable appendages.

The dynamic performance of the proof of concept straight-wall EMH structure has been analyzed. Based on this analysis, the dominant parameters in time domain behavior of the EMH structures has been identified to optimally design the next generation sloped-wall EMH systems. The optimized micro-hydraulic structure is well suited for high performance sensing applications where wide dynamic range and high resolution are needed in a low power system. The fabricated devices have shown bandwidth of 50-70 Hz in sensing mode.

For the first time, the idea of hair-like appendages being used in conjunction with EMH structure to realize a novel high-performance air flow sensors is demonstrated. Two generations of the micro-hydraulic hair-like air flow sensors (HAFS) have been successfully fabricated and tested. HAFS offer a large measurement range while maintaining high sensitivity. An integrated hair-boss structure is introduced and optimized for high performance micro-hydraulic HAFS. Using stereo-lithography technique, a fabrication method for precise positioning and simultaneous attachment of arrays of hair-boss structures has been developed. An array of four HAFS allows for 2-D directional sensitivity with minimum angular resolution of 13°. The second generation HAFS presented in this dissertation has a wide dynamic range while maintaining high resolution. The experimental results show 78.9 dB of range to minimum detection ratio. This range to resolution ratio is one of the highest reported among all flow sensors. Additionally, extrapolated minimum detection of 1.7 mm s^{-1} of external DC air flow velocity, is the lowest minimum detection ever reported.

EMH sensing platforms are also used to realize another high-performance sensor. The successfully fabricated micro hydraulic force sensor exhibited average sensitivity of 87 fF/mN (maximum observed: 260 fF/mN) and potential to minimize pixel size to 0.79 mm^2, with a full-scale range of 10 mN. The full-scale range can be increased up to 180 mN without a change in

geometry, but increasing the parylene layer thickness. Moreover, the tactile interface - made with low cost SLA technique - along with the micro-hydraulic design provides completely isolated pixels for minimized cross talk between adjacent cells. This force sensor shows promise for skin-like sensing applications.

Table 7.1 summarizes the aforementioned achievements.

Table 6.1 Summary of the achievements reported in this thesis

Tasks	Contributions	Pub.
Wafer-level liquid encapsulation (2008-2009)	1st double sided wafer level liquid encapsulation technique 1st long lasting double sided liquid packaging technique High yield, reliable, repeatable fabrication technique	[67]
µ-hydraulic system (2009-2010)	1st µ-hydraulic system with individual actuation/sensing chambers 1st successful integration of electrostatic components with µ-hydraulics Low power, large stroke out of plane µ-hydraulic actuator	[67]
Hair-like hotwire flow sensors (2009-2010)	1st time using of bond-wires for flow sensing Monolithic integration with CMOS circuitry Very low cost method for hotwire anemometer fabrication	[54, 68]
1st generation HAFS (2010)	1st functioning µ-hydraulic based hair-like air flow sensor 1st successful functionalization µ-hydraulic system for sensing Low power air flow sensor	[50]
µ-hydraulic design optimization (2011-2012)	1st study on dynamics of multi-dimensional µ-hydraulics Time response reduction by 400× Fastest electrostatic µ-hydraulic system	[69, 46]
µ-hydraulic force sensors (2012)	Nearly zero cross-talk tactile sensors array Large measurement range Low power force sensor Promising for skin-like applications	[70]
2nd generation HAFS (2012-2013)	Lowest minimum detection for external DC airflow sensing Highest maximum range to resolution ratio Low-power, robust, stand-alone operation Directional airflow sensing	[69, 51]

6.2 Future Works

Bandwidth, base capacitance and footprint size of EMH structures can be enhanced. To broaden the applications of EMH sensing/actuation platform, the bandwidth can be increased by utilizing lower viscosity materials. As shown in Chapter 3, lower viscosity fluids can

significantly affect the time domain behavior of the micro-hydraulic structures. For instance water can reduce the response time of straight-wall EMH by approximately 100×. Increasing the base capacitance of EMH can help both sensing and actuation mechanism. In the sensing mode of EMH, it increases the sensitivity and in actuation mode, it will generate larger force for a given applied voltage. To increase the base capacitance, fluids with higher permittivity (e.g. water) can be used or nano-particles with electrical dipoles can be added to the low-k fluids (fluids with low permittivity) to increase the overall permittivity. Although some of the EMH devices presented in this dissertation have footprint smaller than 1 mm^2, EMH cells can be scaled down by a factor of 2 or 3 while maintaining other aspects of the devices. This scaling increases the hydraulic resistance and lowers the capacitance. The former deteriorates bandwidth and the latter lowers the sensitivity. By exploiting bandwidth and capacitance increasing with abovementioned methods, the losses due to scaling can be compensated. Therefore formation of denser arrays of EMH structures and eventually EMH sensors/actuators will be feasible.

EMH fabrication process may be revisited to address some of the critical steps. In the current fabrication process, liquid is dispensed manually, which is a series process. This results in variations over the samples and slows the fabrication run. Auxiliary fixtures may be designed to allow for die-level or potentially wafer-level liquid dispensing. If realized, this fixture would help to reduce the capacitive gap of the EMH to improve sensitivity.

For applications in which EMH sensors are deployed in harsh environments, averaging is essential to obtain low noise measurements. Examples of such include integration of HAFS with micro-air vehicles (MAVs) where the sensors experience significant inertial, electromagnetic and background flow noises. By averaging, however, the measurand signal can be effectively separated from the noise. In order to embed multiple sensors, EMH structures with small

footprint sizes are yearned for. Additionally, with abundant number of sensors, reference cells can be defined to alleviate effect of other physical parameters on measurement. For instance, in MAV application, one covered HAFS experiences the same temperature variations, electromagnetic induction and inertial force noises. Hence, its output can be subtracted from uncovered cells to extract the flow velocity signal.

EMH based sensors presented in this dissertation can be improved. Hair-like appendages can be revisited to enhance performance of HAFS. Although larger hair diameters can increase fluid drag force, therefore sensitivity, they result in change of fluidic regime from laminar to turbulent at smaller flow velocities. Utilizing multiple extremely narrow hairs (e.g. hairs made of carbon fibers) instead of one hair can address this issue. In this scenario, while each hair provides lower drag, once bundled, the overall drag force converted to hydraulic pressure is multiplied. Hairs with various cross sections and geometries may also be used for HAFS improvements. For force sensors, tactile interfaces with pin and casing configuration can be made to realize fingertip touch sensor for material identification and pattern recognition.

The EMH presented can also be used for realization of other types of sensors (e.g. inertial sensors, i.e. accelerometers and gyroscopes) or actuators. With use of appropriately designed appendages, 3D accelerometers, 2D biomimetic haltere-like gyroscopes and shear stress sensors can also be made. Applications using EMH in actuation mode are not investigated thoroughly in this dissertation, due to immediate needs for micro-hydraulic HAFS within the MAST program. Nonetheless, tri-gait locomotion pattern using EMH actuators are excellent candidate for micro-sized robots, due to lowered center of gravity. Additionally, EMH structures with vane-like appendages in actuation mode can be utilized for active flow control. Moreover, EMH

actuators can be configured in series or parallel to multiply deflection or force depending on the application.

In summary, this research work introduces the novel concept of electrostatic micro-hydraulic system, which exhibits a new paradigm in MEMS device designing. This high-performance versatile platform can be used in combination of various appendages to realize many MEMS sensors and actuators with unprecedented performance. The work presented herein is a foundation of a new class of MEMS devices utilizing EMH and similar hybrid platforms.

7 Appendix: Hotwire Hair-like Anemometer

7.1 Introduction

Ambient gas flow can be measured using micro electro mechanical systems (MEMS) devices [71] such as micro-scale thermal [72, 73, 74], resonating mass [75], differential pressure [76], lift-force [77], hair-like capacitive [23, 50, 45], or piezoresistive [21, 16] sensors, or by micro-fabricated hot-wire anemometers [78, 18]. However, all these sensors require complex structures or fabrication, considerably increasing cost. For applications where meso-scale sensor size is acceptable, conventional hot-wire anemometers are widely used. This type of sensor is made of platinum or tungsten wires stretched between two prongs, which hold the wire immersed in the fluid. With recent advancement in manufacturing technology, high-speed hot-wire anemometers are available at moderate to high cost [79]. Silicon-based hot-wire flow sensors were introduced in the late 1980s [80], have been studied [71, 72, 73, 74, 81] and are now commercially available. These sensors have very acceptable overall performance, with the capability for on-site integration with signal processing circuitry [82, 83]. However, these sensors are typically designed for mass flow measurement inside an enclosed tubular package, which makes them unsuitable for ambient gas flow measurement, e.g. of wind velocity.

Here a novel, low cost and easy to fabricate hair-like air flow sensor, which can detect external air flows is described. The sensor is a micro-scale hot-wire anemometer, which utilizes a bond-wire as the sensing element (Figure 7.1) [84].

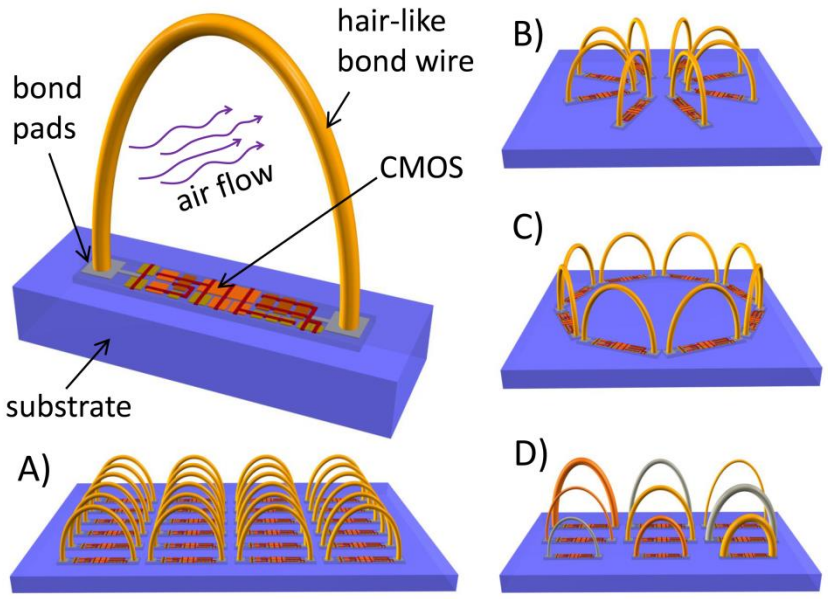

Figure 7.1 Schematic drawing of a hot-wire hair thermal flow sensor with integrated CMOS circuitry for transduction and/or processing. a) Dense array of hot-wire sensors, Various arrangements and orientations; b) star-like, c) circular and d) sensors of different height, wire gauge or materials.

The bond-wire extends above the surface of the substrate, thus saving valuable chip area and allowing for positioning of the sensing element out of the boundary layer. The sensor can be formed on a silicon substrate with prefabricated readout and signal conditioning integrated circuits underneath, to minimize the size of device for standalone operations, allowing the formation of dense sensor arrays for flow pattern imaging over large areas (Figure 7.1-A). The hair-like flow sensor fabricated with bond-wires uses a high throughput post-process technique in which the wire loops are formed by standard wire bonders that are routinely used in integrated circuit (IC) packaging. Therefore, the fabrication process is IC-compatible. In addition, since wire bonding is a post-IC process step, performed during the mandatory packaging procedure, no overhead expense is imposed, thus minimizing the cost of fabrication. Additionally, the sensing element specifications, i.e. bond-wire material, gauge and dimension, can be easily altered without modification of the substrate layout (with or without IC), which provides unprecedented flexibility for custom sensor design. It is trivial to incorporate different wire arrangements and

orientations, different wire materials and dimensions (Figure 7.1-A, B, C, and D). Such bond-wires can be used for a variety of sensing applications including inertial [84] and thermal sensing.

The air flow sensor introduced in this chapter can be used in many applications, including autonomous mobile platforms such as micro air vehicles (MAVs). The translational movement of these platforms occurs at moderate speeds (less than 20 $m.s^{-1}$), the size ranges from a few to tens of centimeters and their weight varies from a few 100 grams to a few kilograms. These platforms require sensors for navigation, control, and positioning as well as for mission-related functions such as detection of personnel and of various threats [54]. Flow sensors can provide valuable information in this regard. Air flow sensors with thermal transduction are an appealing option for mobile platforms that experience large inertial forces, since the transduction is minimally affected by inertial movements. However, currently available commercial hot-wire flow sensors are too fragile, too expensive, too large/heavy, or have excessively large power consumption to be used with MAVs [85].

7.2 Design and Implementation

7.2.1 Basic Concept and Design

Hot-wire anemometers operate based upon heat transfer from a heated wire through forced convection. The amount of heat sunk from the wire is directly proportional to the viscosity, density and velocity of the fluid in which the heated wire is immersed. The wire resistance varies with its temperature and thus the amount of heat sunk can be electrically sensed. If the density and viscosity of the fluid are known, the fluid velocity can be determined. Hot-wire sensors can operate in two modes: constant temperature anemometry (CTA) and constant current anemometry (CCA). In CTA mode, the temperature (or equivalently the resistance) of the hot-

wire is kept constant by continuously controlling the amount of current passing through it. Therefore, the power consumption indicates the flow speed. In CCA mode, a constant current is passed through the wire, and the resistance of the wire (i.e. the temperature of the wire) indicates the fluid flow speed. For both CTA and CCA modes, King's law [86] relates the hot-wire power consumption, *P*, to the fluid speed, *U*:

$$P = A + B\sqrt{U}, \qquad \textit{Eq. 7.1}$$

where *A* and *B* are constants that depend on wire geometry and material. Since *A* is the power consumption at zero velocity, the power consumed due to fluid flow is simply $B\sqrt{U}$ [87]. This increased power consumption is assumed to be primarily due to heat loss through forced convection. Therefore, to estimate *B* for wires with aspect ratio of about 100, as used in this work, the average Nusselt number [88] for a circular cylinder of infinite aspect ratio in a constant heat flux [89] is used:

$$Nu_D = 0.632\, Re_D^{\frac{1}{2}} Pr^{\frac{1}{3}}, \qquad \textit{Eq. 7.2}$$

where the Nusselt number is the ratio of convective to conductive heat transfer across a boundary. The Reynolds number, Re_D, corresponds to the ratio of inertial forces to viscous forces under given flow conditions (low Reynolds numbers correspond to laminar flow; large ones correspond to turbulent flow). Re_D for a cylinder (bond-wire) with diameter D is given by $Re_D = \frac{UD}{\nu}$ [88]. Pr is the Prandtl number, a dimensionless constant that depends only on the fluid properties: $Pr = \frac{\nu}{\alpha}$, where ν is the kinematic viscosity, and α is the thermal diffusivity [88]. Using Eq. 7.1 and heat transfer coefficient definitions [88], the heat loss, ΔQ, from a cylinder through forced convection at speed *U* can be obtained as:

$$\Delta Q = 0.632\,\pi k_f \left(\frac{D}{\nu}\right)^{\frac{1}{2}} Pr^{\frac{1}{3}} L\Delta T\sqrt{U}, \qquad \textit{Eq. 7.3}$$

in which k_f is the thermal conductivity of the fluid, L is the cylinder (bond-wire) length, and ΔT is the overheat temperature of the cylinder. If heat loss due to forced convection dominates the change in power consumption fluid flow is present, that is $\Delta Q \approx P - A = B\sqrt{U}$, then Eq. 7.3 can be used to estimate *B*. This equation will be used later to compare our experimental results with theory.

To design the hot-wire hair sensor, the wire material, wire geometry (wire gauge and length) and overheat temperature must be chosen. The goal is to co-optimize maximum and minimum detection levels and response time within the fabrication constraints. The maximum flow that can be measured by the hot-wire sensor is primarily constrained by the maximum available power. The greater the power budget, the higher the upper limit for flow speed. The minimum detectable air flow speed is the minimum velocity of forced convection required to overcome the natural convection flow generated by heated hot-wire itself. Natural convection flows are formed due to buoyancy of the heated fluid around the hot-wire, according to the temperature difference between the hot-wire and ambient. The minimum Reynolds number, Re_{min}, for a given overheat ratio, $\frac{T_m}{T_0}$, where T_m is the mean elevated wire temperature and T_0 is fluid ambient temperature, is:

$$Re_{min} = 1.85 \times Gr_D^{0.39} \left(\frac{T_m}{T_0}\right)^{0.76}, \qquad \textit{Eq. 7.4}$$

Gr_D is Grashof number, a dimensionless value that relates buoyancy to viscous forces:

$$Gr_D = \frac{g\beta(T_s - T_0)D^3}{\nu^2}, \qquad \textit{Eq. 7.5}$$

in which g is the acceleration of gravity, β is the volumetric thermal expansion coefficient, and T_s is the surface temperature of the wire. According to these equations, a temperature

difference of slightly over 13 K above ambient results in a minimum detectable velocity of 1 cm.s^{-1} [86]. In our design, an overheat ratio of about 1.05 or less is targeted.

To determine the response time of the sensor, its operation mode must be considered. For sensors operated in CTA mode, a differential equation governs heat transfer and electrical Joule heating of the electro-thermal system [86]. The time constant, τ_{cta}, of this differential equation sets the time scale of the sensor's Joule heating response to additional air flow. τ_{cta} is given by:

$$\tau_{cta} = \frac{\rho c A_W L(\overline{R}_s - R_f)}{\alpha R_0 \overline{I}_s^2 \left[2 g_A R_s (\overline{R}_s - R_f) + R_f^2\right]}, \qquad \textit{Eq. 7.6}$$

in which ρ, c and α are wire resistivity, specific heat and temperature coefficient of resistivity (TCR), respectively. L and A_W are wire length and cross-sectional area. $\overline{I}_s$ is the mean sensor current, $\overline{R}_s$ is mean sensor resistance at $\overline{I}_s$, R_f is sensor resistance at the fluid temperature, R_0 is sensor resistance at a reference temperature (i.e. room temperature), and g_A is the amplifier transconductance. This equation is derived based on a step input perturbation of either flow velocity or voltage [23]. It is clear from Eq. 7.6 that the sensor time constant can be reduced by using wires with lower specific heat and higher resistance (i.e., smaller diameter). Due to its higher resistivity and lower specific heat (Table 7.1), platinum wire is used as the primary material. Prototypes with aluminum were also made due to its wide usage in wire-bonding. For instance, according to (Eq. 7.6), for sensors made with 1.7-mm long, 25-μm diameter bond-wires, for a typical amplifier transconductance of 1.5×10^2 and overheat ratio of 1.05, the τ_{cta} is estimated to be 396 msec and 147 msec for aluminum and platinum sensors, respectively. When 17.5-μm diameter wires are used, the time constants are reduced to 188 msec and 72 msec, for Al and Pt, respectively. Note that the heat transfer analytical model discussed in this section assumes a wire that is infinitely far away from any other thermally conductive surface and that

there is very low heat loss through the ends, which may not be true for our relatively short wire [86]. Further modeling would be needed to fully account for time-dependent thermal losses to the substrate in our bonded wire anemometer, similar to what is described for a planar, elevated hot-wire in reference [90].

Table 7.1 Parameters and material properties used for calculation of sensor time constants.

Material Properties	**Unit**	**Platinum**	**Aluminum**
Density [91]	$kg.m^{-3}$	2.144×10^{4}	2.70×10^{3}
Specific heat capacity [91]	$kJ.kg^{-1}.K^{-1}$	0.1327	0.9016
Temp. Coeff. of Resistivity at 20°C [91]	K^{-1}	3.927×10^{-3}	4.290×10^{-3}
Resistivity at 20°C	nΩ.m	106.4 [91]	33.1*
Young's modulus [91]	GPa	146.86	68.95
Thermal expansion at 25°C [91]	$\mu m.m^{-1}.K^{-1}$	8.9	23.2
Extracted and Measured Parameters			
Wire length, *L*	mm	1.7	
Wire diameter, *D*	µm	17.5	25
Aspect ratio *(L/D)*	-	97	68
Op-Amp open loop gain	dB	130	
Measured sensor current, $\overline{I}_s$	mA	13.45	15.87
Measured** τ_{cta}	msec	70	120

* based on electrical measurement

** measurement resolution is 10 msec

This model suggests that the time domain behavior is strongly dependent on the diameter of the sensor wire. Conventionally-assembled hot-wire anemometers use wire diameters of a few microns [79]. For the prototypes presented in this chapter of dissertation, standard bond-wire gauge with 25-µm and 17.5-µm diameters have been used for aluminum and platinum, respectively. However lower gauge wire could be utilized for applications requiring faster sensor response. For instance, for 10-µm diameter bond-wires the time constants using the same parameters as above (i.e., the same length, current and transconductance) are reduced to 4.4 msec and 1.8 msec for aluminum and platinum, respectively. Bond-wires with 15-µm wire gauge are now commercially available [92]. Bonding of narrower diameter wires (e.g. 10-µm diameter) may become feasible in the near future as the packaging industry develops new capabilities.

7.2.2 Simulation

Conventional hot-wire anemometers use wires with very high aspect ratios ($L/D \geq 200$) in order to minimize the impact of heat loss due to conduction at the ends, and obtain a relatively flat temperature profile across a large region in the center of the wire for accurate measure of both linear and turbulent fluidic flows, as described in [93, 94]. They are also typically positioned so that they are very far away from any other thermally conductive surfaces, for optimum dynamic response, which adds to the volume of the sensor but allows straightforward modeling using the analytical equations presented in Section 7.2.1. For many integrated silicon hot-wires [73, 78, 81] or our bond-wires, typical aspect ratios are about equal to or less than 100, the wires may not be cylindrical, and the hot-wire is near to the substrate, causing heat losses not included in analytical models. Therefore, a model in COMSOL^{TM} has been developed using the *Joule Heating* multi-physics module to find the temperature distribution across a hot-wire for a given applied voltage (25 mV per mm of wire length), assuming conductive heat transfer through ambient air away from the wire. The absolute voltage value is adjusted such that the wire current is the same for all configurations. Modeling convective heat transfer requires additional 3-dimentional multi-physics modeling, and therefore is not included here.

Four different 2-D configurations are modeled and are shown schematically in Table 7.2. First, a 1-mm long aluminum wire ($L = 1$ mm) with 25-µm diameter stretches across a 1-mm long trench ($L = L_F$) in a silicon wafer, so that the wire lies parallel to the silicon substrate, to model silicon hot-wires [73, 78, 81]. Two trench depths are modeled: (A) 10 µm and (B) 100 µm. Second, a 25-µm diameter aluminum looped wire extending above the surface of a silicon substrate is modeled. Two cases are modeled: (C) a 1-mm long wire (L) which occupies a 0.5 mm footprint (L_F) on the silicon surface and (D) a 2-mm long wire, which occupies a 1-mm

footprint. Cases C and D will be used to explain the relative advantages of looped wires. It is assumed that the looped wires have elliptical contours. The dimensions of the 2-mm looped wire model (D) are chosen to match the fabricated devices. However, the deformation at the base of the wire, which occurs during the wedge-bonding process, is not included in the model. The silicon substrate with dimensions listed in Table 7.2 is assumed to be mounted on a alumina packaging block and the temperature on the bottom side of the package is kept constant at 293.15K (20°C). Therefore, heat generated by the hot-wire can elevate the silicon substrate and package temperatures.

Table 7.2 Schematic drawings of various wire configurations, dimensions and material properties used in COMSOL simulation.

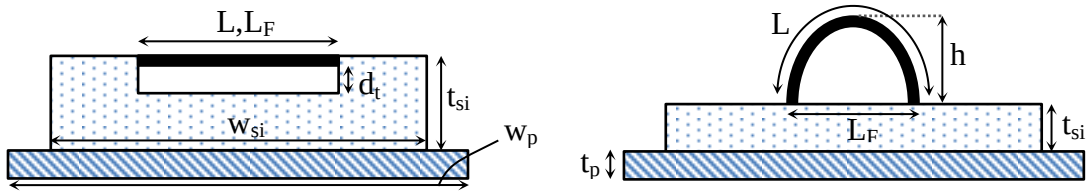

	L [mm]	d_t [µm]	L_F [mm]	h [mm]	w_{si} [mm]
A: 1mm straight wire, 10-µm gap	1.0	10	1.0	-	1.82
B: 1mm straight wire, 100-µm gap	1.0	100	1.0	-	2.00
C: 1mm looped wire, constant length	1.0	-	0.5	0.386	1.75
D: 2mm looped wire, constant footprint	2.0	-	1.0	0.773	1.75
A-D: t_{si}: 0.5 mm, t_p: 1 mm, w_p: 3 mm, wire thickness: 25 µm, voltage/L: 25mV/mm					

Material Properties (from COMSOL™)

	Elec. Cond. [$S.m^{-1}$]	Relative permittivity	Density [$kg.m^{-3}$]	Thermal Cond. [$W.m^{-1}.K^{-1}$]	Heat capacity [$J.kg^{-1}.K^{-1}$]
Air	5×10^{-15}	1	1.225	0.024	1012
Silicon	1×10^{-12}	11.7	2329	130	700
Aluminum	2.36×10^{-12}	1	2730	155	893
Alumina	1×10^{-12}	3.8	3980	36	930

The hot-wire and silicon substrate along with the package are inside of a 50×50 mm^2 block of air (the bottom side of the package is centered in the bottom of the air block). For the sake of comparison, the width of silicon substrate is adjusted so that the same mass of silicon is present

in all cases (Table 7.2). Boundary conditions are set as follows: for the bottom side of the air block is ambient temperature of 293.15K; for all other sides continuity is assumed. Material properties (based on COMSOL^{TM} material library) and geometrical dimensions used in this simulation are listed in Table 7.2. The mesh size is reduced as much as possible but sufficient mesh size is used in order to obtain mesh-independent simulation results.

Simulation results of temperature distribution versus normalized wire length are plotted in Figure 7.2. The peak temperature obtained on the wire is observed and compared to the ambient temperature used in the model of 293.15K, the difference of which is referred as ΔT_{PEAK}. Temperature distributions are shown for cases A and B in Figure 7.2: a deeper trench provides better thermal isolation, allowing a higher temperature in the middle of the wire.

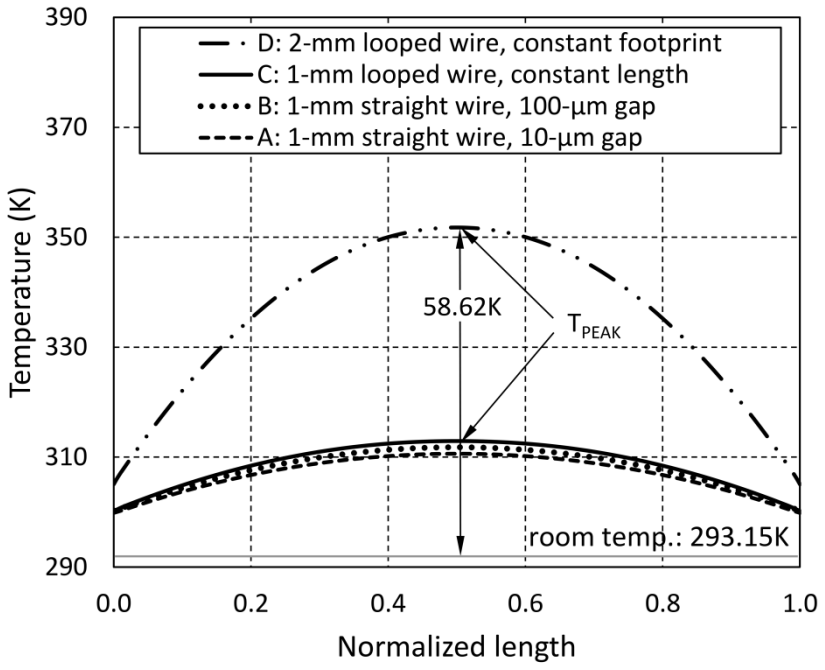

Figure 7.2 Simulation results showing temperature distributions for aluminum hot-wires with 25 mV per millimeter length applied across the wire, comparing straight vs. looped geometries with different footprints, lengths, and gaps to the substrate.

Simulations results shown in Figure 7.2 suggest that for 1-mm long, 25-µm wide wire stretched over a 100-µm trench (case B), the ΔT_{PEAK} is 18.6K while that of the same wire over a

10-μm trench (case A) is 17.5K. Although Joule heating from both wires is the same, with better thermal isolation, that is to say, more space between the hot-wire and the substrate, less heat is sunk by silicon substrate. Therefore, in the latter case, the silicon substrate temperature rises more than that of the former case and the wire temperature is lower. However, if the same wire is looped over the silicon substrate with the same current, it can provide better isolation. As indicated in Figure 7.2, ΔT_{PEAK} for 1-mm long looped wire (case C) is 19.8K. This implies that to maintain a given temperature, the looped wire architecture consumes about 13% less power (case A) for the same wire length and current. Moreover, trench formation consumes a large silicon chip area. In contrast, looped wires extending away from the substrate plane can achieve even better thermal isolation while the valuable chip area underneath the looped-wire sensor can be used for CMOS interface/signal processing circuits. For a given wire length, if the wire is looped and extended away from the substrate surface, it will have a smaller footprint area, thereby enabling denser arrays. The case where the footprint size is kept constant (case D) has been explored, so the looped wire length and thus its resistance will increase. In this case, by keeping the current passing through wire constant, a higher temperature is achieved due to increased resistance of the wire. However, there is another factor boosting the temperature rise, which is better thermal isolation. Simulation results show that for a looped wire twice the length of straight one, the resultant ΔT_{PEAK} is 58.6K (Figure 7.2). Based on the straight wire ΔT_{PEAK} of 18.6K, one would expect the resistance increase alone to increase the ΔT_{PEAK} by about twice to ~37.2K. Thus, it can be concluded that enhanced thermal isolation by further moving the bond-wire away from the surface increases the equilibrium ΔT_{PEAK} by an additional 58%.

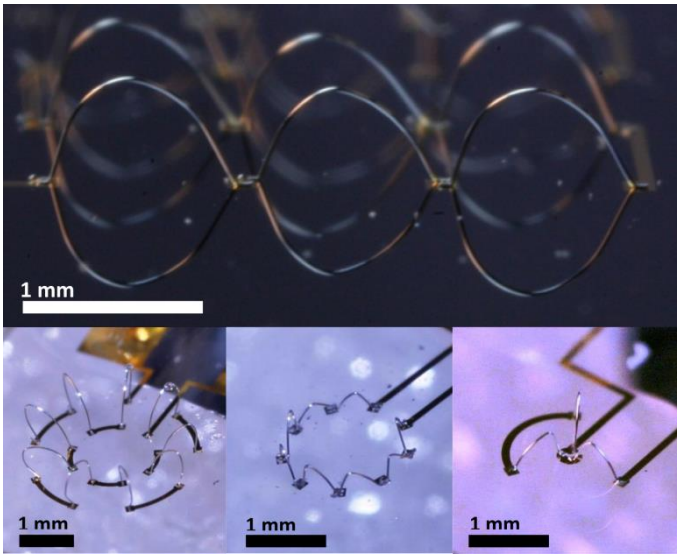

Figure 7.3 (Upper) Fabricated hot-wire sensors with micro-scale bond-wires on silicon substrate. (Lower) Various patterns and arrangements of bond-wires on glass substrates. The bond-wires are shown linked in series. However for directional sensing it might be preferable to separate the bond-wire electrodes.

7.2.3 Fabrication

The hair-like hot-wire sensor reported in this chapter consists of a semi-loop of 25-µm aluminum alloy (AlSi 1%) bond-wire (or 17.5-µm platinum) formed by conventional wire bonding technique between two Cr/Au bond pads. The metal bond pads are e-beam evaporated and patterned on a borosilicate glass (or silicon) substrate. Both wedge bonding and ball bonding can be used to realize the structure shown in Figure 7.1; wedge bonding has been used here. Wire bonding is ubiquitously used for IC packaging, therefore, sensor fabrication with bond-wires can be considered an IC-compatible technique. Moreover, since the sensing elements are essentially an additional bond-wire "interconnect", the sensor does not impose any extra IC process steps so that the cost of sensor fabrication and integration is minimal. By design, the sensors are thermally isolated from the substrate, as described in Section 7.2.2. By extending above the substrate plane, the loops save costly IC die area compared to other planar anemometer fabrication methods [78]. In addition, formation of three-dimensional arrays of hair-like hot-wire

types of sensors is very simple to implement and many configurations can be realized by rearranging the bond pads layout and/or changing the bond loop settings. Figure 7.3 shows various combinations of bond-wire loops that potentially can be used for directional flow sensing or other applications in the future.

7.2.4 Interface Circuit

The sensor is used in CTA mode, in other words, the wires are elevated to the target overheat ratio of about 1.05 and kept constant through a closed loop circuit shown in Figure 7.4.

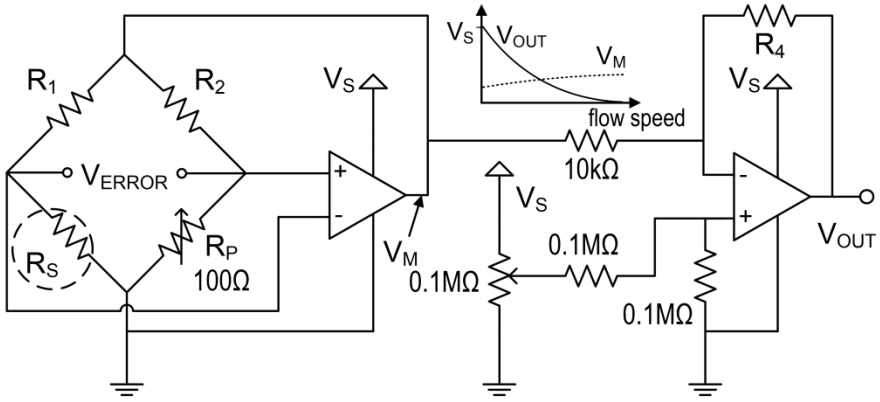

Figure 7.4 Schematic of the read-out circuit used for a constant temperature hot-wire hair flow sensor, RS. The second op-amp stage scales the first op-amp stage output to rail-to-rail and removes the DC bias of the first stage by adjusting the virtual ground of the second op-amp. Resistors values in parentheses are for the platinum wire interface circuit.

The first op-amp shown in this figure constantly adjusts its output voltage to keep the resistance of the sensor, R_S, the same and thus keep the bridge in balance, with an error voltage of zero. The wire resistance is directly related to its temperature and therefore the bridge voltage, V_M, (the output of the op-amp) increases monotonically with the fluid flow. The maximum range of this intermediate voltage is limited. In order to obtain maximum resolution once the analog output is converted to a digital signal through an analog to digital convertor (ADC), the output is scaled from rail-to-rail (i.e. from ground to the battery supply level). The second op-amp stage

shown in Figure 7.4 subtracts a reference value from V_M and amplifies the difference so that at quiescence the output, V_{out}, is V_S, and at maximum flow V_{out} is zero. For standalone operation of the sensor, a printed circuit board (PCB) is made and the sensor is elevated from the board to prevent flow shadowing by circuit elements (Figure 7.5). An isolation box wraps around the circuit to minimize circuit-induced heating of the sensor and reduce the background convection flow generated by the heated circuit elements. Figure 7.5 shows the sensor mounted with the PCB interface circuit of Figure 7.4. A potentiometer (R_P) is used in this prototype circuit to set the initial overheat ratio and to calibrate the sensor.

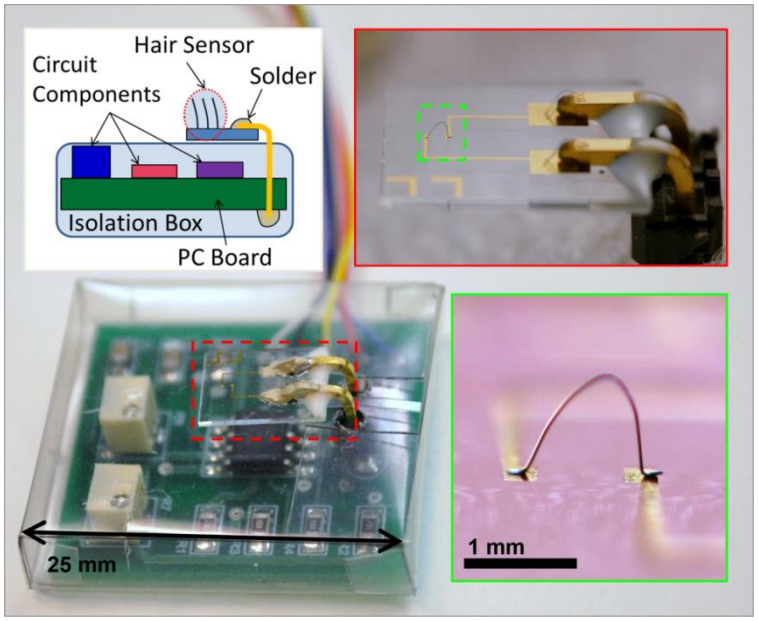

Figure 7.5 A fabricated hot-wire sensor along with the PCB and flow isolation package.

7.3 Experimental Results

Fabricated sensors with aluminum and platinum micro-bond-wires are characterized in a controlled lab environment. A commercial hot-wire anemometer (HHF42, Omega, Stamford, CT, USA) was used to calibrate the bond-wire sensor. As a proof-of-concept, a hair-like air flow sensor and its circuitry are integrated with an autonomous mobile platform and intelligent robotic behavior is exhibited.

7.3.1 Sensor Characterization

7.3.1.1 Flow Response

Both 25-µm aluminum and 17.5-µm platinum hot-wire hair sensors are tested in a six-inch wind-tunnel while V_M and V_{OUT} are recorded as the wind-tunnel fan frequency and thus wind speed, are increased (Figure 7.6). Tests are performed with 3.3 V and 5 V DC supplies. For a given supply voltage, the platinum wire sensor has larger full-scale range due to its higher specific resistivity and the lower wire gauge used. The aluminum wire hair-sensor operated at 3.3 V-supply exhibits an almost linear response for flows ranging from about 0.2 to 4.0 $m.s^{-1}$. The platinum sensor operated at 5 V-supply shows linearity for air flows from 2 $m.s^{-1}$ to greater than 17 $m.s^{-1}$. The upper limit of the sensor range is set by the maximum output power of the first stage op-amp or the saturation point of the voltage-flow plot, whichever comes first. In our experiments on the platinum bond-wire hair sensor, no saturation is observed up to 17.5 $m.s^{-1}$. At higher flow speeds, mechanical stability of the sensor mounting fixture inside the wind-tunnel could not be maintained. Hence, the actual full-scale range of the sensor might be even larger than 17.5 $m.s^{-1}$.

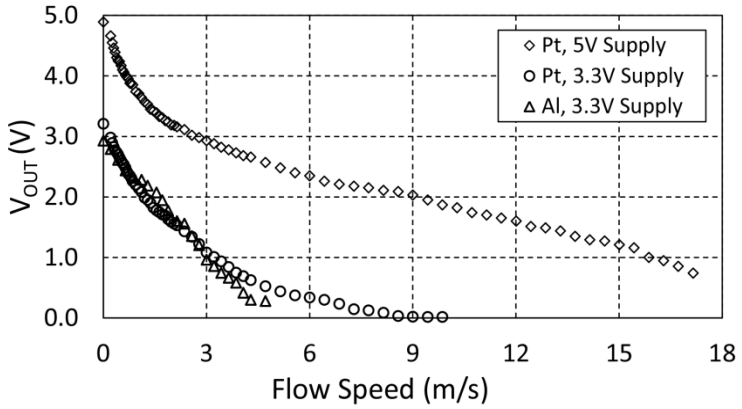

Figure 7.6 Platinum and aluminum sensors flow response in wind-tunnel with 3.3 V and 5 V supply.

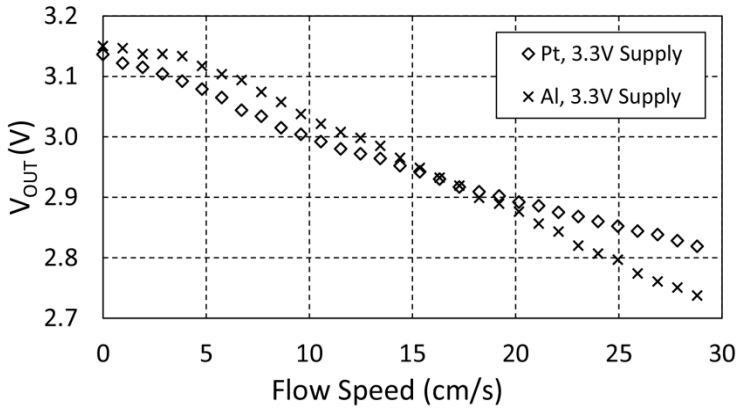

Figure 7.7 Sensor response to low flow speed in rate table with 3.3 V supply.

Characterization of the sensors at low air flow speed is challenging because wind-tunnels lose linearity at low flow speeds. The lower limit of air flow speed that can be reliably sustained in the wind-tunnel used here is about 20 $cm.s^{-1}$, below which the flow is not unidirectional and flow speed fluctuations are observed. Moreover, the lower bound of existing sensors used for air flow speed calibration inside the wind-tunnel is 20 $cm.s^{-1}$ [95], which is larger than the expected minimum flow detection level of our sensors. Therefore, conventional wind-tunnels are not capable of reliable measurements at these speeds. A method of moving the sensor through stagnant air at a constant velocity has been utilized by mounting it on an enclosed rate table to achieve accurate low speed measurements [54]. Since speed of the rate table is accurately controlled and the whole rate table system operates in an enclosed chamber, the relative speed of the table to stagnant air can be precisely controlled in the low-speed range. Figure 7.7 shows low flow regime characterization of both aluminum and platinum sensors. The minimum detectable air flow speeds are 2.8 $cm.s^{-1}$ and about 1 $cm.s^{-1}$ for aluminum and platinum sensors respectively. The plots in Figure 7.6 and Figure 7.7 show the relative linearity of the aluminum sensor response to flow speeds smaller than 4.5 $m.s^{-1}$.

To obtain accuracy, sensitivity and resolution, two regimes of operation for the sensors have been considered, low flow (LF, smaller than 50 $cm.s^{-1}$) and high flow (HF larger than 2 $m.s^{-1}$) regimes. Accuracy is defined as the maximum error between sensor calibration curve and the experimental data in terms of percentage of full-scale range for each sensor. Aluminum wire sensor exhibits accuracy of 0.08% and 2.5% in LF and HF regimes, respectively; those of platinum wire sensor at 3.3V supply are 0.06% and 4.0%. Sensitivity is defined as the slope of linear regression of experimental data points in each regime. Finally, resolution is obtained by dividing the output noise at quiescence by sensitivity in each regime. Resolution of sensors ranges from 0.93 $cm.s^{-1}$ to 1.7 $cm.s^{-1}$ in LF, and 2.6 $cm.s^{-1}$ to 13.7 $cm.s^{-1}$ in HF regimes. These parameters are listed in Table 7.3.

Table 7.3 Summary of platinum and aluminum sensor performance. Values in bold refer to the platinum sensor when supplied with 5 V.

		Pt wires	**Al wires**
Wire diameter		17.5 μm	25 μm
Wire length		1.7 mm	1.7 mm
Supply voltage		3.3 **(5)** V	3.3 V
Range		0 – 10 **(0-17.5)** $m.s^{-1}$	0 – 5 $m.s^{-1}$
Resolution	LF*	1.4 **(1.7)** $cm.s^{-1}$	9.3 $mm.s^{-1}$
	HF†	10.2 **(13.7)** $cm.s^{-1}$	2.6 $cm.s^{-1}$
Sensitivity	LF	1.11 **(1.17)** $V/(m.s^{-1})$	1.61 $V/(m.s^{-1})$
	HF	196 **(146)** $mV/(m.s^{-1})$	586 $mV/(m.s^{-1})$
Min. det. flow		1.0 $cm.s^{-1}$	2.8 $cm.s^{-1}$
Accuracy	LF	0.06 **(0.39)** %	0.08 %
	HF	4.0 **(3.9)** %	2.5 %
Time constant		70 msec	120 msec
Power	idle	56 **(82)** mW	85 mW
	max	154 mW at 10 $m.s^{-1}$	169 mW at 4.5 $m.s^{-1}$

*LF: Low Flow, for $< 0.5 m.s^{-1}$
†HF: High Flow, for $> 2 m.s^{-1}$

7.3.1.2 Response Time

In order to measure how fast the hot-wire reacts to a step flow, the following experiments has been conducted. Both aluminum and platinum hot-wire hair sensors are affixed in front of a fan

with a shutter-like baffle in between the fan and sensors. To generate a step-like flow, the fan is turned on and the baffle is quickly removed while the sensor outputs are measured.

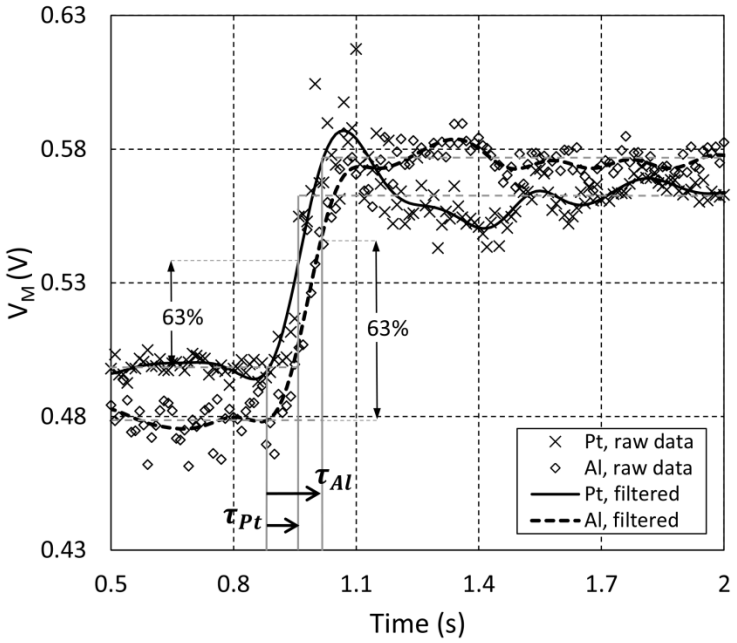

Figure 7.8 Time constant measurement of platinum and aluminum wire sensors. Time constant calculation is based on transition time from baseline to (1-e^{-1}) (63%) of final value.

Figure 7.8 plots sensor responses to the generated step flow. The platinum sensor has a faster response of 70 msec compared to 120 msec for the aluminum sensor. As mentioned in Section 2a, the described theoretical model assumes infinitely long circular cylinder far away from a wall. When a hot-wire sensor operates in close proximity to a wall, its dynamic response deteriorates [90]. Therefore, Eq. 7.6 will not precisely model the behavior of the hair-like hot-wire presented here. However, it can be used to provide a rough estimate of the time-domain response, as well as comparison between materials for design purposes. Based on the model, platinum responds faster than aluminum to flow perturbations, which is in agreement with the experimental results. Additionally, the TCR of multiple contacts in the path from the bond-wires to the circuit may contribute to discrepancies between the model and experimental results.

7.3.1.3 Power Consumption

The power consumption vs. air flow speed of the sensors made with 25 µm aluminum and 17.5 platinum bond-wires was also measured. Figure 7.9 shows that platinum wire sensors are more power efficient than aluminum wire sensors. However, aluminum wire-bonds are regularly used in IC packaging whereas platinum wire-bonds are not very common due to their greater resistance.

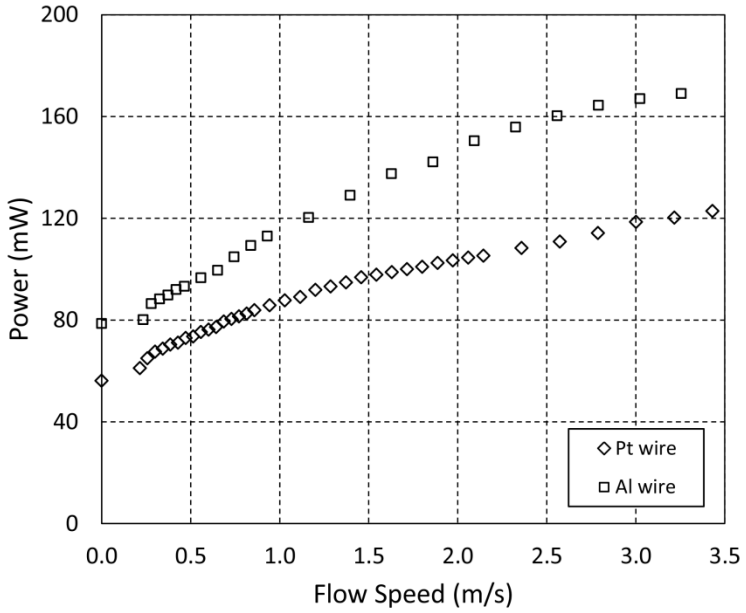

Figure 7.9 Total power consumption of platinum and aluminum wire sensors.

Figure 7.10 plots power consumed by the bond-wire (not the bridge power) versus the square root of air speed. According to the King's law in Section 7.2.1, power consumption linearly increases with square root of air speed. Extracted values of B based on the experimental results of Figure 7.10 are 0.25 mW/(m.s^{-1})^{½} for Al sensors and 0.34 mW/(m.s^{-1})^{½} for Pt sensors. At ambient temperature of 25 °C, using Eq. 7.3, dimensions and bias conditions given in Table 7.1, air thermal conductivity (k_f) of 2.57×10^{-2} W.m^{-1}.K^{-1}, kinematic viscosity (ν) of 15.82×10^{-6} m^2.s^{-1} and Prandtl number (Pr) of 0.714, $\Delta Q = 11.466\, L\, \Delta T \sqrt{DU}$ is obstained. Therefore, overheat ratio of sensors are estimated to be 1.012 and 1.014 for Al and Pt wire sensors, respectively.

These values are in reasonable agreement with the targeted overheat ratio of 1.05 or below, based on calculations. Discrepancies may be due to the small wire length to diameter ratio (<100) and its proximity to a thermally conductive substrate. Table 3 summarizes aluminum and platinum wire sensor performance. Power consumption is compared for platinum and aluminum sensors under conditions of quiescence (idle power consumption) and full scale flow (maximum power consumption).

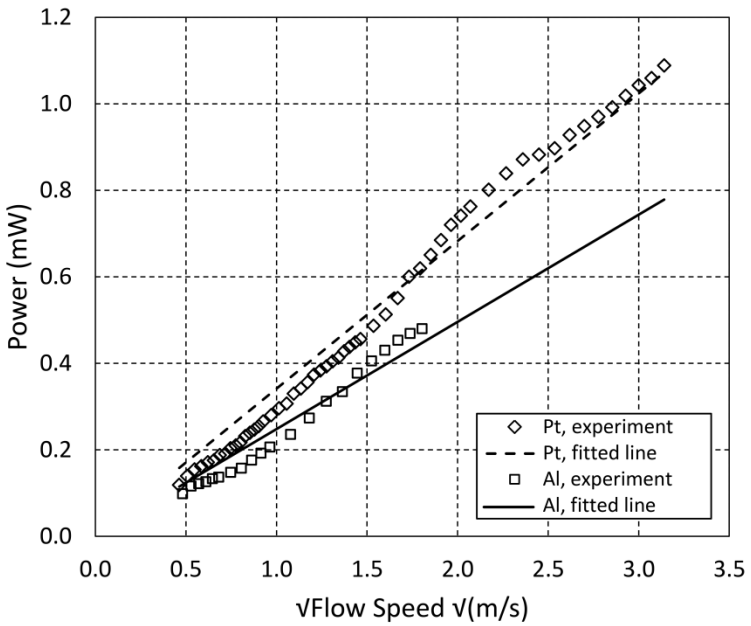

Figure 7.10 King's law evaluation, overheat ratio is estimated based on experimental data.

7.3.2 Integration with Crawler

The hot-wire sensor has been integrated with a small hexapedal crawler to exhibit intelligent behavior [54]. The sensor is powered by the onboard robot battery, and the analog voltage output of the sensor is connected to the ADC input of the crawler's onboard controller. The robot is programmed to avoid airflow using the following algorithm: it moves in a random direction for two seconds, then remains motionless and measures flow. If the measured flow is below a preset threshold level, the robot considers that spot to be a "safe" location and remains still. If it senses air flow larger than the pre-set threshold, it again moves in a random direction for a two-second

period. The loop is repeated until it finds a “safe” location. The micro-hot-wire sensor shown in Figure 7.5 was used to successfully implement and test this algorithm on the crawler robot, demonstrating the sensor utility on mobile platforms. The tests are more fully described in reference [54].

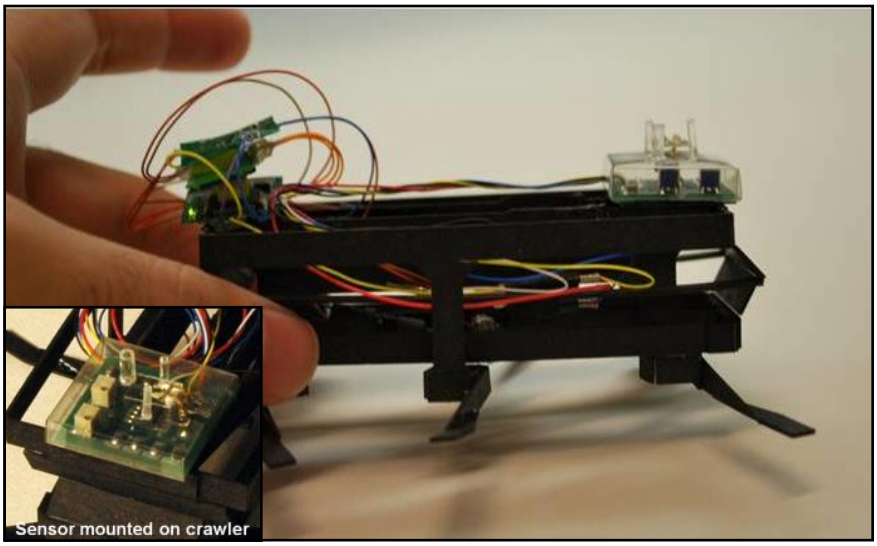

Figure 7.11 Robotic crawler with integrated hot-wire hair sensor. The posts are used to protect the hot wire from mechanical damage in case the robot flipped over.

7.4 Discussion

Sensors made with platinum bond-wires tend to exhibit superior performance in terms of response time and power consumption. Platinum has lower specific heat, which improves the thermal dynamics of the system: since the heat energy stored in the platinum wire is smaller, it can be heated and cooled more quickly than a wire of aluminum with the same volume and geometry. In addition, platinum has higher resistivity compared to aluminum, which for a given wire geometry and intended overheat ratio lowers the power consumption. Moreover, platinum has larger Young’s modulus that allows use of a narrower diameter wire, compared to aluminum, to obtain the same mechanical strength of the loop structure. As a result, with platinum bond-wires sensor resistance can be further increased by reducing the wire diameter, which further

lowers power consumption. Table 7.1 compares the physical properties of bulk platinum and aluminum that are important in the design of flow sensors. In the future, a wide range of materials -such as titanium, tantalum, tungsten, etc., and other wire attachment methods, such as micro-welding, can be used to form the looped micro-wires above the surface of the substrate [96, 97].

The hot-wire hair sensors described here have excellent overall performance. Table 7.4 compares other reported research and commercial flow sensors. The full scale range of the hair hot-wire sensor (17.5 $m.s^{-1}$) is comparable with commercial hand-held hot-wire anemometers (25 $m.s^{-1}$) [95]. However, our sensor minimum detection of air flow speed (1-2 $cm.s^{-1}$) is lower than commercial sensors (5-20 $cm.s^{-1}$) and most research sensors (with the exception of two cases which exhibit minimum detection levels of 3 $mm.s^{-1}$ [98] and 1 $mm.s^{-1}$ [99]). The minimum detection enhancement is made possible by using small overheat ratio. However, this may cause flow measurement bias as a result of small temperature fluctuations in the fluid (air) stream. Higher overheat ratios are conventionally used to mitigate this bias; nonetheless, this shortcoming can be simply addressed by integration of hot-wire sensor with an on-chip thermometer included in the CMOS interface circuit. In this fashion, with simultaneous measurement of fluid stream temperature, any bias in flow measurement can be corrected. Additionally, with another on-chip circuit, the overheat ratio can be precisely controlled.

Table 7.4 Hair-like hot-wire sensor performance compared with previously reported research and commercial flow sensors.

Transduction	Reference	Size	Full Scale Range	Min det. Flow	Response time	Power (sensor)
thermo-resistive	Tabata '86 [80]	4×4×0.36 mm^3	14 m/s	-	100 ms	8.6 mW
	Neda '96 [73]	1×1×0.3 mm^3	35 m/s	5 cm/s	140 µs	6 mW
	Liu '03 [78]	-	20 m/s	-	< 200 µs	-
	Omega HHF-SD1 [95]	Φ12×280 mm	25 m/s	20 cm/s	-	135 mW w/circuit
	Dantec Dynamics [79]	Φ1.9×30 mm	500 m/s	5 cm/s	11 ms CCA 2.5 µs CTA	-
	Sensirion ASF 1400 [100]	-	55 m/s*	2 cm/s*	min: 142 ms max: 1.28 s	180 mW w/circuit
	This work	Sensor: 1×2×2 mm^3 With circuit: 25×20×12 mm^3	> 17.5 m/s	1.0 cm/s	70 ms	82 mW (idle) 154 mW (max) w/circuit
resonating	Bouwstra '90 [75]	2×1 mm^2	3 m/s	-	-	20 mW
thermo-electric	Kaltsas '99 [98]	1.1×1.5 mm^2	0.4 m/s	3 mm/s	4.5 ms	67mW
	Makinwa '02 [101]	-	18 m/s	2 m/s	-	400-600 mW
piezo-resistive	Svedin '03 [77]	6×3 mm^2	55 m/s	10 cm/s	> 1s	-
	Su '03 [102]	-	3.5 m/s	7 cm/s	-	-
	Liu '07 [21]	-	15 m/s	4.5 cm/s	< 1 ms	-
capacitive-hair	Krijnen '09 [99]	-	2 m/s	1 mm/s	< 1 ms	-

**calculated from mass flow measurement data given in datasheet.*

Heat transfer from a hot-wire generally depends on the flow yaw, pitch and roll angles and it is locally dominated by the flow velocity component normal to the wire [86]. The specific U-shape of the hot-wires described in this chapter may cause ambiguity in flow measurement as shown in ref. [54]. Well-designed packaging can be used to guide the flow stream so it is always perpendicular to the wire (normal to the "*sensor plane*" in which the whole U-shape contour is contained). In addition, an array of at least two sensors (such as those shown in Figure 7.3) can be used for directional flow measurements. In some applications, such as autonomous micro-vehicles [54], a flow sensor may be used as an "*event detector*" to sense the presence of flow in an arbitrary direction, in which case a sensor with isotropic sensitivity is preferred. This type of "*event detectors*" can be realized with an array of sensors in circular or radial forms as schematically shown in Figure 7.1-B and Figure 7.1-C.

The size and weight of the total sensor system is very small: its weight is below 2 grams and the footprint of the PCB is smaller than one square inch, which is an advantage for applications with limited payload. The sensor size and weight can be further reduced if CMOS interface circuitry is used, as in ref. [82].

The hot-wire hair sensor has a moderate response time of about 70 ms. While some other sensors are slower than 100 ms [77, 80], many others respond to stimuli in less than 1 ms [73, 99, 21, 78]. The slow response time of our sensor is mainly due to the higher wire gauge used in wire-bonding compared to the wires used in conventional commercial hot-wire anemometers. Wires with larger diameters have smaller resistance and larger bulk mass. The former elevates power consumption and the latter lowers speed. The increased power consumption can be compensated by increasing the R_1/R_S ratio in the readout circuit, although this comes at the expense of reduced sensitivity. Improved wire-bonding techniques may allow for the use of narrower diameter bond-wires in order to further improve the response time and power performance of our sensor. Narrower wire diameter also leads to a higher aspect ratio ($L/D \approx 200$) for a given wire length, which alleviates conductive heat dissipation through the two axial ends of wires. Overall, our sensor offers excellent performance using an extremely low-cost fabrication technique, with the only tradeoff being the moderate response time.

The sensor performs well when exposed to moderate accelerations, vibrations, and shocks such as those experienced on the hexapedal robotic platform during its translational movement [9]. The sensor is anticipated to perform well in different humidity conditions although it needs recalibration since the heat transfer of air varies with relative humidity. Additionally, our hair-like hot-wire sensor ages well, showing the same sensitivity, range and overall performance over more than two years of laboratory testing.

7.5 Conclusion

A new low-cost method for fabrication of hair-like hot-wire anemometers based on wire bonding technology has been demonstrated. The fabricated air flow sensors are lightweight, low power, with large full-scale range and small minimum detection level. Since the sensors are made in an IC post process step, the cost of fabrication is drastically lower than competitive MEMS devices. A PCB interface circuit is designed for stand-alone operation of the sensor, for example on a robotic mobile platform. Both aluminum and platinum wire sensors are fabricated and characterized. The platinum hot-wire hair sensor has superior performance in terms of speed and power consumption. The achieved performance of this class of hot-wire sensors makes an appropriate component to be used for navigation, control, positional and situational awareness on various autonomous mobile platforms, as well as in many other applications requiring low-cost, compact sensors for wind or air flow sensing.

References

[1] M. De Volder and D. Reynaerts, "Pneumatic and hydraulic microactuators: a review," *Journal of Micromechanics and Microengineering,* vol. 20, no. 4, pp. 1-18, 2010.

[2] H. Kim, S. Lee and K. Najafi, "High-force liquid-gap electrostatic hydraulic micro actuators," in *11th Int. Conf. on Miniaturized Systems for Chemistry and Life Sciences (μTAS '07)*, Paris, Oct 2007.

[3] H. Kim and K. Najafi, "An Electrically-Driven, Large-Deflection, High-Force, Micro Piston Hydraulic Actuator Array for Large-Scale Microfluidic Systems," in *Micro Electro Mechanical Systems, 2009. MEMS 2009. IEEE 22nd International Conference on*, Sorrento, Italy, Jan 2009.

[4] R. McNeill Alexander, "Antennae as Gyroscopes," *Science,* pp. 771-772, 9 February 2007.

[5] M. Izumikawa, R. Minoda, K. Kawamoto, K. A. Abrashkin, D. L. Swiderski, D. F. Dolan, D. E. Brough and Y. Raphael, "Auditory Hair Cell Replacement and Hearing Improvement by Atoh1 Gene Therapy in Deaf Mammals," *Nature Medicine,* vol. 11, no. 3, pp. 271-276, March 2005.

[6] G. A. Jacobs, J. P. Miller and Z. Aldworth, "Review Computational Mechanisms of Mechanosensory Processing in the Cricket," *The Journal of Experimental Biology,* vol. 211, pp. 1819-1828, 2008.

[7] M. E. Benser, R. E. Marquis and A. J. Hudspeth, "Rapid, Active Hair Bundle Movements in Hair Cells from the," *The Journal of Neuroscience,* vol. 16, no. 18, pp. 5629-5643, 1996.

[8] J. Conroy, G. Gremillion, B. Ranganathan and J. S. Humbert, "Implementation of Wide-field Integration of Optic Flow for Autonomous Quadrotor Navigation," *Autonomous Robots,* vol. 27, no. 3, pp. 189-198, October 2009.

[9] P. Birkmeyer, K. Peterson and R. S. Fearing, "DASH: A Dynamic 16g Hexapedal Robot," *Intelligent Robots and Systems, 2009. IROS 2009. IEEE/RSJ International Conference on,* pp. 2683-2689, October 2009.

[10] R. J. Houghtalen, A. O. Akan and N. H. C. Hwang, Fundamentals of Hydraulic Engineering Systems (4th Edition), Prentice Hall, 2011.

[11] J. OK, M. Chu and C. J. Kim, "Pneumatically driven microcage for micro-objects in biological liquid," in *Micro Electro Mechanical Systems, 1999. MEMS '99. Twelfth IEEE International Conference on*, Orlando FL, 1999.

[12] S. Mutzenich, T. Vinay and G. Rosengarten, "Analysis of a novel micro-hydraulic

actuation for MEMS," *Sensors and Actuators A: Physical,* vol. 116, no. 3, pp. 525-529, 2004.

[13] Y. Lu and C. Kim, "Micro-finger articulation by pneumatic parylene balloons," in *TRANSDUCERS, Solid-State Sensors, Actuators and Microsystems, 12th International Conference on,* Boston, MA, June 2003.

[14] Y. Matsumoto, X. Arouette, T. Ninomiya, Y. Okayama and N. Miki, "Vibrational Braille Code Display With Mems-Based Hydraulic Diplacement Amplification Mechanism," in *Micro Electro Mechanical Systems (MEMS), 2010 IEEE 23rd International Conference on*, Wanchai, Hong Kong, 2010.

[15] J. Watanabe, H. Ishikawa, X. Arouette, Y. Matsumoto and N. Miki, "Artificial tactile feeling displayed by large displacement MEMS actuator arrays," in *Micro Electro Mechanical Systems (MEMS), 2012 IEEE 25th International Conference on*, Paris, 2012.

[16] Y. Ozaki, T. Ohyama, T. Yasuda and I. Shimoyama, "An air flow sensor modeled on wind receptor hairs of insects," in *Micro Electro Mechanical Systems, 2000. MEMS 2000. The Thirteenth Annual International Conference on*, Miyazaki, Japan, Jan 2000.

[17] K. Noda, K. Hoshino, K. Matsumoto and I. Shimoyama, "Fabrication of the Flexible Sensor Using SOI Wafer by Removing the Thick Silicon Layer," in *Micro Electro Mechanical Systems, 2006. MEMS 2006 Istanbul. 19th IEEE International Conference on* , Istanbul, Turky, Jan 2006.

[18] S. Haasl, D. Mucha, V. Chernoray, T. Ebefors, P. Enoksson, L. Lofdahl and G. Stemme, "Hybrid mounted micromachined aluminium hot-wire for near-wall turbulence measurements," in *Micro Electro Mechanical Systems, 2002. The Fifteenth IEEE International Conference on*, Las Vegas, NV, Jan 2002.

[19] B. Zhang, H. Qiao, S. Chen, J. Liu, W. Zhang, J. Xiong, C. Xue and G. Zhang, "Modeling and characterization of a micromachined artificial hair cell vector hydrophone," *Microsystem Technologies,* vol. 14, no. 6, pp. 821-828, 2008.

[20] J. Engel, J. Chen, C. Liu and D. Bullen, "Polyurethane rubber all-polymer artificial hair cell sensor," *Journal of Microelectromechanical Systems (JMEMS),* vol. 15, no. 4, pp. 729-736, Aug 2006.

[21] N. Chen, C. Tucker, J. Engel, Y. Yang, S. Pandya and C. Liu, "Design and Characterization of Artificial Haircell Sensor for Flow Sensing With Ultrahigh Velocity and Angular Sensitivity," *Journal of Microelectromechanical Systems (JMEMS),* vol. 16, no. 5, pp. 999-1014, Oct 2007.

[22] C. M. Bruinink, R. K. Jaganatharaja, M. J. de Boer, E. Berenschot, M. L. Kolster, T. S. J. Lammerink, R. J. Wiegerink and G. J. M. Krijnen, "Advancements in Technology and Design of Biomimetic Flow-Sensor Arrays," in *Micro Electro Mechanical Systems, 2009. MEMS 2009. IEEE 22nd International Conference on*, Sorrento, Italy, Jan 2009.

[23] H. Droogendijk, C. M. Bruinink, R. G. P. Sanders, A. M. K. Dagamseh, R. J. Wiegerink and G. J. M. Krijnen, "Improving the performance of biomimetic hair-flow sensors by electrostatic spring softening," *Journal of Micromechanics and Microengineeirng,* vol.

22, no. 6, 2012.

[24] A. R. Aiyar, C. Song, S.-H. Kim and M. G. Allen, "An All-Polymer Airflow Sensor Using a Piezoresistive Composite Elastomer," *Smart Materials and Structures,* vol. 18, p. 115002, 2009.

[25] A. Qualtieri, F. Rizzi, G. Epifani, A. Ernits, M. Kruusmaa and M. De Vittorio, "Parylene-Coated Bioinspired Artificial Hair Cell for Liquid Flow Sensing," *Microelectronic Engineering,* vol. 98, pp. 516-519, 2012.

[26] H. Bleckmann, "Role of the Lateral Line in Fish Behaviour," in *The Behaviour of Teleost Fishes,* Springer US, 1986, pp. 177-202.

[27] A. M. K. Dagamseh, C. M. Bruinink, R. J. Wiegerink, T. S. J. Lammerink, H. Droogendijk and G. J. M. Krijnen, "Interfacing of Differential-Capacitive Biomimetic Hair Flow-Sensors for Optimal Sensitivity," *Journal of Micromechanics and Microengineering,* vol. 23, p. 035010, 2013.

[28] S. Matsumoto and N. Ichikawa, "New methods for liquid encapsulation in polymer MEMS structures," Tucson, AZ, Jan 2008.

[29] C. A. Gutierrez and E. Meng, "Improved self-sealing liquid encapsulation in Parylene structures by integrated stackable annular-plate stiction valve," in *Micro Electro Mechanical Systems (MEMS), 2010 IEEE 23rd International Conference on*, Wanchai, Hong Kong, 24-28 Jan. 2010.

[30] M. A. Lapisa, F. Niklaus and G. Stemme, "Room-temperature wafer-level hermetic sealing for liquid reservoirs by gold ring embossing," in *Solid-State Sensors, Actuators and Microsystems Conference, 2009. TRANSDUCERS 2009. International*, Denver, CO, USA, 21-25 June 2009.

[31] T. Ninomiya, Y. Okayama, Y. Matsumoto, X. Arouette, K. Osawa and N. Miki, "MEMS-based hydraulic displacement amplification mechanism with completely encapsulated liquid," *Sensors and Actuators A: Physical,* vol. 166, no. 2, pp. 277-282, April 2011.

[32] H. Kim and K. Najafi, "Characterization of Low-Temperature Wafer Bonding Using Thin-Film Parylene," *Journal of Microelectromechanical Systems (JMEMS),* vol. 14, no. 6, pp. 1347-1355, Dec 2005.

[33] B.-K. Nguyen, E. Iwase, K. Matsumoto and I. Shimoyama, "Electrically driven varifocal micro lens fabricated by deposition Parylene Directly on Liquid," in *Micro Electro Mechanical Systems, 2007. MEMS. IEEE 20th International Conference on (MEMS'07),* Kobe, Japan, Jan 2007.

[34] M. M. Sadeghi, H. S. Kim and K. Najafi, "Electrostatically driven micro-hydraulic actuator arrays," in *Micro Electro Mechanical Systems, 2010 IEEE 23rd International Conference on, (MEMS'10),* Wanchai, Hong Kong, Jan 2010.

[35] H. Kim and K. Najafi, "Electrostatic Hydraulic Threeway Gas Microvalve for High-pressure Applications," in *Proc. 12th Int. Conf. on Miniaturized Systems for Chemistry and Life Sciences (μTAS'08),* San Diego, California, USA, October 12-16, 2008.

[36] W. K. Schomburg, Introduction to Microsystem Design, Aachen: Springer, 2011.

[37] T. A. Harder, T.-J. Yao, Q. He, C.-Y. Shih and Y.-C. Tai, "Residual Stress in Thinfilm Parylene-c," in *Micro Electro Mechanical Systems, 2002. The Fifteenth IEEE International Conference on*, Las Vegas, NV, 20-24 January 2002.

[38] T. Jordan, Z. Ounaies, J. Tripp and P. Tcheng, "Electrical Properties and Power Considerations of a Piezoelectric Actuator," ICASE, NASA, Hampton, Virginia, 2000.

[39] J. O. Wilkes, Fluid Mechanics for Chemical Engineers, Second Edition, New York: Prentice Hall, 2006.

[40] N. Binh-Khiem, K. Matsumoto and I. Shimoyama, "Tensile Film Stress of Parylene Deposited on Liquid," *Langmuir*, vol. 26, no. 24, pp. 18771-18775, 2010.

[41] L. M. Walpita, W. M. Pleban and H. Eckhardt, "Liquid Crystaline Polyemr Composites Having High Dielectric Constant". USA Patent 5,962,122, 5 October 1995.

[42] Dupont (Wilmington, DE, USA), "DuPont Krytox," [Online]. Available: http://www2.dupont.com/Lubricants/en_US/uses_apps/Product_Guide.html. [Accessed 8 March 2013].

[43] Solvay International Chemical Group (Brussels, Belgium), "Fomblin® PFPE Lubricants," [Online]. Available: http://www.solvayplastics.com/sites/solvayplastics/EN/specialty_polymers/Fluorinated_Fluids/Pages/Fomblin_Lubricants_PFPE.aspx. [Accessed 8 March 2013].

[44] C. Sullivan, "Lumped Fluid Systems," 2004. [Online]. Available: http://www.dartmouth.edu/~sullivan/22files/Fluid_sys_anal_w_chart.pdf. [Accessed 4 January 2014].

[45] M. M. Sadeghi, R. L. Peterson and K. Najafi, "Hair-Based Sensors for Micro-Autonomous Systems," in *Proc. SPIE 8373, 83731L*, Baltmore, MD, Apr 2012.

[46] M. M. Sadeghi, R. L. Peterson and K. Najafi, "High-Speed Electrostatic Micro-Hydraulics for Sensing and Actuation," *Micro Electro Mechanical Systems (MEMS), 2013 IEEE 26th International Conference on*, pp. 1191-1194, 20-24 January 2013.

[47] G. L. Smith, S. S. Bedair, B. E. Schuster, W. D. Nothwang, J. S. Pulskamp, C. D. Meyer and R. G. Polcawich, "Biologically Inspired, Haltere, Angular-Rate Sensors for Micro-Autonomous Systems," *Proc. SPIE 8373, Micro- and Nanotechnology Sensors, Systems, and Applications IV, 83731K*, 1 May 2012.

[48] C. Santulli, T. J. Finn and R. S. a. G. Jeronimidis, "Scanning LDV for Vibration Measurement of Filiform Hairs in Crickets in Response to Induced Airflow," in *Proc. SPIE 6345, Seventh International Conference on Vibration Measurements by Laser Techniques: Advances and Applications, 63450E*, Ancona, Italy, June 19-22, 2006.

[49] T. Shimozawa, T. Kunmagai and Y. Baba, "Structural scaling and functional design of the cercal wind-receptor hairs of cricket," *Journal of Comparative Physiology A*, vol. 183, no. 2, pp. 171-186, Jul 1998.

[50] M. M. Sadeghi, R. L. Peterson and K. Najafi, "Micro-hydraulic structure for high

performance bio-mimetic air flow sensor arrays," in *IEEE International Electron Devices Meeting (IEDM)*, Washington, DC, Dec 2011.

[51] M. M. Sadeghi, R. L. Peterson and K. Najafi, "A 2-D Directional Air Flow Sensor Array Made Using Stereolithography and MEMS Micro-Hydraulic Structures," in *17th Int. Conf. on Solid-State Sensors, Actuators and Microsystems, Trancducers'13*, Barcelona, Spain, June 16-20, 2013.

[52] "Viper si2 - 3D Systems," 3D Systems Inc. , [Online]. Available: http://www.3dsystems.com/products/datafiles/viper/datasheets/International/viper_si2_uk.qxd.pdf. [Accessed 14 November 2013].

[53] "Accura® ClearVue," 3D Systems Inc., [Online]. Available: http://www.3dsystems.com/materials/accurar-clearvue#.UoVcnHBjuM4. [Accessed 14 November 2013].

[54] M. M. Sadeghi, R. L. Peterson, K. Peterson, R. Fearing and K. Najafi, "Air-flow Sensing on Autonomous Mobile Platforms Using Micro-Scale Hot-Wire Anemometry," in *27th Army Science Conference*, Orlando, 2010.

[55] G. Krijnen, A. Floris, M. Dijkstra, T. Lammerink and R. Wiegerink, "Biomimetic Micromechanical Adaptive Flow-Sensor Arrays," in *Proc. SPIE 6592, Bioengineered and Bioinspired Systems III, 65920F*, Gran Canaria, Spain, May 22, 2007.

[56] Analog Devices, "AD7746: 24-Bit, 2 Channel Capacitance to Digital Converter," 5 2005. [Online]. Available: http://www.analog.com/en/analog-to-digital-converters/capacitance-to-digital-converters/ad7746/products/product.html. [Accessed 5 July 2012].

[57] "AD7147: Captouch™ Programmable Controller for Single-Electrode Capacitance Sensors," September 2011. [Online]. Available: http://www.analog.com/en/analog-to-digital-converters/capacitance-to-digital-converters/ad7147/products/product.html. [Accessed 17 November 2013].

[58] K. Suzuki and K. Najafi, "A 1024-Element High-Performance Silicon Tactile Imager," *IEEE Transaction on Electron Devices*, vol. 37, no. 8, pp. 1852-1860, August 1990.

[59] C. Ko, J. Wu, W. Wang, C. Huang, S. Tseng, Y. Chen and M. Lu, "A Highly Sensitive CMOS-MEMS Capacitive Tactile Sensor," *IEEE Int. Conf. on Microelectromech. Systems (MEMS), Istanbul, Turkey*, pp. 642-645, 22-26 January 2006.

[60] H. Lee, S. Chang and E. Yoon, "A Flexible Polymer Tactile Sensor: Fabrication and Modular Expandability for Large Area Deployment," *Jounral Microelectromechanical Systems (JMEMS)*, vol. 15, no. 6, pp. 1681-1686, 2006.

[61] H. Lee, J. Chung, S. Chang and E. Yoon, "Normal and Shear Force Measurement Using a Flexible Polymer Tactile Sensor With Embedded Multiple Capacitors," *Jounral of Microelectromechanical Systems (JMEMS)*, vol. 17, no. 4, pp. 934-942, 2008.

[62] K. Kim, K. Lee, W. Kim, K. Park, T. Kim, J. Kim and J. Pak, "Polymer-Based Flexible Tactile Sensor up to 32×32 Arrays Integrated with Interconnection Terminals," *Sensors and Actuators A: Physical*, vol. 156, pp. 284-291, 2009.

[63] H. B. Muhammad, C. Recchiuto, C. M. Oddo, L. Beccai, C. J. Anthony, M. J. Adams, M. C. Carrozza and M. C. L. Ward, "A Capacitive Tactile Sensor Array for Surface Texture Discrimination," *Journal of Microelectronic Engineering,* vol. 88, pp. 1811-1813, 2011.

[64] T. Takahashi, M. Suzuki, S. Iwamoto and S. Aoyagi, "Capacitive Tactile Sensor Based on Dielectric Oil Displacement out of a Parylene Dome into Surrounding Channels," *Journal of Micromachines,* pp. 270-278, 2012.

[65] R. W. Van Boven and K. O. Johnson, "The Limit of Tactile Spatial Resolution in Humans," *Neurology,* vol. 44, no. 12, pp. 2361-2366, 1994.

[66] J. G. Zhou, D. Herscovici and C. C. Chen, "Parametric Process Optimization to Improve the Accuracy of Rapid Prototyped Stereolithography Parts," *International Journal of Machine Tools and Manufacture,* vol. 40, no. 3, pp. 363-379, 2000.

[67] M. M. Sadeghi, R. L. Peterson and K. Najafi, "Electrostatically driven micro-hydraulic actuator arrays," in *Micro Electro Mechanical Systems, 2010 IEEE 23rd International Conference on, (MEMS'10)*, Wanchai, Hong Kong, Jan 2010.

[68] M. M. Sadeghi, R. L. Peterson and K. Najafi, "Air Flow Sensing Using Microwire Bonded Hair-Like Hot-Wire Anemometry," *Journal of Micromechanics and Microengineering,* vol. 23, no. 8, p. 085017, August 2013.

[69] M. M. Sadeghi, R. L. Peterson and K. Najafi, "Hair-based sensors for micro-autonomous systems," in *Proc. SPIE 8373, 83731L*, Baltmore, MD, Apr 2012.

[70] M. M. Sadeghi, K. Dowling, R. L. Peterson and K. Najafi, "High Sensitivity, High Density Micro-Hydraulic Force Sensor Array Utilizing Stereo-Lithography Fabrication Technique," in *Micro Electro Mechanical Systems (MEMS), 2013 IEEE 26th International Conference on*, Taipei, Taiwan, January 20-24, 2013.

[71] Y.-H. Wang, C.-P. Chen, C.-M. Chang, C.-P. Lin, C. Lin, L.-M. Fu and C.-Y. Lee, "MEMS-Based Gas Flow Sensors," *Microfluid Nanofluid,* vol. 6, pp. 333-346, 2009.

[72] M. Elwenspoek, "Thermal flow micro sensors," in *International Semiconductor Conference, 1999. CAS '99 Proceedings*, Sinaia, Romania, Oct 1999.

[73] T. Neda, K. Nakamura and T. Takumi, "A polysilicon flow sensor for gas flow meters," *Sensors and Actuators A: Physical,* vol. 54, no. 1-3, pp. 626-631, 1996.

[74] F. Kohl, R. Fasching, F. Keplinger, R. Chabicovsky, A. Jachimowicz and G. Urban, "Development of miniaturized semiconductor flow sensors," *Measurement,* vol. 33, no. 2, pp. 109-119, March 2003.

[75] S. Bouwstra, R. Legtenberg, H. A. Tilmans and M. Elwenspoek, "Resonating microbridge mass flow sensor," *Sensors and Actuators A: Physical,* vol. 21, no. 1-3, pp. 332-335, 1990.

[76] O. Berbrig, K. Nottmeyer, J. Mizuno, Y. Kanai and T. Kobayashi, "The Prandtl micro flow sensor (PMFS): a novel silicon diaphragm capacitive sensor for flow velocity measurement," *Sensors and Actuators A: Physical,* vol. 66, no. 1-3, pp. 93-98, 1999.

[77] N. Svedin, E. Kalvesten and G. Stemme, "A new edge-detected lift force flow sensor," *Journal of Microelectromechanical Systems (JMEMS),* vol. 12, no. 3, pp. 344-354, 2003.

[78] J. Chen, Z. Fan, J. Zou, J. Engel and C. Liu, "Two-Dimensional Micromachined Flow Sensor Array for Fluid Mechanics Studies," *Journal of Aerospace Engineering,* vol. 16, no. 2, pp. 85-97, 2003.

[79] Dantec Dynamics A/S (Skovlunde, Denmark), "Hot-wire and Hot-film Probes," 22 November 2012. [Online]. Available: http://www.dantecdynamics.com/Default.aspx?ID=750. [Accessed 6 February 2013].

[80] O. Tabata, "Fast-response silicon flow sensor with an on-chip fluid temperature sensing element," *IEEE Transactions on Electron Devices,* vol. 33, no. 3, pp. 361-365, Mar 1986.

[81] F. Jiang, Y.-C. Tai, C.-M. Ho, R. Karan and M. Garstenauer, "Theoretical and experimental studies of micromachined hot-wire anemometers," in *International Electron Devices Meeting, 1994. IEDM '94. Technical Digest.*, San Francisco, CA, Dec 1994.

[82] E. Yoon and K. D. Wise, "An integrated mass flow sensor with on-chip CMOS interface circuitry," *IEEE Transactions on Electron Devices,* vol. 39, no. 6, pp. 1376-1386, Jun 1992.

[83] P. Bruschi, M. Dei and M. Piotto, "A Single Chip, Double Channel Thermal Flow Meter," *Microsystem Technologies,* vol. 15, no. 8, pp. 1179-1186, August 2009.

[84] Y.-T. Liao, W. Biederman and B. Otis, "A Fully Integrated CMOS Accelerometer Using Bondwire Inertial Sensing," *IEEE Sensors Journal,* vol. 11, no. 1, pp. 114-122, Jan 2011.

[85] F. E. Jorgensen, "How to measure turbulence with hot-wire anemometers- a practical guide," Dantec Dyanmics, 1 2 2002. [Online]. Available: http://www.dantecdynamics.com/Default.aspx?ID=456. [Accessed 27 June 2012].

[86] C. G. Lomas, Fundamentals of Hot Wire Anemometery, Cambridge: Cambridge University Press, 1986.

[87] H. H. Bruun, Hot-wire Anemometry, Oxford: Oxford University Press, 1995.

[88] F. P. Incropera and D. P. DeWitt, Introduction to Heat Transfer, 4th ed., John Wiley & Sons, 2001.

[89] W. A. Khan, J. R. Culham and M. M. Yovanovich, "Fluid Flow Around and Heat Transfer From an Infinite Circular Cylinder," *Journal of Heat Transfer,* vol. 127, pp. 785-790, July 2005.

[90] B. C. Khoo, Y. T. Chew, C. Lim and T. C. J, "Dynamic response of a hot-wire anemometer. Part I: A marginally elevated hot-wire probe for near-wall velocity measurements," *Measurement Science and Technology,* vol. 9, no. 5, pp. 751-761, January 1998.

[91] J. F. Shackelford, CRC materials science and engineering handbook, 3rd ed., Boca

Raton, FL: CRC Press, 2001.

[92] Heraeus Holding GmbH (Hanau, Germany), "Heraeus Materials Technology - Heraeus Ball Bonding Wires," [Online]. Available: http://heraeus-contactmaterials.com/en/products/audr/ballbonding/ha_1.aspx. [Accessed 6 February 2013].

[93] A. S. Azad and S. Z. Kassab, "New Method of Obtaining Dissipation," *Experiments in Fluids,* vol. 7, no. 2, pp. 81-87, November 1989.

[94] S. Z. Kassab, "Effect of the hot-wire length on the determination of the length scale of large eddies," *Measurement Science and Technology,* vol. 2, no. 7, pp. 647-652, 1991.

[95] OMEGA Engineering INC. (Stamford, Connecticut, USA), "Hot Wire Anemometer with Real Time Data Logger," [Online]. Available: http://www.omega.com/pptst/HHF-SD1.html. [Accessed 6 February 2013].

[96] J. Funari, "Micro-Surface Welding". United States of America Patent 4,171,477, 16 October 1979.

[97] C.-M. Lin and R. D. Sam, "Laser-Driven Microwelding Apparatus and Process". United States of America Patent 5,938,952, 17 August 1999.

[98] G. Kaltsas and A. G. Nassiopoulou, "Novel C-MOS compatible monolithic silicon gas flow sensor with porous silicon thermal isolation," *Sensors and Actuators A: Physical,* vol. 76, no. 1-3, pp. 133-138, Aug 1999.

[99] C. M. Bruinink, R. K. Jaganatharaja, M. J. de Boer, E. Berenschot, M. L. Kolster, T. S. J. Lammerink, R. J. Wiegerink and G. J. M. Krijnen, "Advancements in Technology and Design of Biomimetic Flow-Sensor Arrays," in *Micro Electro Mechanical Systems, 2009. MEMS 2009. IEEE 22nd International Conference on*, Sorrento, Italy, Jan 2009.

[100] Sensirion AG (Staefa ZH, Switzerland), "Datasheet ASF1400," [Online]. Available: http://www.sensirion.com/en/products/mass-flow-meters-for-gases/mass-flow-sensor-asf14001430/. [Accessed 6 February 2013].

[101] K. A. A. Makinwa and J. H. Huijsing, "A smart wind sensor using thermal sigma-delta modulation techniques," *Sensors and Actuators A: Physical,* Vols. 97-98, pp. 15-20, Apr 2002.

[102] Y. Su, A. G. R. Evans, A. Brunnschweiler and G. Ensell, "Characterization of a highly sensitive ultra-thin piezoresistive silicon cantilever probe and its application in gas flow velocity sensing," *Journal of Micromechanics and Microengineering,* vol. 12, no. 6, pp. 780-785, Nov 2002.